Chem Soc Rev

REVIEW ARTICLE

View Article Online
View Journal | View Issue

Cite this: *Chem. Soc. Rev.*, 2026, **55**, 4303

Multi-scale roles of water in electrocatalytic CO_2 and CO reduction

Xiaoyang He,† Weiwen Zhou,† Junxiong Chen, Qinghong Zhang, Ye Wang and Shunji Xie *

The electrocatalytic CO_2 reduction reaction (CO_2RR) in aqueous electrolytes is a cornerstone technology for achieving a carbon-neutral society. Beyond the direct CO_2RR, the sequential reduction of CO_2 to CO followed by the CO reduction reaction (CORR) offers an alternative pathway. Water plays a pivotal and complex multi-scale role in CO_2RR/CORR systems. Its influence spans multiple scales, including micro-scale water-mediated reaction kinetics, meso-scale regulation of the local aqueous microenvironment, and macro-scale optimization of operational conditions. Factors at these different scales are interconnected and mutually interactive, ultimately determining the overall reaction performance. Therefore, this review establishes a comprehensive multi-scale framework for water regulation in both the CO_2RR and the CORR. We systematically elucidate the roles of water, survey advanced regulation strategies, and discuss state-of-the-art *in situ* characterization and simulation techniques. Finally, we identify key challenges and provide a forward-looking perspective, emphasizing that as this technology matures towards large-scale applications, such synergistic, multi-scale regulation becomes increasingly critical. This work aims to offer a clear roadmap for designing high-performance, stable, and large-scale CO_2RR/CORR systems and accelerating their practical implementation.

Received 15th October 2025

DOI: 10.1039/d5cs01088h

rsc.li/chem-soc-rev

1. Introduction

Global industrialization and population growth have escalated energy demand, primarily fulfilled by fossil fuels, leading to a persistent rise in atmospheric CO_2 concentrations that not only poses significant risks to global climate stability but also conflicts with sustainable development goals.[1,2] The electrocatalytic CO_2 reduction reaction (CO_2RR) offers a promising solution that leverages renewable electricity to convert waste CO_2 into value-added chemicals and fuels, simultaneously addressing the storage of intermittent renewable energy and advancing carbon neutrality.[3] The CO_2 electrolysis technologies can be categorized into high-temperature (>600 °C) and low-temperature (<100 °C) systems. While high-temperature

State Key Laboratory of Physical Chemistry of Solid Surfaces, Collaborative Innovation Center of Chemistry for Energy Materials, Innovation Laboratory for Sciences and Technologies of Energy Materials of Fujian Province (IKKEM), College of Chemistry and Chemical Engineering, Xiamen University, Xiamen 361005, China. E-mail: shunji_xie@xmu.edu.cn

† These authors contributed equally.

Xiaoyang He

Xiaoyang He received his BE degree from the Dalian University of Technology in 2019. He is a PhD student in the Department of Chemistry at Xiamen University under the supervision of Prof. Shunji Xie. His research interests focus on catalyst design, electrolyzer engineering, and in situ characterization for electrocatalytic CO_2 reduction.

Weiwen Zhou

Weiwen Zhou received his BSc degree from Xiamen University in 2024. He is a MSc student in the Department of Chemistry at Xiamen University under the supervision of Prof. Shunji Xie. His research interest focuses on the electrocatalytic reduction of CO.

CO_2 electrolysis has shown progress in CO production,[4] its monoproduct nature restricts its broader application. In contrast, the low-temperature CO_2RR in an aqueous electrolyte has garnered significant attention for its ability to selectively generate C_1–C_6 olefins and oxygenates under mild conditions.[5] Furthermore, the tandem pathway, involving the initial reduction of CO_2 to CO followed by a subsequent CO reduction reaction (CORR) in an aqueous electrolyte, represents another promising research avenue.[6–9] The significant potential of these approaches has positioned the CO_2RR/CORR systems as a major research hotspot.

However, in these aqueous-based systems, water emerges as a pivotal variable, conferring substantial tunability while introducing multifaceted challenges. At the micro-scale, water acts as a key reactant, supplying protons and potential partial oxygen sources to modulate the product spectrum; yet, this versatility often results in broad product distributions and facilitates the competing hydrogen evolution reaction (HER), diminishing target selectivity. Additionally, water molecules, together with cations, constitute an important component of the electrode–electrolyte interface double layer (EDL), regulating the electric field strength of the double layer and thus influencing the adsorption configuration, binding strength, and local concentration of intermediates, as well as reactant competition at the active sites.[10,11] Shifting to the larger-scale, water acts as a solvent and mass transfer medium. At the meso-scale, local water content dictates the state of the three-phase boundary (TPB) within the catalyst layer, creating a critical trade-off between maximizing ion and mass transport and preventing electrode flooding.[12] Meanwhile, at the macro-scale, overall operational conditions, such as the electrolyzer configuration and associated reaction conditions, govern the overall water balance and its distribution across the electrolyser. These factors, in turn, influence the CO_2/CO

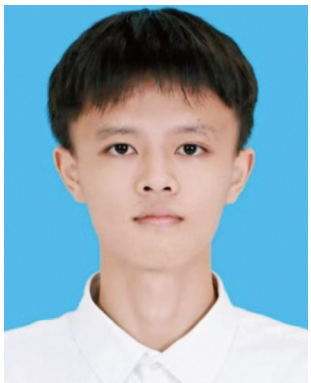

Junxiong Chen

Junxiong Chen received his BSc degree from FuZhou University in June 2024. He is a MSc student in the Department of Chemistry at Xiamen University under the supervision of Prof. Shunji Xie. His research interest focuses on the electrocatalytic reduction of CO_2.

Qinghong Zhang

Qinghong Zhang received her BSc and MSc degrees from Nanjing University in 1989 and 1992 and obtained her PhD degree from the Hiroshima University of Japan in 2002. She joined Xiamen University in October 2002 and was promoted to full professor in 2010. Her research interests include the synthesis and characterization of novel materials with advanced catalytic properties.

Ye Wang

Ye Wang received his BSc degree from Nanjing University and PhD degree from the Tokyo Institute of Technology. He then worked at the Tokyo Institute of Technology, Tohoku University and Hiroshima University and was promoted to associate professor at Hiroshima University in 2001. He became a full professor of Xiamen University in August 2001. He served as a council member of the International Association of Catalysis Societies and is an associate editor of ACS Catalysis. The research interest of Prof. Ye Wang's group is catalysis for C_1 and sustainable chemistry, including C–H activation and C–C coupling of C_1 molecules and C–O/C–C cleavage chemistry for cellulose/lignin valorization.

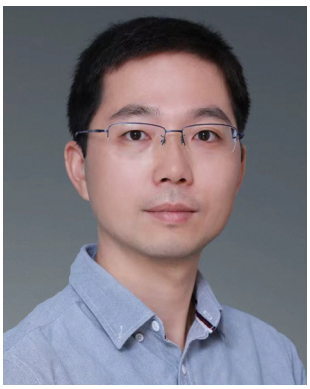

Shunji Xie

Shunji Xie received his BSc and MSc degrees from the Hunan University of China in 2008 and 2011 and obtained his PhD degree from Xiamen University in 2014. He then carried out postdoctoral research at the Collaborative Innovation Center of Chemistry for Energy Materials (iChEM). He became a full professor in the College of Chemistry and Chemical Engineering of Xiamen University in 2020. His research interest focuses on photocatalysis and electrocatalysis for C_1 and sustainable chemistry, including CO_2 reduction, CH_4 oxidation, biomass conversion, and ethylene glycol synthesis.

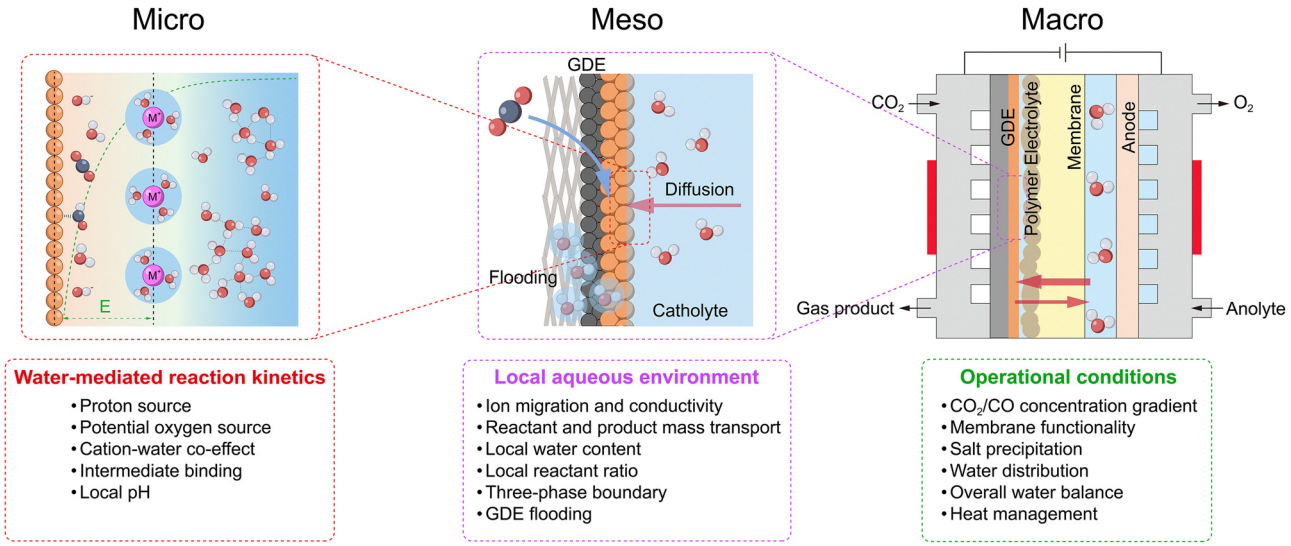

Fig. 1 Illustration of the interplay of water regulation across micro-, meso-, and macroscales in the electrocatalytic CO_2RR. The orange, grey, red, and white spheres represent metal particles, carbon, oxygen, and hydrogen atoms, respectively. GDE stands for the gas diffusion electrode.

concentration gradient, ion exchange membrane functionality (*e.g.*, conductivity, swelling, and stability), heat management (as the primary thermal storage and exchange medium),[13] and long-term stability against challenges such as salt precipitation.[14,15] Crucially, these scales are deeply interconnected. Macro-scale operating conditions across various electrolysers with diverse configurations dictate the meso-scale local environment, regulating micro-scale water-mediated reaction kinetics; in turn, micro-scale reactions provide feedback to the local environment, collectively determining overall CO_2RR/CORR performance including selectivity (Faradaic efficiency, FE), activity, stability, and energy conversion efficiency (Fig. 1).

Despite the profound impact of water, a comprehensive understanding that connects these disparate scales remains lacking. Although recent reviews have discussed the role of water in electrocatalysis,[16–18] they typically concentrate on understanding reaction mechanisms at the micro-scale and focus predominantly on the CO_2RR. Such a microscopic perspective, however, is increasingly inadequate to interpret the overall performance variations observed in practical devices. Furthermore, the related CORR process is often overlooked.[7] In the absence of a systematic comparison, it is challenging to distinguish whether strategies are transferable across reactions or limited to specific operational requirements. As CO_2RR research progresses from fundamental catalyst exploration toward industrial scale-up, distinct water-related behaviours emerge that are unobservable at the micro-scale. The cross-scale propagation of impacts shifts the priority of governing factors, thereby necessitating an integrated perspective to accurately evaluate their relative importance to guide rational scale-up. Consequently, the lack of a systematic review integrating meso- and macro-scale strategies creates a disconnection that hinders the development of large-scale applications.

To bridge this critical gap, this review establishes a comprehensive, multi-scale framework for water regulation in the CO_2RR/CORR. Distinct from previous molecular perspectives, this framework advances beyond microscopic confinement to explicitly elucidate the water-mediated molecular mechanisms (micro), the local water environment (meso), and overall operational conditions (macro). We first elucidate the roles of water across different scales in the CO_2RR and CORR, highlighting its distinct impacts and corresponding regulation strategies. We then systematically investigate advanced water regulation strategies from the micro- to the macro-level and discuss state-of-the-art *in situ* characterization and simulation techniques for probing the dynamic behaviour of water. Finally, we identify the prevailing challenges and provide a forward-looking perspective on water management, with the aim of offering a clear roadmap for the development of large-scale CO_2RR systems with enhanced performance and stability. Synthesizing these multi-level insights, this review offers a holistic perspective to advance the practical applications of CO_2 electrolysis.

2. Multiscale roles and influence mechanisms of water in the CO_2RR/CORR

This section is dedicated to elucidating the pivotal role of water across different scales in the CO_2RR/CORR, thereby enabling a profound comprehension and discussion of the various multi-scale investigative strategies reported in the literature.

2.1. Water as a direct chemical reactant: source of protons and oxygen

Water acts as a crucial proton donor *via* two primary mechanisms: direct dissociation and proton-coupled electron transfer (PCET). During the CO_2RR/CORR, the electrode–electrolyte interface typically exhibits a near-neutral to alkaline pH.[19] Driven by this environment, water acts as the predominant

kinetically viable proton provider. In this regime, hydronium ions (H_3O^+) are depleted ($<10^{-7}$ M), hydroxide ions (OH^-) act inherently as acceptors, and bicarbonate functions primarily as a CO_2 donor (confirmed by the kinetic isotope effect, KIE).[20] This leaves the abundant solvent water (*ca.* 55 M) as the dominant proton source. Consequently, the direct dissociation pathway, which predominates under near-neutral or alkaline conditions, is exemplified by the Volmer step ($H_2O + e^- + * \rightarrow *H + OH^-$). In this process, water molecules dissociate on the catalyst surface to form adsorbed hydrogen intermediates (*H), which subsequently contribute to the hydrogenation of reaction intermediates and the competing HER (Fig. 2). In contrast, the PCET mechanism involves a concerted or sequential process wherein an electron is transferred to an adsorbed intermediate, accompanied by proton donation from species such as H_2O ($*CO_2 + H_2O + e^- \rightarrow *COOH + OH^-$) (Fig. 2, left side). DFT calculations utilizing explicit solvent models provide critical evidence that such water participation significantly alters reaction energetics. For instance, Wang *et al.* explicitly demonstrated on Sn(112) that water clusters form hydrogen-bonding networks that significantly stabilize O-containing intermediates (*e.g.*, HCOO* and CHO* + OH*), thereby shifting the potential-limiting step compared to vacuum models.[21] Similarly, on Cu(100), Chen *et al.* revealed that water-mediated direct proton transfer (Eley–Rideal mechanism) significantly lowers kinetic barriers for C–H bond formation steps compared to surface-hydrogenation pathways (Langmuir–Hinshelwood); specifically, the barrier for $*CH_2$–C reduction drops from 1.10 eV (LH) to 0.49 eV (ER), facilitating the selective production of ethylene.[22] The first is the competition from the parasitic HER, where the kinetics of water dissociation limit the overall FE of carbon-containing products. The second aspect is the proton availability that tunes the specific carbon-containing product distribution, where rapid *CO protonation promotes deep hydrogenation to C_1 species (*e.g.*, CH_4) while a restricted proton supply facilitates *CO dimerization toward C_{2+} products.

Beyond its role as a proton donor, water can function as a potential partial oxygen source. Although the oxygen atoms in oxygenated products are predominantly derived from CO_2 (in the CO_2RR) or CO (in the CORR), emerging evidence suggests that in certain CORR pathways producing C_{2+} oxygenates such as ethanol,[23,24] acetic acid,[25] and *n*-propanol,[24] oxygen atoms from the aqueous solvent (H_2O) or hydroxide ions (OH^-) can be incorporated into the final products (Fig. 2, right side). For instance, Lum *et al.* utilized $H_2{}^{18}O$ labeling to reveal that 60–70% of the oxygen in ethanol and *n*-propanol originates from the solvent water. They proposed a non-electrochemical Grotthuss-chain-mediated co-hydrolysis mechanism, wherein a water chain directly attacks the *C–CH intermediate to insert solvent oxygen.[23] Complementing this view, Hasa *et al.* employed *operando* flow electrolyzer mass spectrometry (FEMS) to track volatile intermediates. While they found that the oxygen in the acetaldehyde intermediate initially stems from CO, it undergoes rapid oxygen exchange with solvent water in the alkaline electrolyte before being further reduced to ethanol, thereby explaining the presence of solvent-derived oxygen in alcohols.[16] Regarding acetate formation, Jouny *et al.* combined $C^{18}O$ labeling with gas chromatography-mass spectrometry (GC-MS) analysis to demonstrate a distinct mechanism: acetate is formed *via* the nucleophilic attack of a solvent-derived OH^- on a reaction intermediate, resulting in a product containing one oxygen from CO and one from the electrolyte.[25]

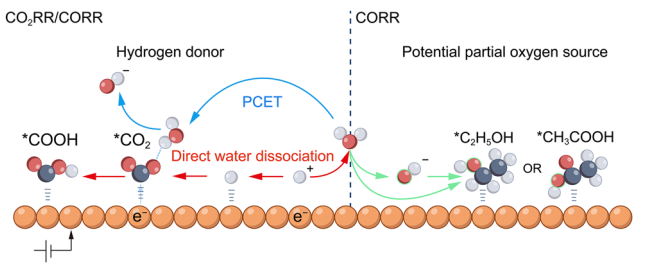

Fig. 2 Schematic of the dual roles of water as both a hydrogen and an oxygen donor in the electrocatalytic CO_2RR/CORR. The orange, grey, red, and white spheres represent metal particles, carbon, oxygen, and hydrogen atoms, respectively. PCET stands for proton-coupled electron transfer.

2.2. Shaping of the interfacial microenvironment by water and its impact on reaction kinetics and selectivity

Beyond its direct participation as a reactant, water exerts a profound influence on the microenvironment at the catalyst–electrolyte interface through intricate interactions with the electrode surface, electrolyte ions, and reaction intermediates.

Under an applied cathodic potential, the electrode surface accumulates a charge, attracting counter-ions from the electrolyte to establish the electrical double layer (EDL) with a well-defined structure and electric field distribution.[26] This EDL, fundamental to electrochemical processes, typically consists of an inner Helmholtz plane (IHP) featuring tightly adsorbed ions and an outer Helmholtz plane (OHP) comprising solvated ions (Fig. 3a).[27] Within the EDL, water molecules, characterized by their substantial dipole moment and high relative permittivity ($\varepsilon_r \approx 78.3$),[28] not only organize into ordered structures in response to the electrode potential but also effectively solvate electrolyte ions.[29] Critically, water serves as the primary dielectric medium of the EDL and thus governs the distribution of the interfacial electric field (Fig. 3a).

Furthermore, this water-mediated EDL structure is profoundly influenced by electrolyte cations, giving rise to the cation effect that modulates reaction dynamics.[30] Particularly, alkali metal cations (*e.g.*, Li^+, Na^+, K^+, and Cs^+) significantly modulate the reaction pathways and selectivity of the CO_2RR and CORR by reshaping the EDL structure and interfacial electric field strength. The mechanism is rooted in how the intrinsic properties of each cation, such as charge density, size, bare ionic radius, hydration shell size, and hydrated radius, dictate its interactions with surrounding water molecules and overall behaviour within the EDL.[10,31] Despite increasing bare radii down the group ($Li^+ < Cs^+$), smaller cations exhibit higher

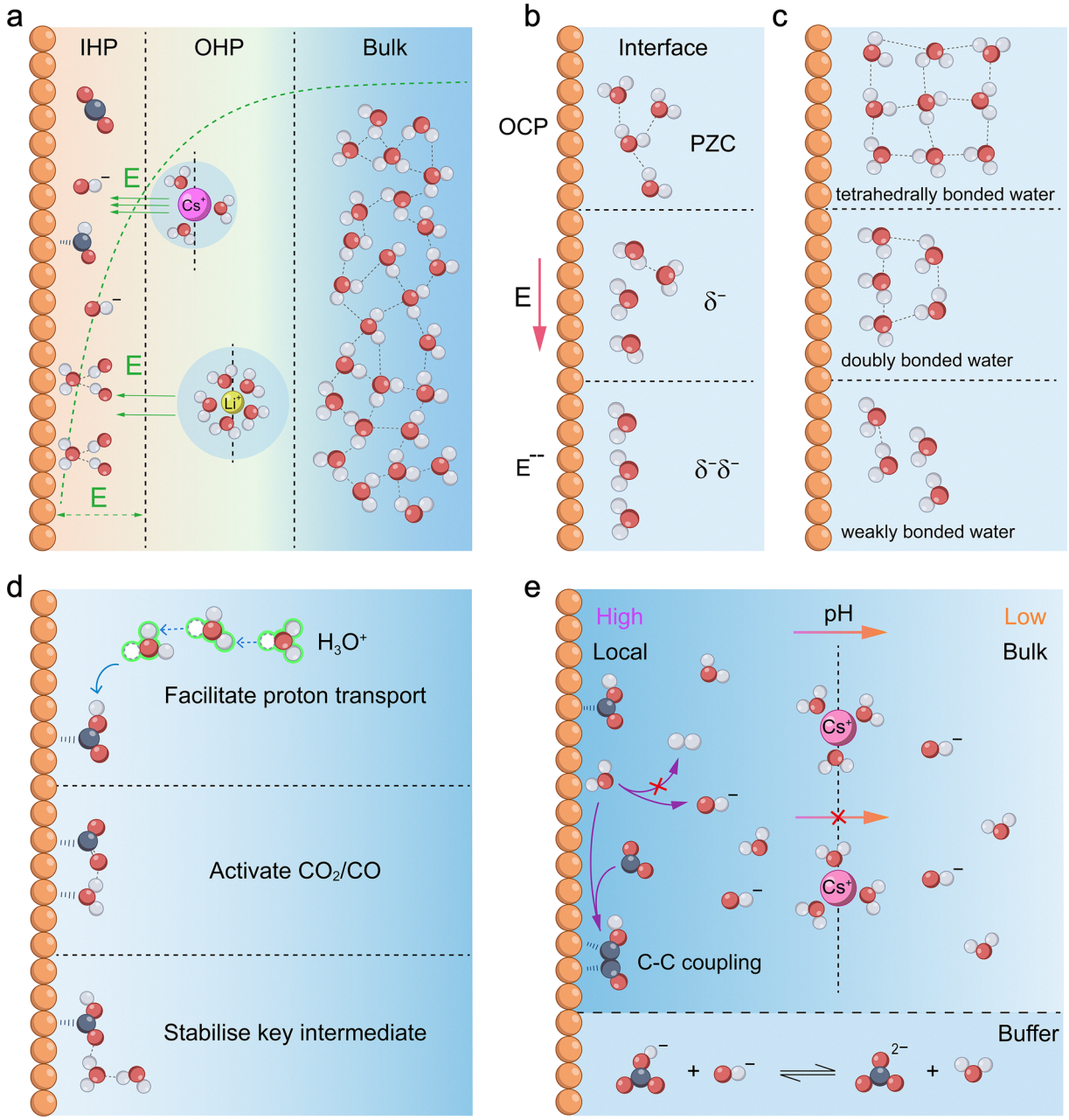

Fig. 3 Water-mediated shaping of the microscopic interfacial environment. (a) Schematic of the electrical double layer (EDL) according to the Gouy–Chapman–Stern model, illustrating the Stern and diffuse layers. The green curve indicates the potential as a function of the distance from the surface. (b) Reorientation of interfacial water molecules in response to the applied cathode potential. (c) Schematic representation of different bonding states of water molecules. (d) The dual role of interfacial water in stabilizing reaction intermediates and facilitating proton transport through hydrogen-bonding networks. (e) Regulation of local pH at the cathode interface by hydrated cations and buffer anions. The orange, grey, red, and white spheres represent metal particles, carbon, oxygen, and hydrogen atoms, respectively. IHP, OHP, OCP, and PZC stand for the inner Helmholtz plane, outer Helmholtz plane, open circuit potential and potential of zero charge, respectively.

charge density and stronger hydration ($Li^+ > Cs^+$), leading to larger hydrated radii. Under applied electric fields, hydrated cations accumulate at the OHP, where their size, charge, and shell structure determine the OHP position, EDL capacitance, and potential gradient. Strongly hydrated cations (*e.g.*, Li^+) shift the OHP farther from the surface, yielding a gradual potential drop and weaker field, while weakly hydrated ones (*e.g.*, Cs^+) reside closer, generating a steep drop and strong field (Fig. 3a). This intensified field promotes C_{2+} formation in the CO_2RR by polarising CO_2, stabilising intermediates (*e.g.*, $*CO_2^-$), and reducing activation barriers for CO_2 activation and C–C coupling.[32] Additionally, strong cation-interfacial water interactions indirectly regulate the local concentration, solubility, or adsorption behaviour of CO_2 near the interface by disrupting

the hydrogen-bond network,[33] reorienting molecules, and modulating local water activity.[34]

Moreover, driven by a dynamic equilibrium among ion hydration, the interfacial electric field, and the electronic structure of the electrode, a distinctive interfacial water region is established (Fig. 3a and b). This region consists of the initial water layers adjacent to the electrode, featuring altered hydrogen-bond networks and molecular orientations.[35] Its structure is inherently dynamic, continuously adapting to changes in applied potential, intermediate adsorption, and ion concentration. Based on the resulting integrity of the hydrogen-bond network, spectroscopic analysis (*e.g.*, O–H stretching and H–O–H bending vibrations) classifies this interfacial water into three types (Fig. 3c): tetrahedrally bonded water, which is least perturbed and maintains a stable, ice-like network; doubly bonded water, an intermediate state with a partially disrupted network; and weakly bonded water, where strong interactions with the electrode surface break the hydrogen bonds, leading to a highly disordered and reactive structure. The relative abundance of these water species is distinctly modulated by the identity of the electrolyte cation, as evidenced by surface-enhanced infrared absorption spectroscopy (SEIRAS) spectra.[36] In Li^+-containing electrolytes, the spectra are dominated by peaks characteristic of the rigid, strongly hydrogen-bonded (ice-like) water network, driven by the high charge density of Li^+ that locks surrounding water into a stiff primary hydration shell. In contrast, the Cs^+-containing electrolytes exhibit a significant intensity increase in peaks corresponding to weakly bonded or free water molecules. The large, low-charge-density Cs^+ exerts weaker constraints, effectively disrupting the ordered network. AIMD simulations further confirm that such a flexible, disordered water network (rich in free water) facilitates the rotation of water molecules to adapt to the dipole changes of reaction intermediates (*e.g.*, $*CO_2^{\delta-}$), thereby lowering the reorganization energy for the PCET step. The relative proportions of these three water types are critical as they directly govern water dissociation and proton transport. Studies indicate that water dissociation ability follows the order: weakly bonded water > doubly bonded water > tetrahedrally bonded water.[37] A higher proportion of tetrahedrally bonded water enhances the connectivity of the hydrogen-bond network, while a greater presence of weakly bonded water increases the dynamic disorder, an appropriate degree of which facilitates proton transport. First, this structured network ensures the efficient supply of protons from the bulk solution or hydrated species to active sites (Fig. 3d),[38] for instance *via* the Grotthuss mechanism.[39] Second, it directly interacts with adsorbed species (*e.g.*, CO_2 and CO) through hydrogen bonding and dipole interactions, thereby altering their energetics and configurations beyond mere dielectric screening (Fig. 3d).[40–42] Third, individual water molecules can act as hydrogen-bond bridges to stabilise key transition states (Fig. 3d), consequently lowering the activation energies for crucial water-assisted elementary steps.[43]

The influence of ions on water behaviour also extends to regulating the local pH at the electrode surface (Fig. 3e). During the CO_2RR/CORR, proton consumption or OH^- production induces a marked pH increase near the electrode relative to the bulk electrolyte, an effect magnified at higher current densities (Fig. 3e).[44] Electrolyte cations play a central role in this regulation, with two primary mechanisms proposed. The electrostatic shielding model suggests that large, weakly hydrated cations (*e.g.*, Cs^+) accumulate at the interface, impeding OH^- diffusion away from the surface and thus elevating local pH.[10] In contrast, the cation hydrolysis model posits that strongly interacting cations polarize water molecules in their hydration shells, thereby reducing the apparent pK_a of coordinated water.[45] These polarized water molecules thus act as proton donors to neutralize OH^-, buffering and suppressing the local pH rise. To quantitatively assess these cation-dependent pH variations, Cuesta *et al.* employed *in situ* probes and SEIRAS to monitor the interfacial environment.[46] Their findings revealed that the magnitude of the interfacial pH rise follows the order $Li^+ > Na^+ > K^+ > Cs^+$, highlighting the distinct buffering capabilities of hydrated cations. While buffering anions (*e.g.*, HCO_3^-/CO_3^{2-}) also modulate pH, they cannot fully eliminate these gradients.[47] Although an elevated local pH generally favours C_{2+} production over the HER, excessive alkalinity can destabilise key *CO intermediates and deplete local CO_2.[48] Therefore, precise pH control is essential for optimising selectivity.

Beyond the specific identity of the cation, its concentration serves as a pivotal parameter that governs the reaction kinetics by fundamentally restructuring the interfacial water environment. As bulk cation concentration increases, hydrated cations accumulate more densely in the electrical double layer, inducing multi-faceted impacts. First, the rigid hydration shells associated with these enriched cations sever the connectivity of the hydrogen-bond network of water and sequester free water molecules, thereby lowering the effective interfacial water activity (a_w).[34] This concentration-dependent scarcity of free water directly suppresses the competing HER by limiting the supply of accessible proton donors. Second, the intensified electric field stabilized by the dense cationic layer interacts electrostatically with polar intermediates such as $*CO_2^-$ and *CO to lower activation barriers. Third, this densely populated cation layer acts as a physical barrier that imposes a dual mass-transport limitation, simultaneously hindering proton migration toward the electrode and restricting the outward diffusion of generated OH^-, thereby elevating local pH and further favoring CO_2/CO reduction pathways.

Furthermore, thermodynamic conditions, specifically temperature and pressure, exert profound impacts on the interfacial water structure. At the micro-scale, temperature reshapes the interface primarily by intensifying the thermal motion of water molecules. As the temperature rises, thermal perturbations gradually counteract the ordering constraints imposed by the electrode electric field, inducing thermal destabilization or relaxation of the rigid hydrogen-bond network at the interface.[49] AIMD simulations by Sun *et al.* reveal that at 330 K, the radial distribution function (RDF) peaks of interfacial water broaden and diminish in intensity.[50] This

degradation of long-range order effectively lowers the solvent reorganization energy, thereby facilitating proton transport through the electrical double layer to the active sites. Concurrently, elevated temperatures accelerate the exchange dynamics of hydration shells surrounding cations, promoting a closer proximity of distinct, partially dehydrated cations to the electrode surface.[51] This proximity alters the local electric field strength and proton supply rate, effectively modulating the water-mediated proton kinetics. In contrast, reaction pressure reshapes the interfacial water environment by elevating the interfacial concentration of reactants (*e.g.*, CO_2) and consequently inducing local acidification.[51] While this acidification fundamentally alters the ionic atmosphere (as detailed in the reaction-specific section below), the most dominant physical consequence of elevated pressure is the steric exclusion of interfacial water. The increased solubility of non-polar CO_2 leads to significant interfacial accumulation, causing steric interference. Consequently, the lateral hydrogen-bond connectivity among water molecules is disrupted, fragmenting the continuity of the proton transport, which manifests as a significant suppression of the competing HER.[52]

Regarding reaction specificity, the interfacial water structure in the CO_2RR and the CORR exhibits significant divergence that is governed by the intrinsic properties of the gaseous reactants and the electrolyte. In the CO_2RR, the high solubility of CO_2 ($\sim$33 mmol L^{-1} under ambient conditions) and the consequent acidification effect ($CO_2 + H_2O \rightleftharpoons H^+ + HCO_3^-$) lower the local pH.[14] This acidic environment introduces high concentrations of hydronium ions, which locally perturb the tetrahedral water network. However, against this locally disordered background, the dissolution of non-polar CO_2 triggers a strong hydrophobic hydration effect, compelling surrounding water molecules to reorient to preserve water–water hydrogen bonds.[49] Consequently, despite the acidic disruption, water molecules form a rigid, locally ordered solvation shell encasing the CO_2. While the bulk network continuity is disrupted, this local structural ordering stabilizes reaction intermediates and modulates protonation pathways. Conversely, in the CORR, the distinct physicochemical constraints dictate a different water behavior. These differences stem from the markedly lower solubility of CO (*ca.* 1 mmol L^{-1}) and the absence of the acidification effect observed in the CO_2RR.[14] Moreover, the CORR is typically carried out under strongly alkaline conditions, where the high concentration of hydroxide ions (OH^-) and hydrated cations at the electrode interface strongly perturbs the local hydration structure.[53,54] The interactions between these ions and water molecules disrupt the continuous hydrogen-bond network, rendering the interfacial water structure more disordered and dynamic. This isolated water microenvironment not only alters interfacial proton/water dynamics and effectively cuts off proton transfer pathways to suppress the competing HER, but also favors key steps such as C–C coupling.

2.3. Water as a mass transport medium

At meso- and macro-scales, the dynamic transport of water as the essential solvent and electrolyte medium remains critical, particularly within the porous gas diffusion electrode (GDE). Effective management of this behaviour, which governs reactant supply, product removal, and ionic conductance, is crucial for optimizing reaction performance.

At the meso-scale (component level), the role of water focuses on migration, distribution, gradient variation, and corresponding local concentration of water within individual components of the electrolyser, such as the catalyst layer, diffusion layer, and membrane. Understanding and precisely controlling water behaviour, influenced by material properties like porosity and wettability and by interfacial structures, is crucial for optimizing reaction performance. The challenge of this optimization trade-off is immediately apparent within the GDE. The inherently low solubility of CO_2/CO in aqueous electrolytes leads to significant mass transport limitations at high current densities.[12] The GDE is designed to mitigate this issue by dramatically shortening the diffusion path to the catalyst surface (Fig. 4). Within the GDE, however, the local water content becomes the critical variable, playing a dual and often conflicting role. On one hand, the hydration level dictates the physical nature of the reaction interface; with increasing hydration, the interface can shift from a dry gas–solid boundary to an optimal triple-phase (gas–liquid–solid) boundary, and ultimately to a flooded liquid–solid boundary (Fig. 4).[55] On the other hand, and in parallel, a continuous aqueous network is essential for efficient ion transport, as local ionic conductivity is directly modulated by the water content and ion hydration. Consequently, a critical trade-off in water management must be addressed. Insufficient water content hinders essential ion transport through the catalyst layer, whereas excessive water creates a thick film that imposes a severe mass transport barrier for gaseous reactants, leading to reactant starvation. Beyond its direct role in transport and reaction, water exerts a crucial indirect effect on GDE flooding resistance and structure disruptions. On one hand, gaseous products, such as H_2 or C_2H_4, can form bubbles that displace the aqueous electrolyte from the catalyst surface, thereby causing physical disruption by blocking active sites and increasing Ohmic losses.[56,57] On the other hand, the accumulation of water-soluble oxygenated products introduces a separate challenge, as it can dynamically alter the wettability of the GDE. Leonard *et al.* systematically studied the role of electrode wettability in CO_2 electrolysers.[58] Their study found that as the mass fraction of products such as formic acid (FA), methanol (MeOH), ethanol (EtOH), and *n*-propanol (PrOH) increases in the aqueous solution, the contact angles on the surfaces of two common electrode materials, polytetrafluoroethylene (PTFE) and graphite, both decrease (Fig. 5a and b). Moreover, on both surfaces, the wetting effect of the products on the electrode increases in the order of FA < MeOH < EtOH < PrOH. Notably, PTFE exhibited superior resistance to wetting compared to graphite. Furthermore, simulation results indicated that operating at a higher current density or with a lower liquid water sweep flow rate causes a higher local product concentration. This lowers the effective hydrophobicity of the electrode and significantly increases the risk of flooding (Fig. 5c). In addition, interactions between

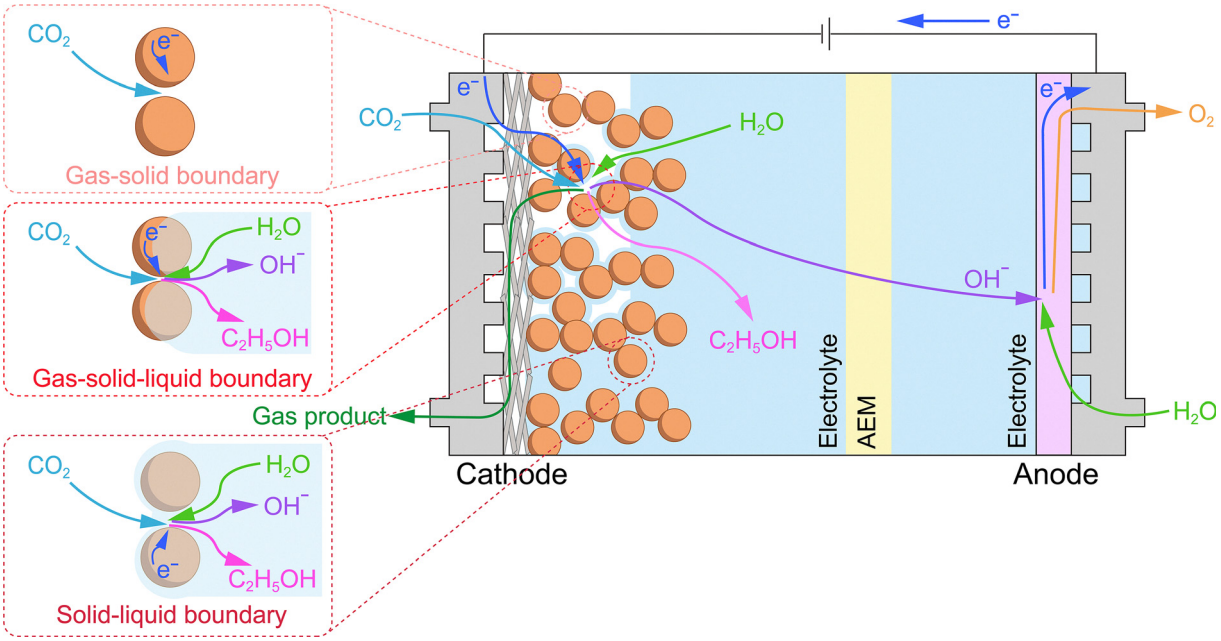

Fig. 4 Schematic illustrating the transport pathways of reactants, products, ions, and electrons for the CO_2RR in a flow cell, and how water content in the GDE impacts the three-phase boundary at the cathode. The inset provides a magnified comparison of gas–solid, solid–liquid, and gas–solid–liquid boundaries. The orange spheres represent metal particles. AEM stands for the anion exchange membrane.

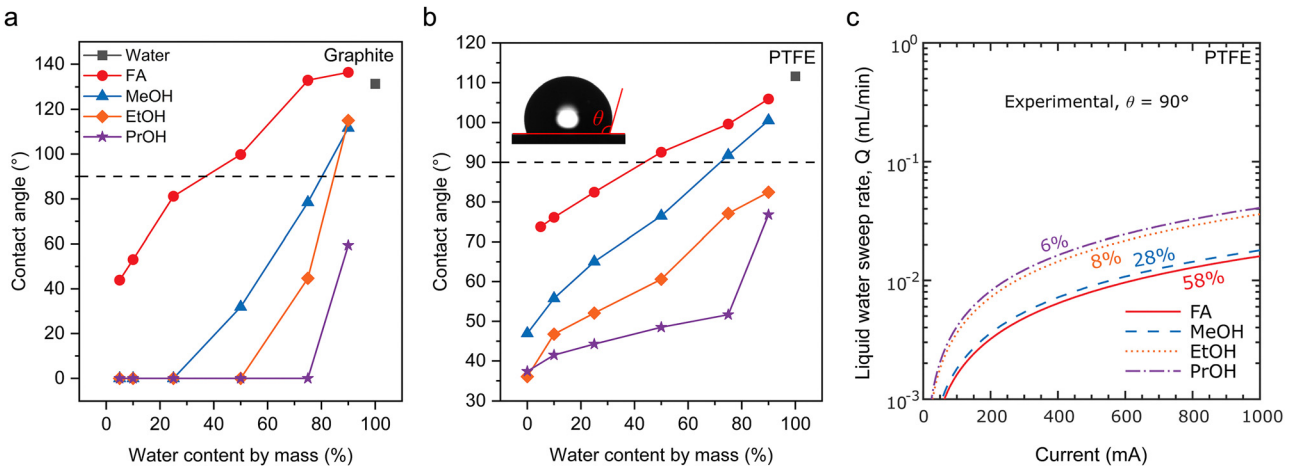

Fig. 5 Wettability of CO_2RR products on the GDE: a study of contact angles and operating parameter dependencies. (a) Sessile drop contact angles of CO_2RR liquid products on graphite surfaces as a function of water content. (b) Sessile drop contact angles of CO_2RR liquid products on PTFE surfaces as a function of water content. (c) Dependence of reaction current density on liquid flow velocity at the wettability transition point (θ = 90°) on PTFE. Reproduced with permission from ref. 58. Copyright 2020, Electrochemical Society, Inc. FA, MeOH, EtOH, and PrOH stand for formic acid, methanol, ethanol, and *n*-propanol, respectively.

water and the electrolyte can also alter the hydrophobicity of the GDE.[59] Therefore, maintaining a stable triple-phase boundary (TPB) through dynamic water management emerges as paramount for achieving long-term stability at industrial current densities.

At the macro-scale, system-level engineering provides a powerful top-down approach for water regulation to modulate the local reaction environment. This strategy encompasses managing the boundary conditions of the electrolyser by controlling the introduction, circulation, and removal of water. Key factors include the overall electrolyser architecture, flow field design, the type of the ion exchange membrane and operating parameters such as temperature, CO_2/CO humidity, and electrolyte flow rate and concentration. These factors significantly influence macro-scale water management, which manifests in several critical, interdependent aspects. The overall water balance is a prerequisite for steady-state operation, defined by a dynamic balance between total water introduction (*e.g.*, *via* anolyte flow or cathode humidification) and total water removal (*e.g.*, *via* product gas streams or cathodic drainage). However,

even if the overall water balance is maintained, the spatial water distribution determined by macro-scale key factors (*e.g.*, flow field design), defined as the overall concentration field of water across different components and locations within the electrolyzer, is the critical determinant of performance uniformity. This non-uniformity directly induces spatial maldistribution of CO_2/CO, creating localized wet zones (where flooding causes CO_2 starvation) and dry zones on the electrode. Consequently, the performance of the system is dictated not by a single concentration value but by the concentration field variations dictated by the macro-design. This non-uniform macro-water distribution also profoundly impacts key components: for the ion exchange membrane, it directly governs its hydration state (*i.e.*, its degree of swelling and water uptake), which in turn profoundly impacts macro-critical performance metrics such as ionic conductivity, selectivity, and mechanical stability.[60] Furthermore, the electrolysis process (especially at high current densities) generates substantial Joule heat due to Ohmic and reaction overpotentials. Owing to its high specific heat capacity, water acts as the primary carrier for thermal management at the macro-scale, where circulating electrolyte or reactant gas streams remove waste heat and influence system temperature. The electrolyte/gas flow rate will affect the spatial distribution of heat.

Thus, this macro-level control establishes the foundational operating environment, dictating transport phenomena at smaller scales and thereby regulating meso-scale water transport and micro-scale catalytic reactions.

2.4. Integrating water effects across scales and systems

The choice of electrolyser configuration is paramount, as it fundamentally dictates how these multi-scale water challenges manifest and can be managed, primarily through distinct water supply mechanisms. The classic H-type cell, for instance, features fully submerged, plate-like electrodes where water is supplied from all sides by the bulk electrolyte. This configuration proves useful for initial catalyst screening. However, it largely decouples the micro-scale reaction from controlled meso-scale transport, often leading to performance dominated by severe mass transport limitations (Fig. 6a).[14] In contrast, the flow cell represents a significant advancement. By employing a semi-submerged electrode design where water is primarily supplied *via* the flowing liquid catholyte, it introduces forced convection that provides a degree of meso-scale control over the local chemical environment (Fig. 6b). This allows for more reliable investigation of micro-scale kinetics under realistic operating conditions. Finally, the membrane electrode assembly (MEA) electrolyser is the most integrated platform. As a zero-gap system with non-submerged electrodes, it eliminates bulk electrolyte entirely. Consequently, water must be supplied either by diffusion across the ion exchange membrane from the anode or through humidification of the cathode feed gas. In an MEA, this tight coupling of water supply with the electrode structure means that every aspect, from molecular-level reactions to system-level water feed, is interdependent, making holistic, multi-scale water management the central challenge for achieving industrial-scale performance and stability (Fig. 6c).

2.5. Membrane-driven water transport and microenvironment control in MEAs

In the MEA configuration, the influence of water on membrane properties is significantly amplified, and these properties are tightly coupled with overall electrolyzer performance. This tight coupling makes the type of ion exchange membrane employed the critical factor, as it dictates the specific transport mechanisms of water and ions, thereby shaping the local pH and reaction microenvironment at the cathode. For CO_2RR systems,

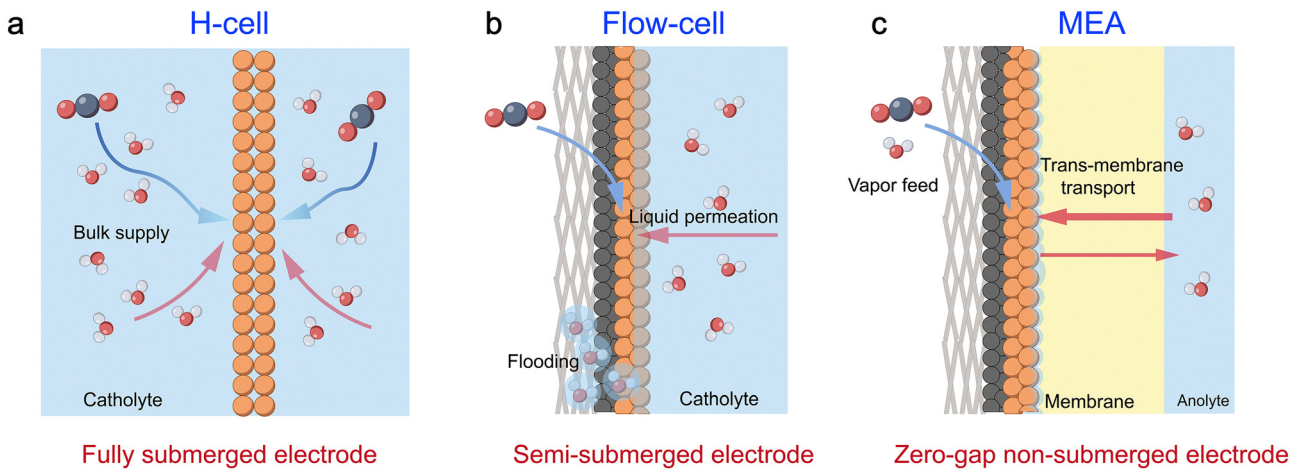

Fig. 6 Water transport and supply mechanisms in three typical electrolyser configurations. (a) The classic H-cell features a fully submerged electrode, where water is supplied from all sides by the bulk electrolyte. (b) The flow cell features a semi-submerged electrode, where water is supplied *via* a flowing catholyte. (c) The membrane electrode assembly (MEA) features a zero-gap non-submerged electrode. Water is supplied through humidification of the gas feed and/or transport (crossover and back-diffusion) across the membrane. The orange, gray, red, and white spheres represent metal particles, carbon, oxygen, and hydrogen atoms, respectively. Blue arrows indicate gas diffusion, red arrows represent water diffusion, with the thickness of red arrows reflecting the relative amount of water diffusion.

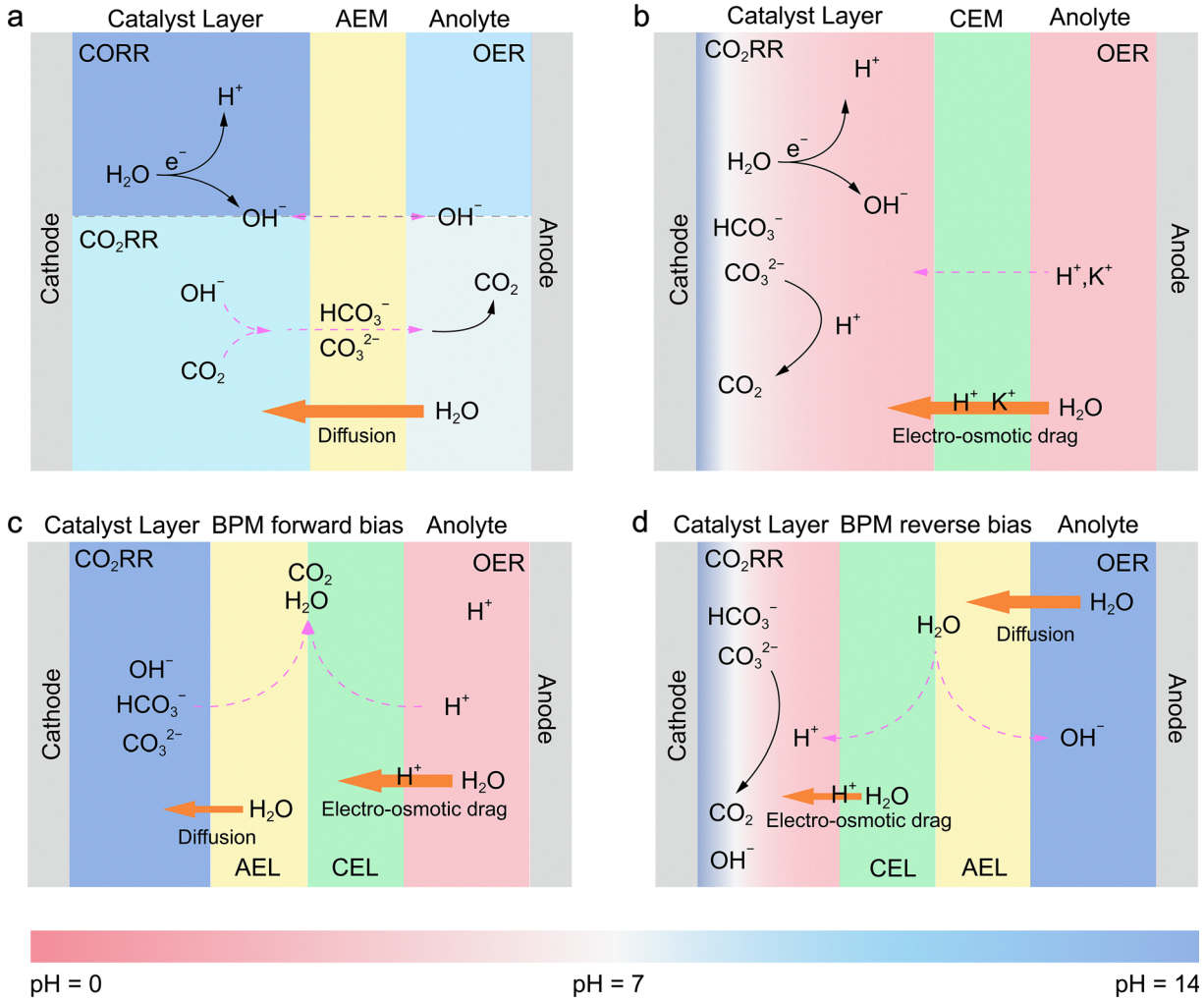

Fig. 7 Schematic illustration of cathode water supply, ion transport, and local pH profiles in four typical simplified MEA configurations for the CO_2RR/CORR. (a) AEM-based electrode assembly for the CO_2RR/CORR. (b) CEM-based electrode assembly for the CO_2RR. (c) Forward-biased BPM-based electrode assembly for the CO_2RR. (d) Reverse-biased BPM-based electrode assembly for the CO_2RR. Orange arrows indicate water transport across the membrane, with the thickness of pink arrows reflecting the relative amount of water diffusion. AEM, CEM, BPM, CEL, and AEL stand for the anion exchange membrane, cation exchange membrane, bipolar membrane, cation exchange layer, and anion exchange layer, respectively.

the anion exchange membrane (AEM), cation exchange membrane (CEM, also known as the proton exchange membrane, PEM), and bipolar membrane (BPM) have been employed, whereas for CORR systems, AEMs are predominantly used (Fig. 7).[61,62] The anolyte serves as a critical source for water transport and ion transport within the membrane. Due to differences in ion transport mechanisms, the net water flux toward the cathode varies significantly across different ion exchange membrane systems. Both cathodic CO_2RR and CORR involve the consumption of water to generate OH^-; however, in the CO_2RR, the produced OH^- further reacts with CO_2 to form HCO_3^-/CO_3^{2-}, thereby affecting the reaction performance.

In AEM systems, water is primarily supplied to the cathode through diffusion driven by a concentration gradient (Fig. 7a). In the CO_2RR, HCO_3^-/CO_3^{2-} generated at the cathode is transported across the AEM to the anode, where it releases CO_2 during the oxygen evolution reaction (OER). A higher operating current leads to a higher local OH^- concentration at the cathode, intensifying its reaction with CO_2. This results in increased CO_2 release at the anode, which in turn exacerbates the alkalinity at the cathode and acidity at the anode, thereby increasing the transmembrane pH gradient.[63] Concurrently, the electric-field-driven migration of hydrated alkali metal ions from the anolyte across the AEM to the cathode results in salt accumulation within the GDE, ultimately causing the deactivation of the CO_2RR. In contrast, the CORR avoids carbonation side reactions, with OH^- serving as the charge carrier, migrating from the cathode to the anode, maintaining anodic alkalinity while the cathode local pH remains higher (Fig. 7a).[44]

To address these challenges, CEM and BPM systems have been developed. In CEM systems, H^+ ions generated by the OER are transported to the cathode along with a large amount of water, driven by the strong electro-osmotic drag (EOD)

effect (Fig. 7b). There, they react with cathodically generated HCO_3^-/CO_3^{2-} to form CO_2 and water, acidifying the carbonate species to prevent salt precipitation and enable *in situ* CO_2 recycling. Concurrently, a small amount of alkali metal cations (*e.g.*, K^+) from the anolyte can permeate through the CEM to the cathode.[64] On the surface of the cathode catalyst, a local, near-neutral pH microenvironment is created *via* the cation effect, which suppresses the HER and improves the selectivity of CO_2RR products. At the same time, the anode maintains an acidic environment.

The BPM systems achieve complete decoupling of pH between the anode and cathode *via* the reaction interface between the anion exchange layer (AEL) and cation exchange layer (CEL), with water transport and conversion mechanisms varying by the bias direction.[65,66] In the forward-biased mode (the anode to the CEL and the cathode to the AEL), H^+ generated by the OER carries water across the CEL to the BPM interface under strong EOD (Fig. 7c). Simultaneously, HCO_3^-/CO_3^{2-} generated from the cathode reaction crosses the AEL and recombines with H^+ at the interface to form water and release CO_2.[67] As the cathode continuously consumes water while the interface generates it, a concentration gradient drives water migration from the interface to the cathode. Ultimately, this configuration maintains an alkaline cathode environment and an acidic anode environment.[61] In the reverse-biased mode (the anode to the AEL and the cathode to the CEL), water dissociates into H^+ and OH^- at the AEL/CEL catalytic interface (Fig. 7d). Driven by a concentration gradient, water from the anolyte migrates through the AEL to the interface. Subsequently, the generated H^+ under EOD carries water through the CEL to the cathode, rendering the cathode side (near the CEL) acidic. In practice, engineering strategies such as buffer layers are often employed to create a locally weakly alkaline or neutral microenvironment at the catalyst surface, suppressing the HER and promoting the CO_2RR.[67,68] HCO_3^-/CO_3^{2-} generated at the cathode reacts with H^+ to form CO_2,[68] while OH^- migrates through the AEL, maintaining a stable alkaline environment at the anode.[61,62]

Overall, the type of membrane regulates the nature of charge carriers (H^+, OH^-, and HCO_3^-/CO_3^{2-}) and water flux, indirectly determining the local pH at the cathode and the overall CO_2RR/CORR performance.

2.6. Water-regulated CO transport in tandem CO_2 reduction

In the tandem CO_2 reduction process, the aqueous environment plays a unique and decisive role. These systems typically involve two spatially distinct active sites, where site A is responsible for reducing CO_2 to the CO intermediate and site B further reduces CO into high-value-added products. Depending on the inter-site distance, tandem systems are generally classified into nanoscale and macroscale regimes (Fig. 8). In both configurations, the aqueous environment plays distinct yet crucial roles in modulating intermediate transport and the ubiquitous competitive HER.

In nanoscale tandem configurations (Fig. 8a), where the two active sites are in atomic contact or separated by less than a few

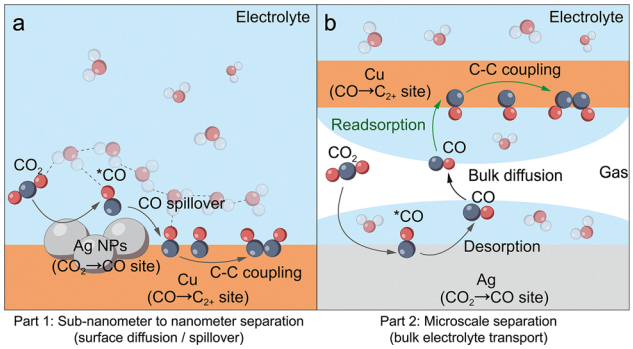

Fig. 8 Schematic illustration of scale-dependent effects of water on intermediate transport during tandem CO_2RR. (a) Molecular-level tandem systems with a nanoscale inter-site distance. (b) Hierarchical tandem systems with a microscale inter-site distance. The orange, light-gray, dark-gray, white and red spheres represent metal particles, copper, silver, carbon, hydrogen, and oxygen atoms, respectively.

nanometers, the transport of the CO intermediate is dominated by surface diffusion or near-surface liquid-phase hopping. In this regime, water primarily acts as both a diffusion medium and a competitive adsorbent. On one hand, water molecules interact with adsorbed *CO species *via* hydrogen bond networks to modulate their thermodynamic stability. On the other hand, the low solubility and high diffusion coefficient of CO in water, combined with the vast volume mismatch between the bulk electrolyte and the interfacial diffusion layer, establish a steep concentration gradient. This gradient drives the rapid diffusion and dissipation of generated CO into the bulk solution, which prevents its effective capture by adjacent sites. Simultaneously, the competitive adsorption of water molecules on site B remains a persistent bottleneck. This parasitic HER directly occupies active sites and impedes the re-capture of CO.

When the inter-site distance extends to the micro- or millimeter scale (Fig. 8b), a range typically observed in layered electrode architectures, surface spillover effects are no longer dominant. Instead, the reaction relies on a trajectory where CO must first exit the liquid film, migrate *via* the convective gas flow, and subsequently re-enter the electrolyte at the utilization layer (*e.g.*, Cu). This desorption–gas transport–readsorption pathway is particularly vulnerable to porous electrode flooding, which thickens the liquid barrier and exacerbates CO dilution. This phenomenon severs gas diffusion channels and thereby restricts the effective supply of CO to the reaction sites. Crucially, this CO starvation effect exacerbates the HER on site B, which becomes even more dominant in the macroscale regime.

2.7. Differing emphasis on water regulation in the CO_2RR and the CORR

While the challenge of water management is universal in both the CO_2RR and the CORR, the specific strategies and research objectives diverge significantly due to the distinct nature of the reactants. This fundamental difference begins with the variations in the roles of water across scales, ranging from in intermediate formation to interfacial environments, local pH,

mass transport, and product selectivity. In the CO_2RR, the reaction between CO_2 and locally generated OH^- readily forms poorly soluble carbonate or bicarbonate salts,[14] simultaneously attenuating pH gradients. This precipitation creates a dual problem: it causes physical pore blockage that impedes mass transport, while the hydrophilic nature of these salts can also draw excess water into the electrode and compound the risk of flooding. In contrast, the CORR lacks this intrinsic buffering capacity. Furthermore, the same catalysts under identical conditions in the CORR tend to yield more C_{2+} oxygenated products compared to the CO_2RR.[7] It can alter the surface wettability of the GDE and disrupt the delicate three-phase interface (Fig. 4 and 5).[58] Furthermore, the CORR has a stronger dependence on alkalinity, as its typically higher local pH fosters a strongly alkaline microenvironment.[44] This accelerates the degradation of the carbon-based GDE material itself, which in turn exacerbates water management issues and hastens performance decay.[69] Thus, there are both shared and unique approaches to enhancing reaction stability through water regulation. Beyond common goals such as improving activity and stability, current water regulation strategies for the CO_2RR predominantly focus on improving the total FE of C_{2+} products and the single FE of C_1 product, suppressing the HER. In contrast, since many catalysts in the CORR already exhibit high intrinsic C_{2+} FE (often $>80\%$), water regulation efforts are primarily centered on enhancing selectivity toward single C_{2+} products.

Moreover, under ambient conditions, CO_2 exhibits $\sim$33-fold higher solubility compared to CO.[14] This disparity results in distinct impacts of water flooding on the stability of the CO_2RR and the CORR (Fig. 9). For both the CO_2RR and the CORR conducted with a highly hydrophobic GDE, the GDE initially maintains its excellent hydrophobicity. This limits water penetration into the gas diffusion layer (GDL), allowing both CO_2 and CO to be effectively transported to the active sites (Fig. 9a and d). However, as the reaction progresses, the hydrophobicity of the GDE gradually diminishes, and different dynamics emerge. In the CO_2RR, the formed bicarbonate droplets can penetrate the catalyst layer and enter the GDL. Nevertheless, owing to the higher solubility of CO_2, it can still traverse these droplets to reach the active sites (Fig. 9b). Subsequent gas flow removes part of the water vapor, promoting the formation of carbonate particles within the GDL. The hygroscopic nature of these carbonates further promotes water diffusion,[70] causing the liquid to gradually extend toward the GDL backside and into the flow channels of the bipolar plate.[71] After the gas flow carries away the water, salts remain deposited in the channels, completely blocking CO_2 diffusion while also limiting further water ingress (Fig. 9c). In contrast, during the CORR, once the catalyst layer loses its hydrophobicity, the electrolyte penetrates the GDL interior, significantly limiting CO access to the diffusion layer (Fig. 9e). In particular, when a continuous aqueous pathway forms within the GDL, external water influx increases persistently, ultimately preventing CO from reaching the active sites (Fig. 9f). Therefore, in the CO_2RR, as long as solid salts do not form a physical barrier, CO_2 can still diffuse slowly to the catalyst surface; whereas in the CORR, significant water accumulation within the GDL completely impedes CO diffusion to the reaction sites.

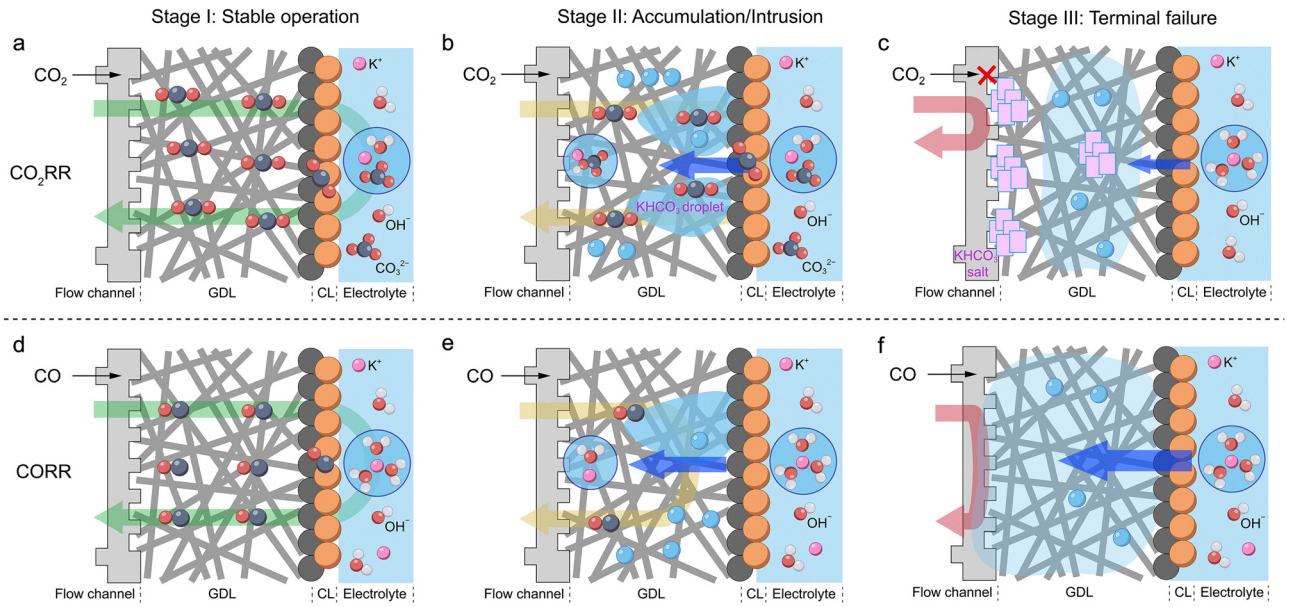

Fig. 9 Comparison of water flooding effects on CO_2/CO and water diffusion processes within the GDE across different temporal states in the CO_2RR and the CORR. (a) Initial state of the CO_2RR. (b) Penetration of bicarbonate droplets into the GDL interior in the CO_2RR. (c) Complete accumulation of salts in the flow channel in the CO_2RR. (d) Initial state of the CORR. (e) Penetration of droplets into the GDL interior in the CORR. (f) Complete water flooding state inside the GDL in the CORR. The orange, gray, red, white and pink spheres represent metal particles, carbon, oxygen, hydrogen and potassium atoms, respectively. The blue sphere represents water droplets. Blue arrows indicate water diffusion through the catalyst layer into and out of the GDL, with the thickness of the arrows reflecting the relative amount of water diffusion. CL and GDL stand for the catalyst layer and the gas diffusion layer, respectively.

In summary, the multi-scale effects of water manifest as a bidirectionally coupled cycle (Fig. 1). Proceeding top-down, a deterministic pathway is observed wherein macro-scale operational conditions govern the meso-scale local aqueous environment, which then modulates the micro-scale water-mediated reaction kinetics. The bottom-up feedback and emergent pathway is characterized by micro-scale kinetic processes accumulating at the meso-scale, and these cumulative effects ultimately emerge at the macro-scale as observable system performance and challenges.

3. Multiscale water regulation strategies

Building upon the established mechanistic roles of water in the electrochemical CO_2RR/CORR, this section provides a systematic review of multi-scale regulatory strategies for water management. Given the significant overlap in underlying strategies, this discussion deliberately addresses the CO_2RR and the CORR in a unified manner, allowing for a more direct comparison of how common approaches are adapted to meet distinct reaction-specific goals. These strategies span the micro-scale, including catalyst- and electrolyte-centered design; the meso-scale, focusing on the engineering of GDE design (including its layered components and material types) as a shared optimization strategy in the flow cell and MEA, and managing water transport, particularly within the MEA, both within and between its various components; and the macro-scale, concerning device architecture design, the optimisation of overall operating conditions, and the optimisation of water management for large-scale electrolysis. Typical systems for multi-scale water regulation in the electrocatalytic CO_2RR (to C_1/C_{2+} products) and CORR (to C_{2+} products) are summarized in Table 1.

3.1. Catalyst-centered regulation approaches

At the micro-scale, the rational design of catalysts to precisely control water and proton dynamics is a cornerstone strategy for achieving high activity and product selectivity in CO_2/CO electroreduction. This section systematically reviews recent advancements in catalyst-centered micro-scale regulation (Fig. 10), which can be categorized into three primary approaches: (1) optimising the supply and distribution of water and the gaseous reactant (CO_2 or CO) at the catalyst–electrolyte interface (Fig. 10a), (2) promoting the controlled dissociation of water to generate protons at active sites (Fig. 10b and 11), and (3) regulating the subsequent transfer and coupling of these protons to key reaction intermediates (Fig. 10c). Importantly, a common outcome of these regulatory approaches is the simultaneous suppression of the competing HER.

Surface treatment/coating offers a direct approach to modulate catalyst wettability, primarily by introducing hydrophobic or hydrophilic functionalities (Fig. 10a, right side, 1). By constructing a thin and intact polymer layer on the surface of each catalyst particle, a water-repellent layer is formed through the introduction of hydrophobic organic groups, such as long-chain alkyls ($-C_nH_{2n+1}$), trifluoromethyl ($-CF_3$), or perfluoroalkyl moieties ($-C_nF_{2n+1}$).[121] This layer effectively minimizes the liquid film thickness to facilitate gas permeation and expand the triple-phase boundary (Fig. 4). Consequently, the optimized interfacial gas-to-H_2O ratio kinetically suppresses the competitive HER while preserving the requisite proton supply for efficient CO_2/CO reduction.[122] For instance, Wakerley *et al.* engineered superhydrophobic surfaces on hierarchical copper dendrites *via* octadecanethiol treatment. This modification efficiently captured gaseous CO_2 and dramatically improved the FE of ethylene and ethanol while suppressing the HER.[72] Chen *et al.* coated Cu nanoparticle catalysts with a highly fluorinated polymer (PT95), featuring excellent CO_2 adsorption, low water uptake (0.58 wt%), high porosity, and strong chemical stability.[74] This created and maintained an extremely low local H_2O/CO_2 ratio at the catalyst surface. In a flow cell for the CO_2RR, this catalyst achieved a FE exceeding 87% for C_{2+} products at an ultra-high current density of 2 A cm^{-2}. In a more nuanced approach, Liu *et al.* used self-assembled toluene molecules on Cu nanosheets to moderately control water transport. This strategy maintained CO_2 enrichment but also prevented catalyst corrosion and the HER, leading to a 78% C_{2+} FE with a total current density of approx. 0.8 A cm^{-2}.[73] Wei *et al.* fabricated a composite catalyst (Cu@F-S) by co-assembling a fluorinated self-assembled monolayer (F-SAM) with siloxanes on a commercial Cu surface. The F-SAM layer enhanced CO_2 mass transfer, and the siloxane network maintained optimal proton and electron transport, thereby reconstructing the TPB and hydrogen-bond network. This synergistic design optimizes the coverage of *H and *CO intermediates, achieving a FE exceeding 85% for C_{2+} products at a high current density of 502.5 mA cm^{-2} and maintaining stable operation for over 100 hours at approximately 300 mA cm^{-2}.[75] Conversely, Wang *et al.* incorporated hydrophilic polyethylene glycol (PEG) into a Cu_2O catalyst. By forming strong hydrogen bonds with water, the PEG disrupts the surface water network, which reduces local water activity and thereby inhibits the competing HER. The Cu-PEG electrode achieved a C_{2+} FE of 90.3% at 500 mA cm^{-2}, significantly outperforming the 69.3% FE from the standard Cu electrode under identical conditions.[76]

Beyond surface modification, tuning the physical architecture of the catalyst, specifically its porosity and nanomorphology, offers powerful, independent pathways for water management (Fig. 10a, right side, 2). Engineered porosity can exploit spatial confinement to selectively influence the permeation and diffusion of CO_2, thus providing a means to indirectly regulate the local water environment. Lee *et al.* systematically compared the performance of Ni–N–C catalysts with different pore structures (microporous, mesoporous, and macroporous), finding that mesoporous structures performed optimally for CO_2 to CO conversion in an MEA. By effectively regulating CO_2 mass transfer, this architecture optimised the local CO_2/H_2O ratio at the catalyst sites. This modulation simultaneously avoided both poor CO_2 accessibility in micropores and HER domination in thick macroporous layers. Ultimately, the

Table 1 Typical electrocatalytic multi-scale water regulation systems for the $CO_2RR/CORR$

Regulation category	System	Target products	Cell	FE (%) before/after	j (mA cm^{-2}) before/after	Stability (h) before/after	Ref.
Catalyst-centered (micro-scale)	Alkanethiol-modified Cu	CO_2RR-C_{2+}	H-cell	20/74	—/30	—/—	72
	Toluene-modified Cu NSs	CO_2RR-C_{2+}	MEA	30/78	300/600	50/400	73
	PT-coated CuNPs	CO_2RR-C_{2+}	Flow cell	60/85	500/1000	15/150	74
	F-SAM/siloxane-modified Cu	CO_2RR-C_{2+}	Flow cell	60/85	200/400	5/100	75
	PEG-modified Cu_2O	CO_2RR-C_{2+}	Flow cell	69/90	500/500	—/—	76
	Meso-Ni–N–C	CO_2RR-CO	MEA	85/95	25/150	—/50	77
	Cu needle-like array	CORR-C_{2+}	MEA	70/90	250/1000	—/20	78
	Leaf-like CuO NSs	CO_2RR-C_{2+}	MEA	35/76	150/300	—/35	79
	Co deposited Ag thin film	CO_2RR-CO	H-cell	56/91	9/9	—/12	80
	Ni NPs/Ni–N_x sites on C	CO_2RR-CO	Flow cell	—/93	—/50	—/—	81
	Ir-SA doped Cu_3N/CuO	CO_2RR-CH_4	Flow cell	34/75	270/320	—/0.5	82
	TCNQ-modified CuO	CORR-C_2H_4	MEA	60/75	300/500	—/120	83
	CeO_2–CuO	CO_2RR-C_{2+}	Flow cell	48/75	150/1200	—/—	84
	$Sm(OH)_3$–CuO	CO_2RR-C_{2+}	Flow cell	45/70	178/228	—/56	85
	Al_2O_3–CuO	CO_2RR-C_{2+}	Flow cell	58/78	500/500	—/8	86
	Cu_2O–Cu^0	CO_2RR-C_{2+}	MEA	—/80	—/1000	—/350	87
	F-modified Cu	CO_2RR-C_{2+}	Flow cell	40/84	—/—	—/40	88
	N-doped Cu	CO_2RR-C_{2+}	Flow cell	50/73	1100/850	—/6	89
	V_O-$Bi_2O_2CO_3$	CO_2RR-formate	Flow cell	—/90	—/35	—/8	90
	TS-Cu(III)	CO_2RR-C_{2+}	Flow cell	—/79	—/400	—/100	91
	Poly(amino acid)-modified Cu	CO_2RR-C_{2+}	Flow cell	—/90	—/200	—/10	92
	3D CIPH-Cu	CO_2RR-C_{2+}	Flow cell	50/75	100/800	—/60	93
	RF resin-coated Cu_2O NCs	CO_2RR-CH_4	Flow cell	—/51	—/1100	—/3	94
	PAHA-modified CuO	CO_2RR-C_2H_4	Flow cell	40/72	150/450	—/3	95
	DAT-modified Cu_2O NCs	CO_2RR-C_{2+}	Flow cell	70/86	800/800	24/24	96
	Bromophenyl modified Cu NPs	CO_2RR-C_{2+}	Flow cell	65/65	500/1000	—/—	97
	SnO@OMC-GDE	CO_2RR- formate	Flow cell	97.5/64.8	95/55	—/—	98
Electrolyte-centered (micro-scale)	High concentration electrolyte	CORR-C_{2+}	Flow cell	19/91	3/54	—/—	99
	Quaternary ammonium salt surfactants	CO_2RR- formate	—	10/40	—/—	—/—	100
	Aprotic organic additives	CO_2RR-CO	H-cell	72/99	—/—	5/8	101
GDE structural engineering (meso-scale)	MPL tuning	CO_2RR-CO	Flow cell	85/95	25/25	—/—	102
	Three-layer HG-M10/25/40 GDE	CO_2RR-CO	MEA	77/89	50/200	—/—	103
	Hydrophobicity-graded GDL	CO_2RR-CO	MEA	—/83	—/75	—/112	104
	Adding PTFE/CB to the catalyst layer	CO_2RR-C_{2+}	Flow cell	40/50	140/240	—/—	105
	Hydrophobic CB overlayer	CO_2RR-C_{2+}	Flow cell	73/63	200/800	—/27	106
	COF-PFSA overlayers	CO_2RR-C_{2+}	Flow cell	43/78	250/250	—/30	107
	PTFE membrane as the GDL	CO_2RR-C_2H_4	Flow cell	55/70	100/150	30/150	108
	Ultrathin porous Cu electrode	CO_2RR-C_{2+}	Flow cell	—/87	—/1800	—/10	109
	Raising the PTFE content in the MSL	CORR-C_2H_4	H-cell	25/53	8/22	—/24	110
MEA water transport management (meso-scale)	Cathode gas humidification	CO_2RR-CO	MEA	85/90	500/1000	—/110	111
	Tuning cathode PFSA content	CO_2RR-C_{2+}	MEA	55/68	500/600	—/—	112
	Tuning anolyte concentration	CO_2RR- C_2H_4	MEA	10/35	200/200	1/6	113
	Tuning anode hydrophobicity	CO_2RR- C_2H_4	MEA	5/32	200/350	—/—	114
	Tuning anode catalyst structure	CO_2RR-C_{2+}	MEA	60/80	/150	—/10	115
Device structure and operating condition optimisation (macro-scale)	Tuning stack structure	CO_2RR-CO	MEA	82/86	400/400	—/—	116
	Tuning membrane structure	CO_2RR-C_{1+}	MEA	60/90	200/800	—/—	61
	Non-isothermal electrode	CO_2RR-CO	MEA	70/80	100/100	3/200	117
	Multi-channel serpentine flow field	CO_2RR-CO	MEA	85/95	50/200	2/12	118
	Parylene-coated gas channels	CO_2RR-CO	MEA	80/90	200/200	100/500	119
	Active cooling channels	CO_2RR-C_{2+}	MEA	—/—	—/—	—/125	120

Note: F-SAM, NPs, PEG, NCs, SA, TS-Cu(III), RF resin, 3D CIBH, PAHA, DAT, WISE, PFSA, and CB stand for fluorinated self-assembled monolayer, nanoparticles, polyethylene glycol, nanocubes, single-atom, tension-strained copper-III, resorcinol-formaldehyde resin, 3D catalyst:ionomer bulk heterojunction, poly-*N*-(6-aminohexyl)acrylamide, diaminotriazole, water-in-salt electrolyte, perfluorosulfonic acid, and carbon black.

mesoporous catalyst achieved a CO FE of 90% at a total current density of 290 mA cm^{-2}, while the microporous and macroporous catalysts only reached a CO FE of 80% at approx. 100 mA cm^{-2}.[77] Similarly, Han *et al.* investigated the influence of carbon support pore diameters on Sn-based catalysts for the CO_2RR to form formate, identifying 5–20 nm mesopores (particularly in ordered mesoporous carbon) as the ideal range.[98] These pores provided a high surface area for abundant TPB reaction sites while their narrow dimensions created diffusion gradients that limited proton transport. Consequently, at −1.16 V *vs.* RHE, the ordered mesoporous carbon catalyst achieved a formate FE of 97.5%, significantly outperforming those based on microporous (64.8%) and moderate-mesoporous (73.3%) supports. In a different physical approach, high-curvature nanostructures such as tips and edges can induce potent local electric field enhancement effects (Fig. 10a, right side, 3). These intensified fields not only influence the migration and enrichment of charged species (*e.g.*, K^+) and intermediates but also actively regulate the orientation of water dipoles, thereby reorganizing the

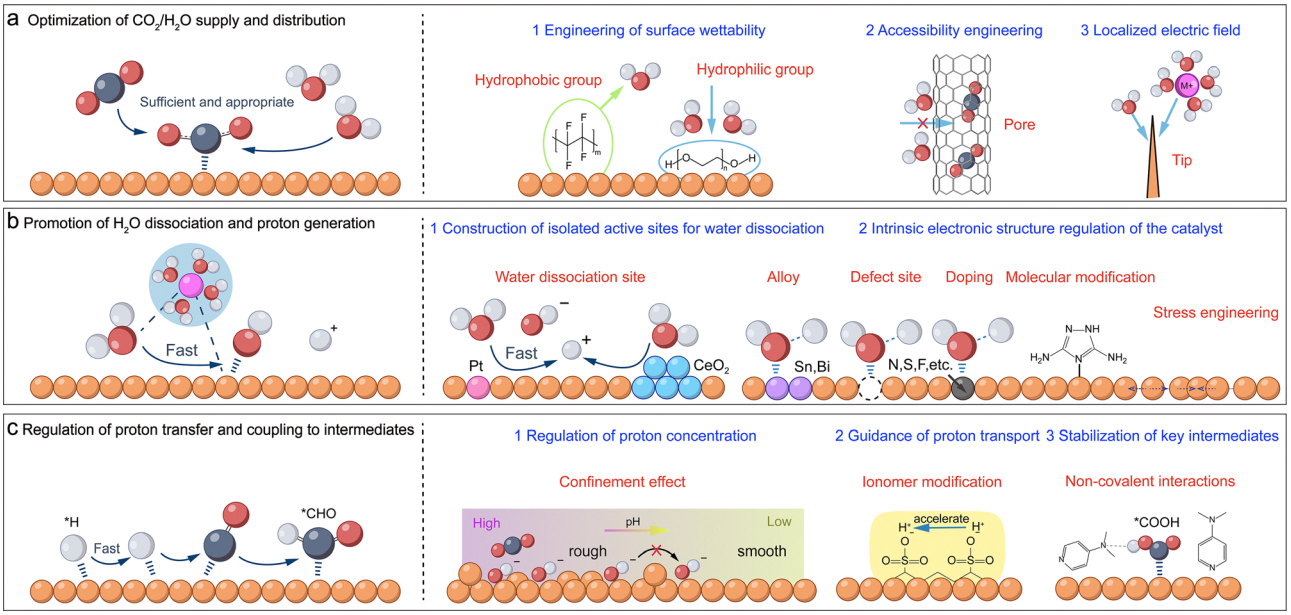

Fig. 10 Catalyst-centered water regulation strategies. (a) Optimising water/CO_2 supply and distribution. (b) Promoting water dissociation and proton generation. (c) Promoting proton transfer and coupling to intermediates. The orange, grey, red, and white spheres represent metal particles, carbon, oxygen, and hydrogen atoms, respectively.

interfacial water network and optimising the overall reaction environment. Guo *et al.* developed a dendritic Bi–Cu alloy (Bi–Cu-D) catalyst with high-curvature tips.[123] They found that the tip-effect-induced enrichment of K^+ ions led to reorganization of the interfacial water structure: Bi–Cu-D exhibited a significantly higher relative proportion of K^+-coordinated water (K-H_2O) compared to the low-curvature irregular Bi–Cu nanoparticles (Bi–Cu-NPs). This mechanism thus facilitates water dissociation and further provides active *H species for the CO_2RR. As a result, in the H-cell, at −1.8 V *vs.* RHE, the Bi–Cu-D catalyst achieved a total current density of 115 mA cm^{-2} with a formate FE of 90%, significantly outperforming the Bi–Cu-NPs (*ca.* 100 mA cm^{-2}). However, the non-selective cation enrichment induced by the tip effect also accumulates H^+, exacerbating the competing HER under acidic conditions. To address this, Wang *et al.* designed a carbon-encapsulated In_2O_3 catalyst with a tip-like morphology. The In_2O_3 tip promotes K^+ enrichment, while the carbon layer serves a critical dual function. It functions as an ion-sieve, selectively hindering H^+ migration while preserving K^+ enrichment, and as a protective layer, stabilizing the In_2O_3 sites against reductive corrosion. Consequently, even under harsh acidic (pH = 0.94) and low K^+ concentration (0.1 M) conditions, the catalyst achieved a HCOOH FE of 98.9% at 300 mA cm^{-2}. Notably, HER suppression was also significant at low current densities; for instance, at 50 mA cm^{-2}, the H_2 FE dropped to 16.9% (from 56.1% for the carbon-free counterpart).[124]

Precisely regulating water dissociation to enhance the selectivity of CO_2 reduction is a key scientific challenge. In the CO_2RR, promoting water dissociation is generally considered unfavorable, as it may lead to the competitive HER. However, water also serves as a proton source for hydrogenation processes, thereby influencing product distribution and reaction activity. Prior research by our group pioneered the experimental demonstration that promoting water dissociation can improve the performance of the CO_2RR to obtain formate.[125] Following this discovery, the precise regulation of water emerged as a pivotal strategy for enhancing electrocatalytic performance, stimulating extensive subsequent research. Currently, strategies to enhance reaction performance by promoting water dissociation can be categorized into two approaches: constructing independent water dissociation sites and modulating the intrinsic electronic structure of the catalyst (Fig. 10b). Specifically, the first approach is typically achieved by introducing a secondary component adjacent to the main active sites. This component, selected for high water dissociation activity but low intrinsic CO_2RR/CORR activity, then efficiently generates active hydrogen species (*H) or protons (H^+) that migrate to the nearby active centers. Typically, this is achieved by heterointerface formation with atomically dispersed metals with high activity for hydrogen evolution (such as Pt, Pd, Ir, Co, Ni, and Mn),[126–128] specific hydroxides (*e.g.*, $Sm(OH)_3$),[129,130] or strong Lewis acidic oxides (*e.g.*, CeO_2) (Fig. 10b, right side, 1).[131,132] Lee *et al.* showed that introducing oxophilic Co or Ni metal into Ag catalysts created water activation sites that accelerated H_2O dissociation to produce protons, thus providing an additional proton source for CO_2 reduction at Ag sites, exhibiting a typical dual-functional effect.[80] Similarly, Wang *et al.* designed a catalyst where nickel nanoparticles (NPs) were adjacent to atomically dispersed Ni@N_x sites. The Ni NPs served as efficient water dissociation centres, accelerating the generation of adsorbed hydrogen ($*H_{ads}$), which subsequently migrated to the adjacent Ni@N_x active sites, promoting intermediate protonation and thereby enhancing the conversion of CO_2 to CO.[81]

Chen *et al.* fabricated Ir single-atom doped Cu_3N/Cu_2O hybrids, with Ir sites acting as efficient water dissociation centers and feeding the produced protons to the active sites, thereby enhancing *CO to *CHO hydrogenation and selectively promoting methane (CH_4) formation.[82] Consequently, at −1.3 V *vs.* RHE, the Ir_1–Cu_3N/Cu_2O catalyst demonstrated a CH_4 FE of 75% at a total current density of 320 mA cm^{-2}, significantly outperforming the Cu_3N/Cu_2O catalyst (34% FE at 270 mA cm^{-2}). Transitioning to hetero-interfaces formed by oxides and hydroxides, these components offer versatile pathways for promoting water dissociation. Notably, a significant portion of these modifiers undergoes *in situ* reconstruction under CO_2RR conditions, while others remain structurally robust. Based on characterization results reported in existing research, these modifiers can be categorized into structurally robust promoters (*e.g.*, $Sm(OH)_3$, $La(OH)_3$, TiO_2, and MgO),[85,131,133,134] partially reduced species exhibiting valence or morphological reconstruction (*e.g.*, CeO_x, $Ce(OH)_x$, and $Ni(OH)_2$),[84,129,130] and coordination-reconfigured species (*e.g.*, Al_2O_3).[86] Consequently, these structural evolutions or the preservation of structural integrity directly determines the efficiency of water activation and the subsequent proton supply at the interface. In the following, we select representative components from each category to dissect these mechanisms.

Han *et al.* incorporated CeO_2 with CuO to create a dynamic hetero-interface. During the reaction, a portion of Ce^{4+} sites undergoes *in situ* reduction to Ce^{3+}, leading to the formation of an amorphous/crystalline mixed phase rich in oxygen vacancies. These Ce^{3+}-enriched regions significantly enhance water adsorption and activation, lowering the energy barrier for H–OH bond cleavage. This transformation ensures a sufficient proton supply, facilitating the key hydrogenation of *CO to *CHO. Simultaneously, the reconstructed CeO_x/Cu interface facilitates C–C coupling through a synergistic effect. Consequently, this synergistic effect boosted the C_{2+} FE from 48.3% (on the unmodified Cu catalyst) to 75.2%, while simultaneously elevating the corresponding total current density from 0.17 to 1.21 A cm^{-2} at −1.21 V *vs.* RHE.[84] Qi *et al.* anchored highly dispersed, small-sized $Sm(OH)_3$ onto the CuO surface to construct a structurally robust hetero-interface.[85] $Sm(OH)_3$ remains remarkably stable under CO_2RR conditions, maintaining its original hydroxide phase. Owing to its highly hydrophilic and polarized surface, $Sm(OH)_3$ significantly lowers the energy barrier for water dissociation, thereby driving a unique hydrogen spillover effect. This mechanism ensures a continuous supply of active hydrogen (H*) from the $Sm(OH)_3$ surface to the adjacent Cu sites, facilitating asymmetric C–C coupling. Consequently, this synergistic interface boosted the C_{2+} FE from 46.5% on the bare Cu catalyst to 77.2% at a high current density of 500 mA cm^{-2}. Hu *et al.* deposited a uniform Al_2O_3 layer onto the Cu surface *via* atomic layer deposition to construct a structurally robust hetero-interface.[86] While the Al_2O_3 layer maintains its structural integrity as a stable amorphous scaffold, its surface undergoes a rapid chemical evolution upon contact with the aqueous electrolyte during electrolysis. Specifically, the coordinatively unsaturated Al sites trigger immediate hydration to generate a high density of surface hydroxyl groups, accompanied by a dynamic rearrangement of the Al coordination environment. This localized chemical reconstruction significantly lowers the energy barrier for water dissociation, thereby creating a localized alkaline microenvironment with an ample proton supply. Consequently, this synergistic modulation boosted the C_{2+} FE from 45.1% on the bare Cu catalyst to 71.3% on the Al_2O_3/Cu electrode at the same potential, while achieving a total current density of 222 mA cm^{-2} in neutral 0.1 M $KHCO_3$.

A more direct approach involves modulating the intrinsic electronic/coordination environment of the catalyst itself to directly enhance its water dissociation capability and optimise the hydrogen adsorption energy. Common methods include heterogeneous atom doping, defect engineering, crystal engineering, and stress/strain engineering (Fig. 10b, right side, 2). For instance, introducing non-metallic (F, O, N, S, P, B, *etc.*) or other CO_2RR-active metallic dopants into the lattice of host metals (Cu, Sn, Bi, *etc.*) can effectively generate abundant heterogeneous interfaces or alter the d-band center, charge density, and coordination unsaturation of the central metal atom, thereby promoting the adsorption and subsequent dissociation of water molecules.[135] Specifically, these electronic modulations create localized electron-deficient regions or polar sites, which strengthen the interaction between the catalyst and the lone pair electrons on the oxygen atom of H_2O. This interaction polarizes and weakens the internal O–H bonds, facilitating water adsorption and lowering the activation barrier for dissociative H–O bond cleavage. Our team previously revealed that F modification of Cu catalysts promotes water dissociation (Fig. 11a).[88] The high electronegativity of F creates localized electron-deficient Cu sites ($Cu^{\delta+}$) that exert a strong coulombic attraction on the oxygen atom of H_2O. This interaction polarizes the O–H bond and lowers the dissociation barrier, thereby accelerating *CO hydrogenation to *CHO, as verified by spectroscopic experiments. Based on this, the study first proposed a *CHO coupling reaction pathway, which proceeds through the key *OHCCHO* intermediate, ultimately facilitating the formation of C_{2+} products, and revealed the H-assisted C–C coupling mechanism. In a flow cell, the catalyst achieved an ultrahigh current density of 1.6 A cm^{-2}, with a FE of 80% for C_{2+} products. In our recent study, we prepared nanocomposite catalysts enriched with Cu_2O–Cu^0 interfaces and demonstrated that Cu^+ species remained stable even under ampere-level current densities (Fig. 11b).[87] The oxophilic nature of Cu^+ species suggests a coordination with the oxygen atom of water, while neighboring surface oxygen species facilitate hydrogen-bond formation. This synergistic interaction is thought to lower the barrier for O–H bond cleavage, thereby promoting *CO hydrogenation to *CHO and subsequent C_{2+} product formation. In an MEA system, by co-feeding CO_2 and water at the cathode, we achieved a current density of 1 A cm^{-2} at a cell voltage of 3.8 V, with a FE for C_{2+} products reaching 80%. Yang *et al.* fabricated N-doped Cu catalysts to enhance *CO adsorption and water activation, which synergistically boosted both the FE and activity for the CO_2RR to form C_{2+}

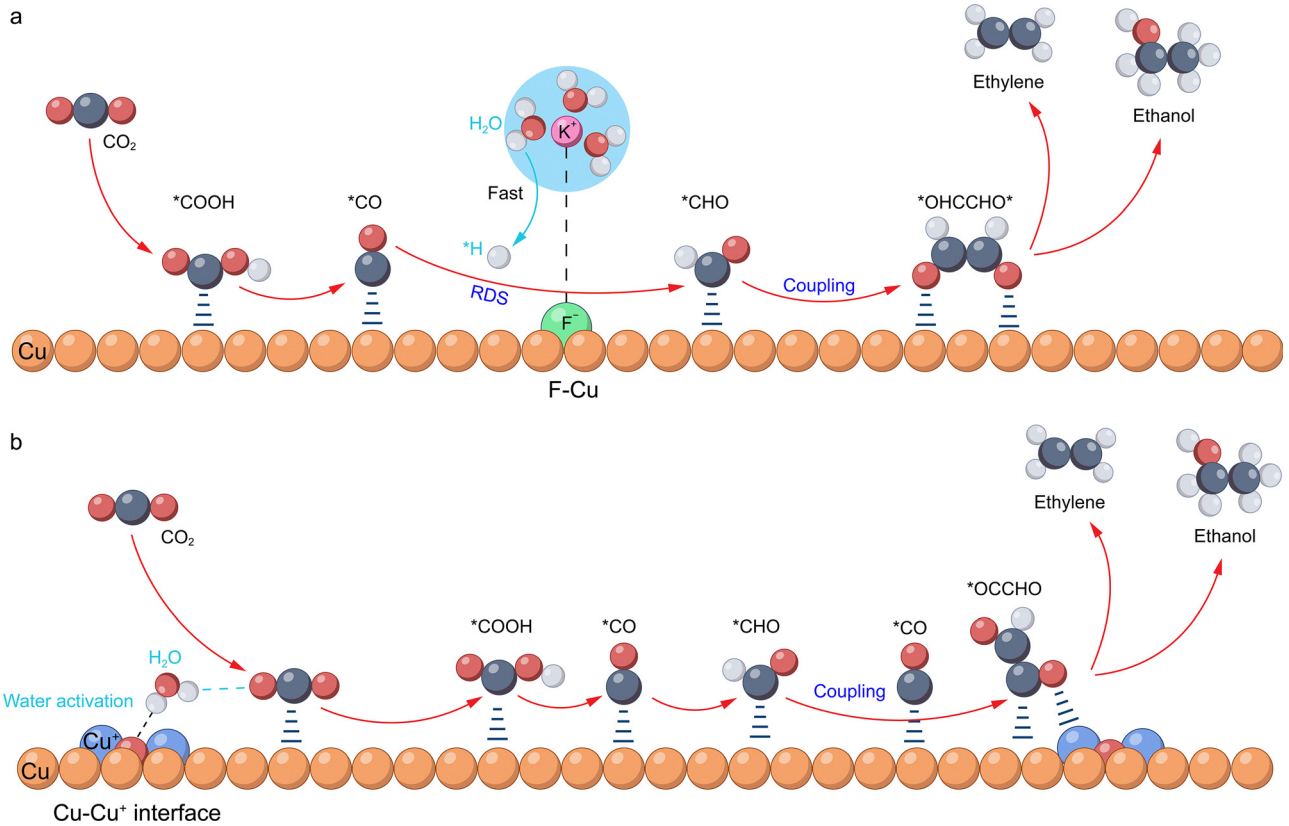

Fig. 11 Representative examples: specific reaction mechanisms for promoting water activation through catalyst design to boost the performance of the CO_2RR to obtain C_{2+} products. (a) A proposed reaction mechanism for the CO_2RR to form ethylene and ethanol through hydrogen-assisted C–C coupling over fluorine-modified copper. Reproduced with permission from ref. 88. Copyright 2020, Springer Nature. (b) A proposed reaction mechanism of the CO_2RR to form ethylene and ethanol with the water-promoting effect of abundant Cu_2O–Cu^0 interfaces. Reproduced with permission from ref. 87. Copyright 2024, Springer Nature. The orange, blue, grey, red, green, and white spheres represent Cu, Cu^+, carbon, oxygen, fluorine, and hydrogen atoms, respectively.

products.[89] Additionally, defect engineering, through the deliberate introduction of oxygen or metal vacancies, generates high-activity sites that optimize water adsorption energetics. These unsaturated, oxophilic vacancies function as Lewis acid sites that strengthen the metal–water (M–OH_2) interaction, facilitating O–H bond polarization and cleavage. For example, Chen *et al.* introduced moderate oxygen vacancies into $Bi_2O_2CO_3$ during electrodeposition synthesis. These oxygen vacancies exert a strong attractive force on the oxygen atom of H_2O, thereby lowering the activation energy barrier for its dissociation. By accelerating this crucial proton-supply step and ensuring a sufficient proton supply for CO_2 conversion, efficient formate generation is achieved.[90] Furthermore, stress/strain engineering offers a precise approach to modulate water adsorption energetics by shifting the d-band center and redistributing surface electron density. This can be achieved intrinsically, through methods such as inducing lattice mismatches, or extrinsically, by applying external stress to tune the properties of the catalyst. To address the challenge of suppressing the dominant HER in the acidic CO_2RR, particularly at low cation concentrations, Li *et al.* applied tensile strain engineering to Cu catalysts. They found that the lattice expansion enriched the electron density of the Cu surface, which in turn facilitated the enrichment of local K^+. The strong electrostatic field induced by these cations then disrupted the hydrogen-bonding network of the interfacial water, thereby hindering efficient proton transport *via* the Grotthuss mechanism and suppressing the HER, even in a strongly acidic electrolyte (pH = 1, 1 M K^+), ultimately promoting CO_2 activation. As a result, introducing 4% lattice strain into the Cu catalyst elevated the C_2H_4 FE to 50% at 300 mA cm^{-2}, compared to 28% for the non-strained catalyst.[91] Additionally, molecular modification to alter the electronic structure of catalysts can also promote water activation. In CO_2RR studies, Du *et al.* employed 3,5-diamino-1,2,4-triazole (DAT), rich in N–H groups, to modify the surface of Cu_2O nanocubes enriched with (100) facets.[96] In a flow cell, this catalyst achieved an 85.7% FE for C_2 products at a current density of 800 mA cm^{-2}. Further investigations revealed that the N–H groups in DAT interact with interfacial water *via* hydrogen bonding, lowering the energy barrier for water dissociation and generating active hydrogen species. These active hydrogen species facilitate the hydrogenation of *CO to form *CHO, followed by asymmetric coupling with *CO to form the key intermediate *OCCHO, thereby promoting the formation of C_2 products. Chang *et al.* employed a non-electrochemical aryl diazonium salt grafting method to *in situ* construct an

approximately 1 nm thick bromophenyl (Cu-PhBr) molecular layer on the surface of CuO_x nanoparticles.[97] This organic layer significantly enhanced the CO_2RR performance by synergistically regulating the interfacial water structure and cation environment. On one hand, it reorganized the hydrogen bonding network of interfacial water molecules, markedly reducing the proportion of strongly hydrogen-bonded water while increasing the proportion of weakly hydrogen-bonded water with higher reactivity, thereby accelerating water dissociation (Volmer step) in alkaline media to promote proton supply. On the other hand, it enhanced the local electric field by promoting the dehydration of alkali metal cations, thereby stabilizing C–C coupling intermediates with high dipole moments and inhibiting CO desorption. Consequently, in a flow cell, this catalyst achieved an ethylene partial current density of 530 mA cm^{-2} (a 7.4-fold increase over the bare copper electrode) and a total current density for C_{2+} products of 760 mA cm^{-2} (a 6.1-fold improvement) during the CO_2RR at −0.65 V *versus* RHE. In CORR research, Liang *et al.* introduced the strong electron-withdrawing molecule 7,7,8,8-tetracyanoquinodimethane (TCNQ) to modify CuO nanoparticles.[83] TCNQ withdraws electrons from the copper surface, rendering it electron-deficient under reaction conditions. In a flow cell, the modified catalyst attained a peak ethylene FE of 75% at a current density of 500 mA cm^{-2}, representing a 1.3-fold improvement over the unmodified catalyst (60%). Further studies indicated that this modification enhances water adsorption and dissociation, enriching the catalyst surface with *OH species. This thermodynamically favours the C–O bond cleavage in the key intermediate *CHCOH to form *CCH, ultimately directing the reaction pathway toward ethylene production.

The accessibility and concentration of protons, together with their interactions with key intermediates (*e.g.*, *CO, *CHO, and *OCCO), directly dictate product distribution (*e.g.*, C_1 *vs.* C_{2+}) and selectivity (Fig. 10c). Catalyst structure and surface modification can be employed to meticulously regulate these critical protonation steps. One regulatory strategy relies on creating nano-scale confinement effects to passively modulate the local pH and proton concentration (Fig. 10c, right side, 1). When catalyst surfaces are designed with nano-cavities, channels, or other recessed structures, these confined spaces physically restrict free ion diffusion. This leads to the local enrichment of OH^- or depletion of protons, thereby elevating the local pH.[92,136] Sargent *et al.* developed an EC-Cu catalyst prepared *via* a $Cu(OH)_x$-mediated *in situ* electrochemical deposition method.[76] This catalyst promotes the *in situ* formation of high concentrations of adsorbed *OH and *CO, significantly promoting C–C coupling under strongly acidic conditions, ultimately achieving a C_{2+} FE of 90% and an ethylene FE of 60% at 200 mA cm^{-2}. Alternatively, functionalized interfacial layers can be constructed on the catalyst surface to actively direct protons toward active sites.[43] These layers precisely control proton accessibility and concentration around the sites, thereby governing key proton-involved reaction steps (Fig. 10c, right side, 2).[76] This approach involves coating the catalyst with a functionally tailored polymer or organic layer that can operate through several distinct mechanisms. Firstly, it can precisely control the local proton flux by establishing efficient delivery pathways with proton-conductive groups. Fan *et al.* introduced a resorcinol-formaldehyde (RF) resin layer onto Cu_2O catalyst surfaces, with careful control over the polymerisation degree of the resin. They found that increased RF polymerization in the Cu_2O@RF catalyst reduced proton transfer resistance, thereby enhancing proton transport. They also observed that lower proton transport rates favoured C_{2+} product formation, whereas higher rates altered the reaction pathway, shifting products towards CH_4.[94] Secondly, these layers can modulate the local reaction environment by employing immobilising basic (*e.g.*, $-N^+(CH_3)_3$ and imidazole rings) or acidic (*e.g.*, –COOH and $-SO_3H$) functional groups.[122] For instance, a polyamine layer integrated onto a Cu electrode *via* co-electrodeposition not only increased the local pH at the catalyst surface through the basicity of amine groups and enhanced *CO adsorption, but also preferentially conducted protons whilst hindering OH^- diffusion. This led to local OH^- enrichment, achieving an ethylene selectivity as high as 87%.[95] Thirdly, introducing functional layers can steer reaction pathways by selectively stabilizing key intermediates through non-covalent interactions (Fig. 10c, right side, 3). For example, Fu *et al.* functionalized a copper catalyst derived from CuO nanosheets with 4-dimethylaminopyridine (DMAP) and then coated the surface with a hydrophobic poly(vinylidene fluoride-*co*-hexafluoropropylene) (PVDF-HFP) protective layer.[137] This protective layer successfully immobilized the DMAP molecules on the catalyst surface. In the CO_2RR conducted in a flow cell, this catalyst achieved a FE for ethanol approaching 50% at a current density of 400 mA cm^{-2}, far exceeding that of the pristine Cu catalyst (<20%). Mechanistic studies revealed that the nitrogen atom on the pyridine ring of DMAP, acting as an electron donor, forms hydrogen bonds with key oxygenated intermediates like *COOH and *CHCHOH. This interaction stabilises the reaction pathway towards ethanol, thereby significantly promoting its selective formation.

Targeting the critical bottlenecks of water-mediated intermediate loss and competitive HER in tandem CO_2RR, recent research has advanced several effective catalyst design strategies. At the nanoscale, the primary bottleneck is the diffusive loss of CO into the aqueous phase, which necessitates the minimization of transport distances. Li *et al.* engineered a dual-site cascade catalyst by co-loading CO-producing NiPc-OCH_3 and methanol-producing CoPc-NH_2 onto a single carbon-nanotube (CNT).[138] This design precisely confines the inter-site distance to the molecular scale (<2 nm), establishing an efficient short-range spillover channel. *In situ* sum frequency generation (SFG) spectroscopy confirmed that this ultra-short proximity ensures CO is captured by neighboring sites before desorbing, thereby significantly enhancing active *CO coverage on Co sites. Ultimately, this catalyst achieved a high methanol FE of 50% at a current density of 300 mA cm^{-2}. The critical necessity of such molecular-scale confinement is underscored by theoretical calculations, which determined that the aqueous diffusion layer thickness on the GDE is approximately 16 nm.

Consequently, in conventional physical mixing approaches where active sites are located on distinct supports, generated CO inevitably diffuses into the bulk electrolyte and is lost before it can bridge this gap to reach adjacent sites. While nanoscale tandem systems offer high efficiency, active sites are prone to reconstruction and agglomeration under operating conditions, leading to uncontrollable spacing.[139] In contrast, micro-scale hierarchically separated structures offer superior structural stability. To address the challenges of flooding and desorption inherent to macroscopic transport, Bian *et al.* constructed a hierarchical Ag–Cu nanowire-nitrogen-doped carbon (NC) tandem electrode on a hydrophobic PTFE membrane.[140] This was achieved by sequentially sputtering Ag and CuAl alloy layers, inducing the *in situ* growth of $Cu(OH)_2$ nanowires *via* etching and finally activating the structure through NC sputtering and electrochemical reduction. Specifically, the hydrophobic PTFE membrane substrate confines liquid water to the interface, preserving rapid gas–liquid transport channels that guarantee efficient CO diffusion from the Ag to the Cu layer. Simultaneously, the modification of Cu nanowires with a NC layer mitigates the weak adsorption of CO at the transport terminal by creating abundant NC–Cu interfaces. These interfaces not only enhance chemical CO trapping *via* linear adsorption but also effectively suppress the competitive HER, resulting in local CO enrichment and promoting C–C coupling. Consequently, this system achieved a C_{2+} FE of 87.5% at 519 mA cm^{-2}.

3.2. Electrolyte-centered regulation methods

Beyond the development of catalysts, the precise design of the electrolyte, including its composition, concentration, and additives, offers a powerful means to modulate the microenvironment at the electrode–electrolyte interphase. This modulation allows for the steering of reaction pathways at a molecular level, enabling precise control of the product selectivity of the CO_2RR. Given the roles of anions and cations, the strategies for their modulation have been extensively reviewed; this section will focus on innovative strategies within aqueous electrolyte systems.[47]

A prime example of such a strategy is the use of water-in-salt electrolytes. Zhang *et al.* used high salt concentrations (*e.g.*, 21 M $NaClO_4$) to thermodynamically regulate water activity (a_w).[34] By lowering the water activity, they effectively limited the supply of protons from water dissociation, which in turn suppressed reactions highly dependent on proton availability, such as the HER and methane formation (Fig. 12a). Meanwhile, this restricted water supply enhances the surface coverage of the *CO intermediate, which creates favourable conditions for subsequent C–C coupling. They identified an optimal water activity of approximately $a_w \approx 0.66$. Under these conditions, even on unoptimised copper catalysts, the FE for C_{2+} products can reach as high as 73% at −0.88 V *versus* RHE, with a total current density of approximately 150 mA cm^{-2}. Their work confirmed that regulating salt concentration to limit proton availability is an effective method to steer the reaction pathway C_1 to C_{2+} products. Crucially, while further reducing water activity continues to inhibit the HER and C_1 product formation, the total current density diminishes significantly when a_w falls below 0.66. This decline occurs because water is not only a proton source but also an indispensable reactant in the CO_2RR; excessively low water activity leads to mass transport limitations to the electrode surface, thereby constraining the overall reaction rate. Zhang *et al.* further investigated the impact of high-concentration electrolytes on the performance of the CORR.[99] The results showed that as the $NaClO_4$ concentration increased from 0.01 M to 10 M, the total current density for CO reduction rose from 3 mA cm^{-2} to 54 mA cm^{-2} at −1.43 V *versus* NHE. The total FE for C_{2+} dramatically increased from 19% to 91%, with C_2H_4 as the primary product; meanwhile, the FE for the HER decreased from 74% to 2%. The study demonstrated that high-concentration $NaClO_4$ electrolytes disrupt the hydrogen-bonding network of interfacial water, forming a disordered water layer structure. This disorder leads to a significant increase in the activation entropy (ΔS) for C–C coupling, where the resulting entropic driving force is sufficient to overcome the unfavourable enthalpy increase (ΔH) caused by elevated electrolyte concentration, ultimately enhancing the overall CORR performance.

Introducing quaternary ammonium salt surfactants ($(R_4N)^+X^-$) into the electrolyte enables dynamic self-assembly of ordered hydrophobic layers on the electrode surface under negative potential (Fig. 12b).[100] This hydrophobic layer effectively repels interfacial water molecules, lowering local proton concentration to suppress the HER. Furthermore, its lipophilicity enriches nonpolar CO_2 molecules, increasing their local concentration at reaction sites. Generally, longer alkyl chains exhibit stronger hydrophobicity, facilitating the formation of denser, more ordered assembled layers. Banerjee *et al.* showed that quaternary ammonium salts with longer alkyl chains, such as cetyltrimethylammonium bromide (CTAB), typically demonstrate optimal performance, particularly in promoting C_1 products like formate. It is worth noting that this strongly hydrophobic environment may impede C–C coupling, while the underlying mechanisms remain to be elucidated.[100]

The addition of aprotic organic co-solvents with a high Gutmann donor number (a quantitative measure of the Lewis basicity or electron-donating ability of a solvent), such as dimethyl sulfoxide (DMSO) or *N*,*N*-dimethylformamide (DMF), can effectively restructure the solvation shell of cations like K^+ (Fig. 12c).[101] Ni *et al.* reported that these organic molecules preferentially displace water from the primary solvation sphere of the cation. Consequently, these organics preferentially occupy the first solvation shell of cations like potassium and, along with the cations, become enriched in the Helmholtz layer, thereby establishing a dehydrated interfacial environment that suppresses the HER. Interestingly, these additives can also indirectly facilitate water dissociation and the protonation of CO_2 by stabilising adsorbed water and weakening the O–H bond, thus enhancing overall CO_2RR activity. Notably, in a KCl electrolyte containing 5 M DMSO, the FE for CO_2 reduction to CO on an Ag electrode reaches 99.2%, compared to only 70% without DMSO.

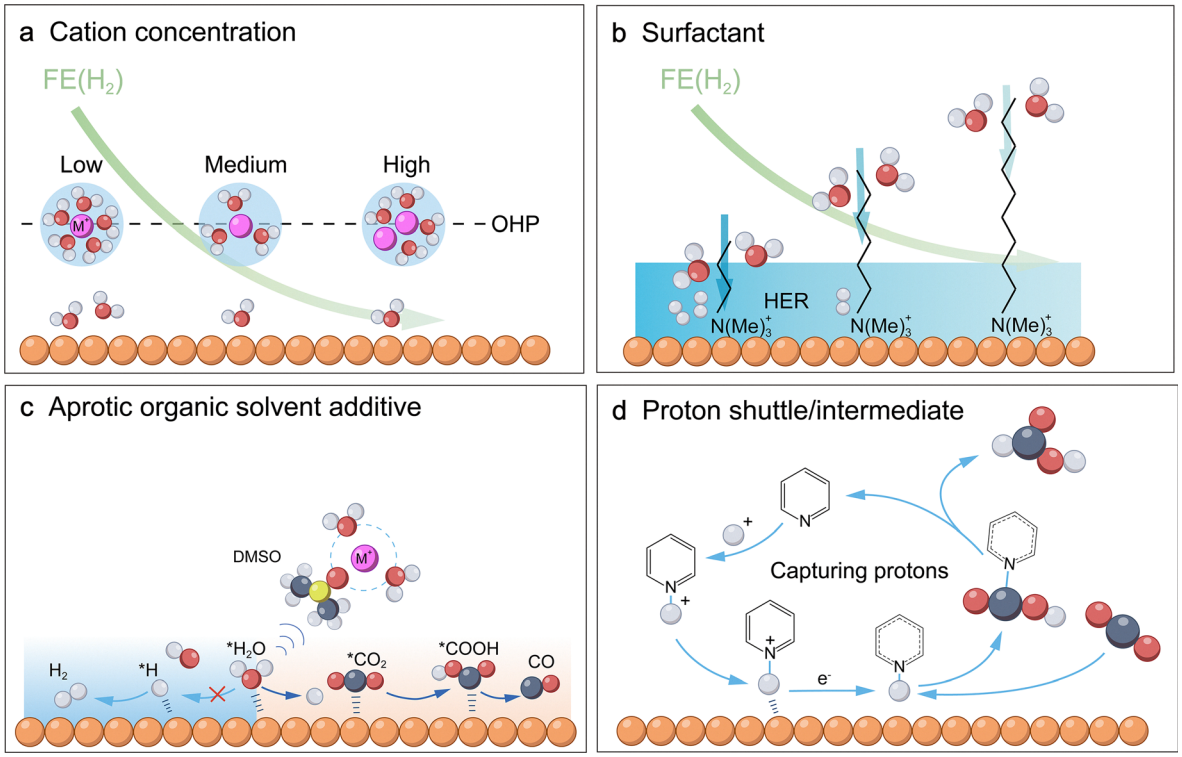

Fig. 12 Electrolyte-centered novel regulation method. (a) Cation concentration regulates water activity. The green curve indicates the H_2 FE as a function of water activity. (b) Surfactants regulate interfacial hydrophobicity. The green curve indicates the H_2 FE as a function of the alkyl chain length in the quaternary ammonium surfactant. (c) Using an aprotic solvent to regulate water dissociation promotes the CO_2RR to form CO. Reproduced with permission from ref. 101. Copyright 2023, John Wiley & Sons, Inc. (d) Promoting the targeted delivery of protons to CO_2 *via* a molecular shuttle to produce formic acid. The orange, grey, yellow, red, and white spheres represent metal particles, sulfur, carbon, oxygen, and hydrogen atoms, respectively. A green downward-sloping arrow indicates a gradual decrease in H_2 FE. FE, OHP, and HER stand for Faradaic efficiency, outer Helmholtz plane and hydrogen evolution reaction, respectively.

In contrast to the above strategies that suppress proton accessibility, an alternative and more advanced approach involves introducing specific molecules that act as proton shuttles, thereby establishing controlled pathways for proton transfer (Fig. 12d).[141] Adding Brønsted acids such as pyridinium ($C_5H_6N^+$) or imidazolium ($C_3H_5N_2^+$) to the electrolyte allows for *in situ* generation of highly reactive surface adsorbed hydrogen ($*H_{ads}$) *via* a PCET mechanism on catalyst surfaces like Pt. These $*H_{ads}$ then subsequently reduce CO_2 to formate. Rather than simply adjusting the overall proton concentration, this method offers a controlled and efficient route for proton delivery, providing directional control over CO_2 reduction product distribution.

3.3. GDE structural engineering

An ideal GDE must efficiently transport gaseous CO_2 to the catalyst surface while precisely managing water distribution and supply (Fig. 13a). A typical GDE consists of a macroporous support layer (MSL), a microporous layer (MPL), and a catalyst layer (CL) (Fig. 13b).[142] The primary challenge is managing water effectively to prevent GDE flooding and to construct a stable TPB within the catalyst layer. This approach involves engineering the pore structure and hydrophilicity/hydrophobicity of each layer to achieve the crucial balance between gas and water/ion transport (Fig. 4). This principle is particularly advantageous in a flow cell configuration.

Through a systematic evaluation of various commercially available carbon papers across multiple parameters, both Samu *et al.* and Wu *et al.* concluded that the MPL is essential for the GDE to attain superior CO_2RR performance.[102,143] Despite its designation, quantitative characterization by mercury intrusion porosimetry reveals that the MPL typically exhibits pore sizes ranging from 10 nm to 1000 nm, classifying it predominantly in the mesoporous-to-macroporous regime. Functionally, this specific hydrophobic architecture generates high capillary pressure to effectively inhibit liquid electrolyte permeation and prevent flooding, thereby preserving open gas pathways for efficient CO_2 mass transport. One key approach involves tuning the bulk and graded properties of the MPL. For instance, a thicker MPL offers superior CO_2RR performance and long-term stability at high current densities because it inhibits electrolyte penetration (Fig. 13b).[102] Wan *et al.* engineered an MPL with graded hydrophobicity, featuring pore sizes predominantly in the 30–100 nm range. By designing a hydrophilic side near the catalyst layer to maintain wetting and a hydrophobic side near the support layer to promote drainage, this structure generates a directional capillary force. This force actively removes excess electrolyte to prevent the blockage of gas diffusion channels,

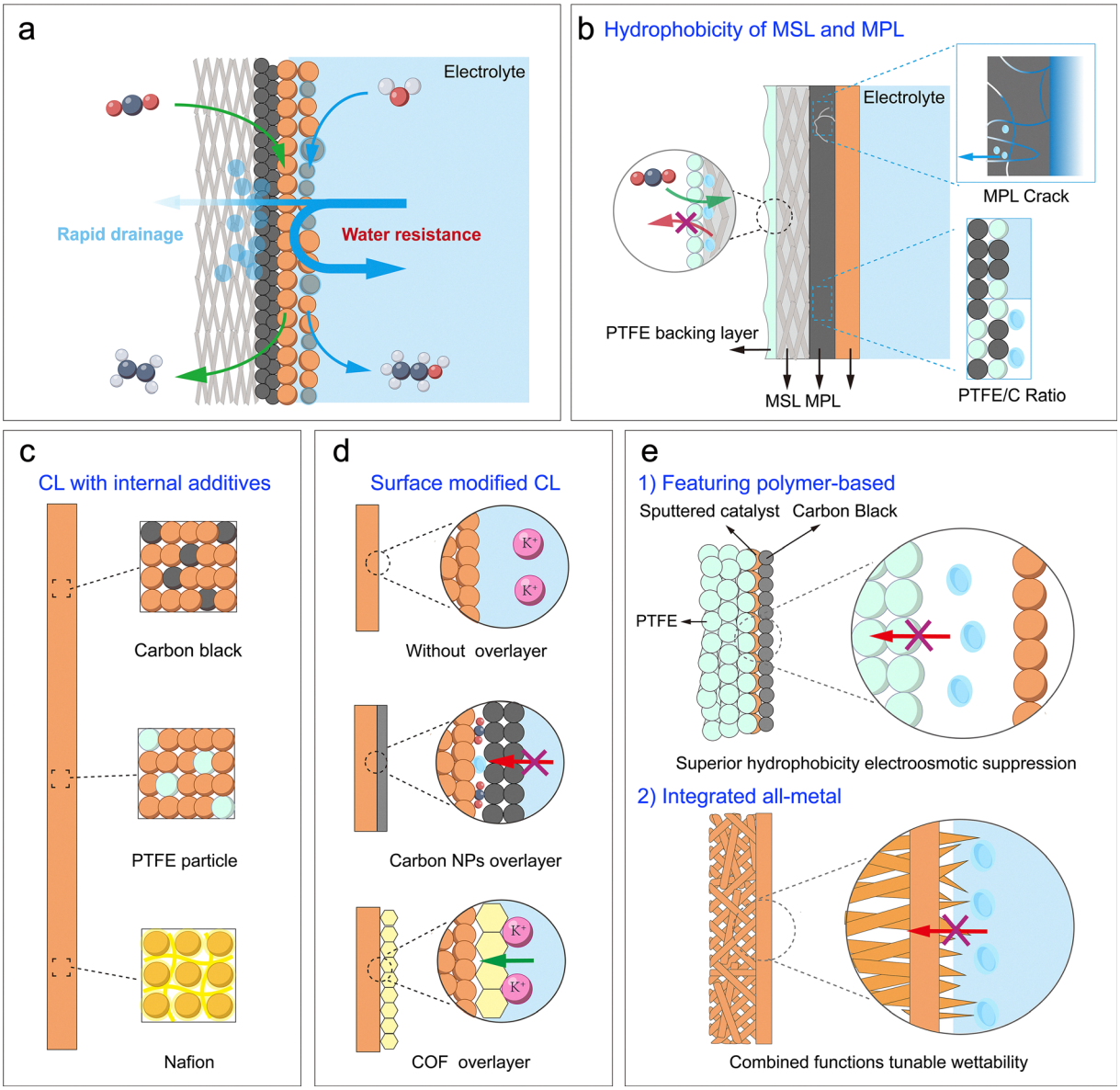

Fig. 13 Gas diffusion electrode (GDE) structure engineering. (a) Schematic of a conventional carbon-based GDE, illustrating fundamental gas and water transport pathways. (b) Hydrophobicity tuning of the macroporous support layer (MSL) and microporous layer (MPL). (c) Incorporation of functional additives within the catalyst layer (CL). (d) Application of a functional overlayer to the catalyst layer (CL). (e) Advanced carbon-free GDE designs, featuring polymer-based and integrated all-metal architectures. The orange, grey, red, and white spheres represent metal particles, carbon, oxygen, and hydrogen atoms, respectively.

thereby ensuring efficient CO_2 mass transport. Specifically, a GDE featuring a three-layer graded structure (HG-M10/25/40) demonstrated exceptional performance for the CO_2RR to form CO in an MEA. It achieved a current density of 209 mA cm^{-2} at 3.5 V in a pure water system, significantly outperforming single-layer designs.[103] Another strategy focuses on engineering the physical microstructure of the MPL. Counterintuitively, studies conducted by Kong *et al.* and Samu *et al.* revealed that the MPL with more numerous and larger cracks (typically 10–40 μm in width) actually exhibits better performance and stability. Functionally, these cracks decouple liquid water removal from gas supply. By channeling the rapid expulsion of liquid products, these fissures prevent the blockage of finer hydrophobic pores, thereby preserving unobstructed pathways for efficient CO_2 mass transport. This structural configuration critically mitigates flooding, which is especially beneficial in the MEA.[143,144] Beyond direct modifications to the MPL, engineering other components of the GDE provides another effective route for optimisation. For example, Li *et al.* demonstrated this by constructing a hydrophobic PTFE macroporous layer (PMPL) featuring a bridged macroporous network on the backside of the support layer. By leveraging its modest pore size to mitigate excess CO_2 input, this external layer effectively resisted electrolyte permeation and optimised gas management, extending the

operational lifetime of the GDE by more than 16 times while maintaining a CO FE above 83% for over 100 hours.[104]

Moving from the support structure to the active sites, the microstructural design of the catalyst layer itself is crucial for optimising the TPB by precisely regulating local water distribution (Fig. 13c). One direct approach is to introduce hydrophobic PTFE nanoparticles and carbon black, which are physically mixed with catalyst particles and fabricated into a composite catalyst layer. Although this method cannot precisely regulate the reaction microenvironment on the catalyst surface, it can form discontinuous and uneven hydrophobic regions around the catalyst, which create microscopic gas channels. This shortens diffusion pathways, nearly doubling both the reaction current density and conversion rate.[105] A more sophisticated strategy involves blending the catalyst with a specialized ionomer, like Nafion, which contains both hydrophobic and hydrophilic segments.[93] The self-assembly of this ionomer decouples the gas and ion transport pathways: the hydrophobic chains form a continuous gas transport network, whilst the hydrophilic chains establish ion transport channels. This design extends the effective reaction zone from a two-dimensional interface to the entire three-dimensional catalyst layer, successfully overcoming mass transport bottlenecks and boosting the ethylene FE to 70% at a total current density of 1.85 A cm^{-2}.[93]

Creating an additional functional overlayer at the interface between the catalyst and electrolyte enables further refinement of the water environment in the flow cell (Fig. 13d). For example, Kong *et al.* demonstrated that adding a hydrophobic carbon black (CB) overlayer above the catalyst layer allows for the quantitative adjustment of water flux to the catalyst surface, thereby optimising the local H_2O/CO_2 ratio. The optimal 6.6 μm thick CB overlayer not only achieved a C_{2+} FE of 63.2%, representing a 2.8-fold improvement compared to that without the CB layer, but also markedly enhanced the resistance to flooding and the long-term stability of the electrode.[106] For efficient C_{2+} product synthesis under strongly acidic conditions, Zhao *et al.* have fabricated composite interfacial modifier overlayers consisting of a covalent organic framework (COF) and a cation-exchange (PFSA, perfluorosulfonic Acid) ionomer. This layer serves dual functions: acting as an efficient proton filter to limit proton penetration to the catalyst surface, creating a locally high-pH environment, and utilising specific COF functional groups, such as carbonyls, to enrich key cations that promote C–C coupling. Ultimately, in a strongly acidic electrolyte (pH = 1), the FE for C_{2+} products as high as 75% was achieved at a current density of 200 mA cm^{-2}.[107]

Traditional carbon-based GDEs suffer from critical stability issues. They are prone to corrosion at high potential or under strongly alkaline operating conditions and are susceptible to electro-wetting, where the electrode surface becomes more hydrophilic with applied potential. This leads to flooding and rapid deactivation at high current densities.[142] To overcome these limitations, research has shifted towards novel carbon-free GDEs, with polymer-based designs representing a key strategy (Fig. 13e). These GDEs utilise inherently hydrophobic porous polymer membranes, such as PTFE or PVDF (polyvinylidene fluoride), as the gas diffusion layers to effectively resist electrolyte penetration.[142] For example, Tang *et al.* constructed a sandwich structure GDE, using a PTFE membrane as the hydrophobic gas diffusion layer, sequentially sputtering a copper catalyst, carbon nanoparticles, and a graphite current collector. By decoupling the functions of gas transport and electron conduction, they achieved stable operation at approximately 100 mA cm^{-2} for 150 hours, far exceeding traditional carbon-based GDEs, which failed within 1 hour.[108] However, the inherent insulating nature of polymers often results in insufficient electrical conductivity, presenting a new challenge. Consequently, researchers have further developed hydrophobically modified all-metal GDEs. These designs utilise a single, conductive metal matrix that serves multiple roles as the catalyst, gas diffusion layer, and current collector. For instance, Sun *et al.* fabricated an ultrathin (0.1 μm) porous copper electrode. Following electrochemical oxidation and modification with 1-octanethiol, it formed a superhydrophobic nanoneedle structure, achieving 87% FE for C_{2+} products with a total current density of 1.84 A cm^{-2} under acidic conditions.[109] Although GDE research primarily concentrates on the CO_2RR, particularly in the flow cell, the CORR is not only equally highly dependent on GDE hydrophobicity tuning, but its performance is also more significantly sensitive to alkaline environments. A study conducted by Chen *et al.* significantly enhanced the performance of CO reduction to ethylene through systematic optimisation of the GDE.[110] Utilising metallic copper particles (Cu-Ps) as the catalyst, they progressively increased the hydrophobicity of the electrode by raising the PTFE content in the MSL and introducing an MPL. In the H-cell operating in 1 M KOH electrolyte, this strategy led to a dramatic increase in FE for C_2H_4, rising from 2.46% on a less hydrophobic carbon paper (CP-5%) to a final 52.7% on the optimised CP-MPL support at total current densities of 20 and 28 mA cm^{-2}, respectively. Concurrently, the partial current density for ethylene reached 14.9 mA cm^{-2} under these optimised conditions.

Recently, substantial advances have been made in enhancing the stability of CO_2RR/CORR systems at low current densities (<200 mA cm^{-2}) through various GDE layer modifications. However, the transition toward industrially relevant high current densities (>500 mA cm^{-2}) presents a severe challenge, where dynamic, multiphysics-coupled failure modes are drastically intensified. Specifically, the stability of the interface is undermined by a combination of factors: the electro-osmotic drag of hydrated cations into the electrode depth, electrowetting caused by high potentials, chemical wetting due to alcohol product accumulation, and the formation of hydrophilic pathways *via in situ* carbonate precipitation. Consequently, building upon the ensured structural integrity of the catalyst, design principles for GDEs operating at high currents must evolve toward the construction of hierarchically ordered hydrophobic architectures (Fig. 13a). At the electrolyte interface, such as the catalyst layer or overlayer, the priority is to construct a dense microscopic interface with high water entry pressure (WEP) to preemptively block electrolyte intrusion at the source. Simultaneously, for water and liquid products that

inevitably penetrate into the support layers (MPL/GDL), ordered low-resistance drainage pathways must be engineered. This structural design facilitates the rapid expulsion of accumulated fluids, thereby sustaining the efficacy of the triple-phase boundary under intense reaction conditions.

3.4. Water transport management in MEAs

It is noteworthy that the importance of macroscopic water management varies among different electrolyser configurations, given that MEA systems typically utilize humidified gas feeds (unless otherwise specified), while flow cells do not. Consequently, the mechanism of water management in MEAs is considerably more complex and indirect compared to that in the flow cell (Fig. 14a and e). Studies conducted by Ren *et al.* on the CORR have clearly highlighted this distinction under non-humidified conditions.[111] In a flow cell configuration, using Nafion as the ionomer wrapping copper catalysts can effectively enhance CORR activity. Increasing catalyst loading from 0.2 to 1.2 mg cm^{-2} results in a thicker catalyst layer with more active sites, thereby improving performance (Fig. 14b). In stark contrast to flow cell systems, the performance of MEA does not continuously improve with increased catalyst loading. While a higher loading provides more active sites, mass transport limitations become severe at high current densities (*ca.* 400 mA cm^{-2}). For instance, increasing the catalyst loading from 0.2 to 0.8 mg cm^{-2} already reveals these limitations, and a further increase to 1.2 mg cm^{-2} leads to a pronounced performance decline (Fig. 14c). Replacing the Nafion ionomer with a hydrophilic anion-exchange ionomer (*e.g.*, XA-9 or Pention) significantly boosts reaction performance (Fig. 14d). This demonstrates that in MEAs, utilising a thicker cathode catalyst layer, Nafion severely impedes the effective transport of OH^- and water. Furthermore, research conducted by Reyes *et al.* has provided in-depth insights into the cathode water supply mechanism in MEAs, emphasising that maintaining the net water flux at the cathode to around 5 mg cm^{-2} h^{-1} contributes to superior performance in the CO_2RR to form CO.[145] In MEAs, the water around the cathode is primarily supplied through transmembrane diffusion (J_{DFF}) from the anode and by humidifying the feed gas, whilst water loss includes back-diffusion (J_{BD}) and electro-osmotic drag (J_{EOD}) from the cathode to the anode (Fig. 14e). The actual water content available for cathode reactions is governed by the balance of these fluxes ($J_{H_2O,Net}$). Key factors influencing the net cathode water flux include the thickness and water uptake capacity of the anion exchange membrane (AEM) and the hydrophobicity of the cathode GDE. Concurrent studies on Ag catalysts have shown that CO_2RR activity and CO FE can be substantially enhanced by mitigating GDE flooding. This is accomplished by reducing the net water flux at the cathode through a synergistic combination of a thinner AEM, higher membrane water uptake, and enhanced GDE hydrophobicity (Fig. 14f and g). Moreover, Saha *et al.* demonstrated that anolyte plays a key role in regulating the cathode water environment in the MEA.[146] The crossover of concentrated electrolyte significantly enhances the water inventory within the porous electrode structure, improving hydration and establishing continuous ion transport channels. This effectively activates deep catalytic sites, leading to a substantial increase in electrochemically active surface area (ECSA) and ionic conductivity. Despite the different electrolyte introduction methods in MEAs (crossover) *versus* flow cells (direct contact), both systems follow similar interfacial regulation effects under non-mass-transport-limited conditions (*i.e.*, at low current densities). The trade-off between electrolyte concentration and cathode hydrophobicity (ionomer content) jointly determines interfacial wetting. Consequently, despite the current lack of systematic studies regarding anolyte concentration effects in MEAs, it is reasonable to extrapolate findings from the flow cell to the MEA system to discuss the effects of anolyte regulation on performance. Research by Giron Rodriguez *et al.* on the CO_2RR conducted in the flow cell over copper catalysts clearly illustrates this relationship.[112] Operating at a fixed current density of 200 mA cm^{-2}, they observed that a catalyst layer with low (10%) Nafion content was highly sensitive to the concentration of the catholyte. Increasing the bicarbonate ($KHCO_3$) concentration from 0.1 M to 3 M triggered a dramatic shift in FE away from C_{2+} products and towards C_1 products. The underlying cause is an increased flux of water to the cathode at high salt concentrations,[113] leading to excessive wetting of the catalyst layer that is unfavourable for C–C coupling. However, this sensitivity to the catholyte can be mitigated by increasing the hydrophobicity of the cathodic catalyst layer. When the Nafion content was increased to 50%, the negative impact of high catholyte concentration on C_{2+} FE was markedly reduced (Fig. 14h). These results demonstrate that increasing the Nafion content creates a more hydrophobic catalyst layer, which in turn shields the active sites from excess water flux. Beyond external optimisation, the intrinsic catalytic properties, particularly its ability to activate water, can also influence water management in MEAs.[147] Ren *et al.* synthesized a series of Cu-based catalysts *via* a one-step solvothermal method, achieving a morphological transition from nanocubes to needle-like arrays by modulating the reaction temperature. These catalysts exhibited robust FE for C_{2+} products in a flow cell during the CORR at 1 A cm^{-2}. However, in the MEA, the C_{2+} FE progressively improved with increasing catalyst curvature (*i.e.*, from cubes to needles). Consequently, the performance gap relative to flow cells at equivalent current densities narrowed and was eventually eliminated. The needle-2 catalyst demonstrated optimal performance, primarily attributable to its tip-enhanced electric field, which concentrated limited K^+ cations at the catalyst tips within the dehydrated MEA interface. Concurrently, this intensified electric field facilitated water uptake through electroosmosis, effectively mitigating K^+ and water depletion at elevated current densities. This advancement significantly enhanced CORR performance in MEAs, culminating in an ultrahigh current density of 2.5 A cm^{-2} at a full-cell voltage of merely 2.7 V.[78]

In a traditional flow cell, the cathode reaction microenvironment is effectively decoupled from the anode reaction microenvironment by the catholyte chamber through the flowing catholyte. Consequently, the anodic OER is generally

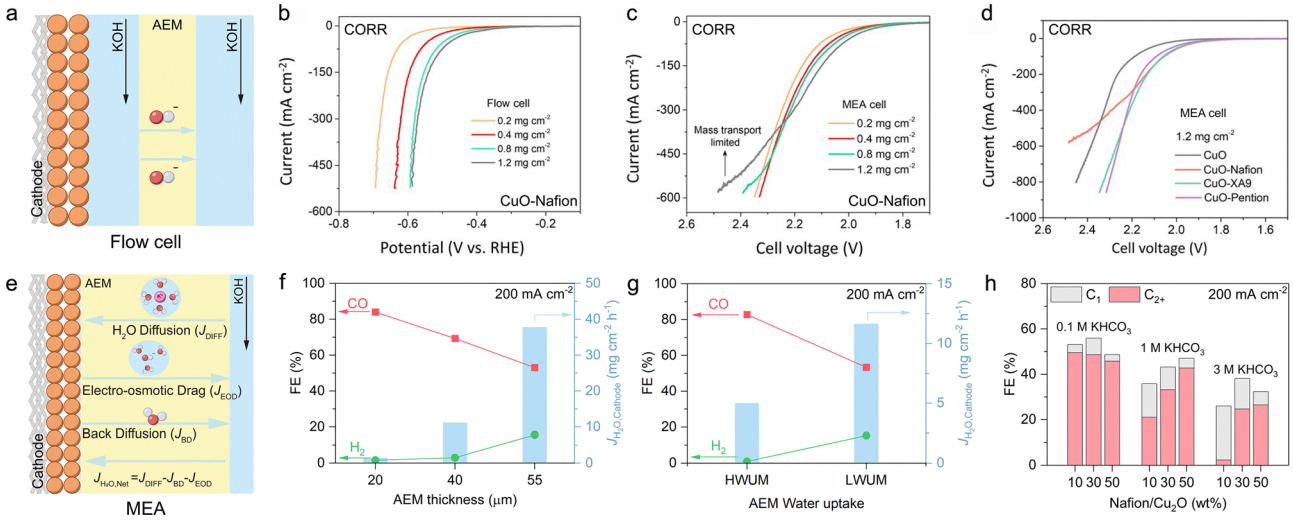

Fig. 14 Water transport management in flow cell and MEA systems. (a) Schematic diagram of water transmission path in a flow cell. (b) LSV curves of CuO-Nafion with different loadings in a flow cell at 10 mV s^{-1} with 1 M KOH. (c) LSV curves of a MEA electrolyser at 10 mV s^{-1} with 1 M KOH as the anolyte, CuO-Nafion as the cathode, and NiFe on Ni foam as the anode. (d) Comparison of LSV curves of CuO, CuO-Nafion, CuO-Pention, and CuO-XA-9 at 1.2 mg cm^{-2} in MEAs. Reproduced with permission from ref. 111. Copyright 2023, Elsevier. (e) Schematic diagram of the water transmission path in an MEA. (f) Effect of low water uptake membranes (LWUMs) with different thicknesses (20, 40, and 55 μm) on the flux of water to the cathode ($J_{H_2O,cathode}$) and CO_2RR performance. (g) Water flux to the cathode ($J_{H_2O,cathode}$) and CO_2RR performance for MEAs with a 55 μm thick high water uptake membrane (HWUM) and LWUM. Reproduced with permission from ref. 145. Copyright 2020, American Chemical Society. (h) Effect of variations in $KHCO_3$ concentration on the CO_2RR selectivity towards C_{2+} and C_1 products using 50 wt%, 30 wt% and 10 wt% Nafion. Reproduced with permission from ref. 112. Copyright 2021, Royal Society of Chemistry. The orange, grey, red, and white spheres represent metal particles, carbon, oxygen, and hydrogen atoms, respectively. AEM stands for the anion exchange membrane.

considered to have no significant influence on the product FE of the CO_2RR/CORR. In an MEA, however, the anode can actively influence the cathodic reaction environment by regulating water and ion transport, as revealed by the recent work of Kim *et al.*, thereby modulating the activity and product selectivity of the CO_2RR.[114] Their study maintained other conditions constant and compared two anode substrates loaded with IrO_2: a hydrophilic, macroporous platinum-coated titanium mesh (TM) and a hydrophobic, microporous carbon paper (CP) (Fig. 15a). The CO_2RR performance showed that the cell voltage with the TM anode was consistently lower than that with the CP anode across the investigated current density range, with the difference increasing at higher current densities (Fig. 15b). Regarding product FE, at low current densities (100–200 mA cm^{-2}), the FE for ethylene on CP was higher than that on TM. However, at higher current densities (250–400 mA cm^{-2}), TM exhibited substantially higher FE for ethylene, lower FE for H_2, and greater overall FE for the CO_2RR products (CO + C_2H_4), with these differences becoming more pronounced as current density increased (Fig. 15c). *In situ* characterization and visualization analyses confirmed that the CP anode, due to its structural properties, significantly suppressed the transmembrane transport of water and K^+ to the cathode, resulting in a relatively ion-deficient and water-deficient environment at the cathode. This environment exacerbated the local pH elevation at the cathode and stabilized oxidized copper species, which are believed to favour ethylene production. While this strategy enhanced the FE of ethylene at low current densities, it led to severe mass transport limitations and uneven reaction distribution at high current densities, ultimately reducing overall performance. Similarly, Ma *et al.* investigated the role of anode physical structure in regulating CO_2RR performance in MEAs.[115] They designed and compared two anode configurations loaded with a $NiFeO_x$ catalyst: one with porous, rough-surfaced nickel foam (NF) in direct contact with the ion exchange membrane, backed by a nickel net (NN) (NF/NN), and another with a smoother, denser-contact NN in direct contact with the membrane, backed by NF (NN (with a catalyst)/NF) (Fig. 15d). Their findings revealed that optimizing the physical contact between the anode and the membrane using the NN (with a catalyst)/NF structure not only significantly enhanced CO_2RR activity but also substantially reduced the H_2 FE within a current density range of 50–250 mA cm^{-2} (Fig. 15e and f). Characterization showed that the sparse and non-uniform contact points of the NF/NN structure facilitated the formation of a thicker liquid film or gap at the membrane–cathode interface. In contrast, the NN/NF structure markedly improved interfacial conformity and reduced the liquid film thickness. Simulations and theoretical calculations further indicated that thinning this liquid layer raised the local pH at the cathode catalyst surface, thereby suppressing the HER and enhancing the FE of C_{2+} products. Furthermore, the study found that removing the $NiFeO_x$ catalyst from the NN in direct contact with the membrane while retaining it only on the rear NF (*i.e.*, transitioning from NN (with a catalyst)/NF to NN (without a catalyst)/NF) resulted in higher operating voltage and H_2 FE at the same current density (Fig. 15d–f). Notably, the introduction of the $NiFeO_x$ catalyst typically does not

significantly alter the hydrophobicity of the electrode. This result suggests that enhancing the kinetics of the OER can indirectly optimize the overall water and ion transport environment within the MEA, thereby positively impacting cathodic CO_2RR performance.

3.5. Device architecture design and operating condition optimisation

Unlike flow cells, which benefit from an abundant supply of liquid water, the MEAs exhibit much greater sensitivity to these strategies.[148] Any adjustment to water management at the macro-scale in MEAs directly and markedly impacts the construction of the gas–liquid–solid TPB and the transport efficiency of key reactants. Consequently, research into macroscopic water management is predominantly focused on MEA systems.

Currently, various macroscopic regulation methods are employed to optimise water management in MEAs. For instance, regulating the thermodynamic state of water to indirectly manage ion behaviour has been explored. In highly alkaline electrolytes, the carbonate or bicarbonate formed on the cathode side leads to GDE blockage and limits CO_2 mass transport. To address this, Li *et al.* proposed an innovative strategy that coupled a cold cathode with a hot anode to form a non-isothermal system (Fig. 16a).[117] This strategy utilises the Soret effect, whereby a temperature gradient drives K^+ ions within the aqueous medium from the cold cathode towards the hot anode, with water facilitating ion transport and maintaining a stable hydration environment. This effectively counteracts their enrichment at the cathode due to the electric field, thereby preventing salt oversaturation and precipitation. For CO_2 reduction to CO in a 1 M KOH anolyte, this approach demonstrated remarkable stability, operating at a current density of 100 mA cm^{-2} for over 200 hours without salt precipitation, in stark contrast to conventional isothermal systems, which failed within a few hours. Concurrently, a hot anode (>60 °C) can enhance OER kinetics, whilst a cold cathode (<40 °C) is beneficial for increasing CO_2 solubility, suppressing the HER, and reducing water evaporation. In traditional isothermal operations, the operating temperature is a critical parameter that directly regulates a suite of physical phenomena, including water/ion transport, CO_2 solubility and diffusion, and the properties of water such as activity and saturated vapor pressure. These factors collectively determine the overall activity and product FE of the CO_2RR. This presents a trade-off, as higher temperatures that enhance mass transport also accelerate water evaporation. For example, Giron Rodriguez *et al.* systematically investigated the effect of operating temperature on CO_2RR performance of copper-based catalysts in MEAs (Fig. 16b).[149] In the low-temperature region (<50 °C), the slow rate of water evaporation biases the reaction towards C_{2+} products (*e.g.*, ethylene and ethanol) over CO, but the system is prone to flooding at high current densities, which blocks GDE pores and promotes the HER. As the temperature increases into the mid-temperature range (50–60 °C), a water balance is achieved. Here, accelerated water evaporation removes excess water promptly, alleviating flooding, improving CO_2 transport, and suppressing the HER. However, the product shifts dramatically from C_{2+} to CO. This window represents an optimal dynamic equilibrium between water inflow and outflow.

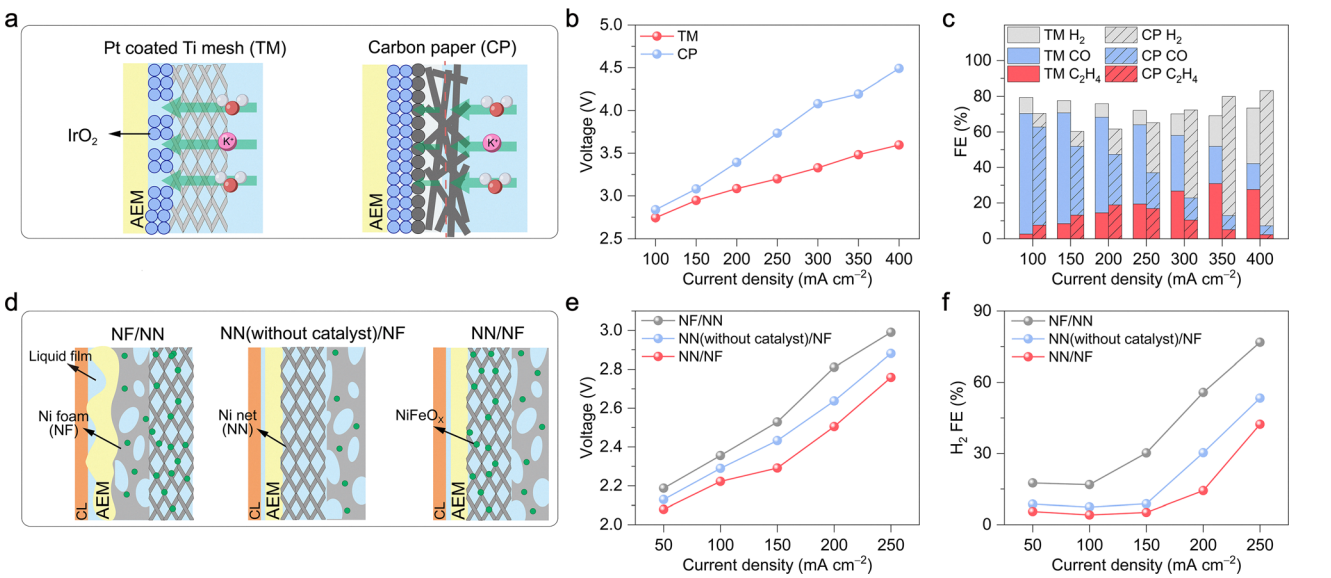

Fig. 15 The influence of anode configuration in MEAs on CO_2RR performance. (a) Schematic of the influence of the iridium oxide (IrO_2) anode supported on titanium mesh (TM) and carbon paper (CP) on water and K^+ transport to the cathode. (b) The cell voltage of the CO_2RR at different current densities on TM and CP anodes. (c) The product distribution of the CO_2RR at different current densities on titanium mesh (TM) and carbon paper (CP) anodes. Reproduced with permission from ref. 114. Copyright 2024, Elsevier. (d) Schematic of the placement of NF/NN, NN (without a catalyst)/NF, and NN/NF composite anodes and their influence on the structure near the AEM. (e) The cell voltage of the CO_2RR at different current densities on NF/NN, NN (without a catalyst)/NF, and NN/NF anodes. (f) The H_2 FE of the CO_2RR at different current densities on NF/NN, NN (without catalyst)/NF, and NN/NF anodes. Reproduced with permission from ref. 115. Copyright 2024, Royal Society of Chemistry.

Entering the high-temperature region (>60 °C), the increased saturated vapour pressure of water dilutes the gaseous CO_2 concentration. Simultaneously, excessively high temperatures can easily cause the AEM dehydration, increasing Ohmic losses and affecting the long-term stability of the AEM. Furthermore, temperature also directly affects the intrinsic reaction thermodynamics and kinetics of the catalyst.[150]

The geometry of the cathode flow field also directly influences the distribution uniformity of reactant CO_2 and the removal of water (Fig. 16c), thereby impacting the performance of CO_2RR in MEAs at high current densities.[118] Usually, when the reactant gas supplied to the cathode is not humidified, the source of water in the cathode mainly relies on diffusion from the anode. As the reactant gas flow passes through the reaction sites, it carries away some of the diffused water. Therefore, the longer the path the reactant gas flow has traveled, the higher the relative water content in the gas flow at that position, typically increasing closer to the outlet. However, in flow fields of different structures, there are significant differences in the distribution of relative water content in the gas flow at various positions (Fig. 16c).[151–153] In a systematic investigation, Yuan *et al.* highlighted the distinct trade-off of conventional designs.[118] They found that simple parallel channels are prone to CO_2 starvation in the center at high currents. In contrast, interdigitated channels, which use forced convection to enhance mass transfer, can be difficult to manage, risking either excessive water removal or channel flooding, leading to instability. Standard serpentine channels were found to offer a better overall balance. Further optimisation revealed that a multi-channel serpentine flow field provides the most robust performance. This advanced design ensures uniform CO_2 supply across the electrode with gentle flow gradients, a combination that inhibits excessive water removal and facilitates superior water and mass management. As a result, using this

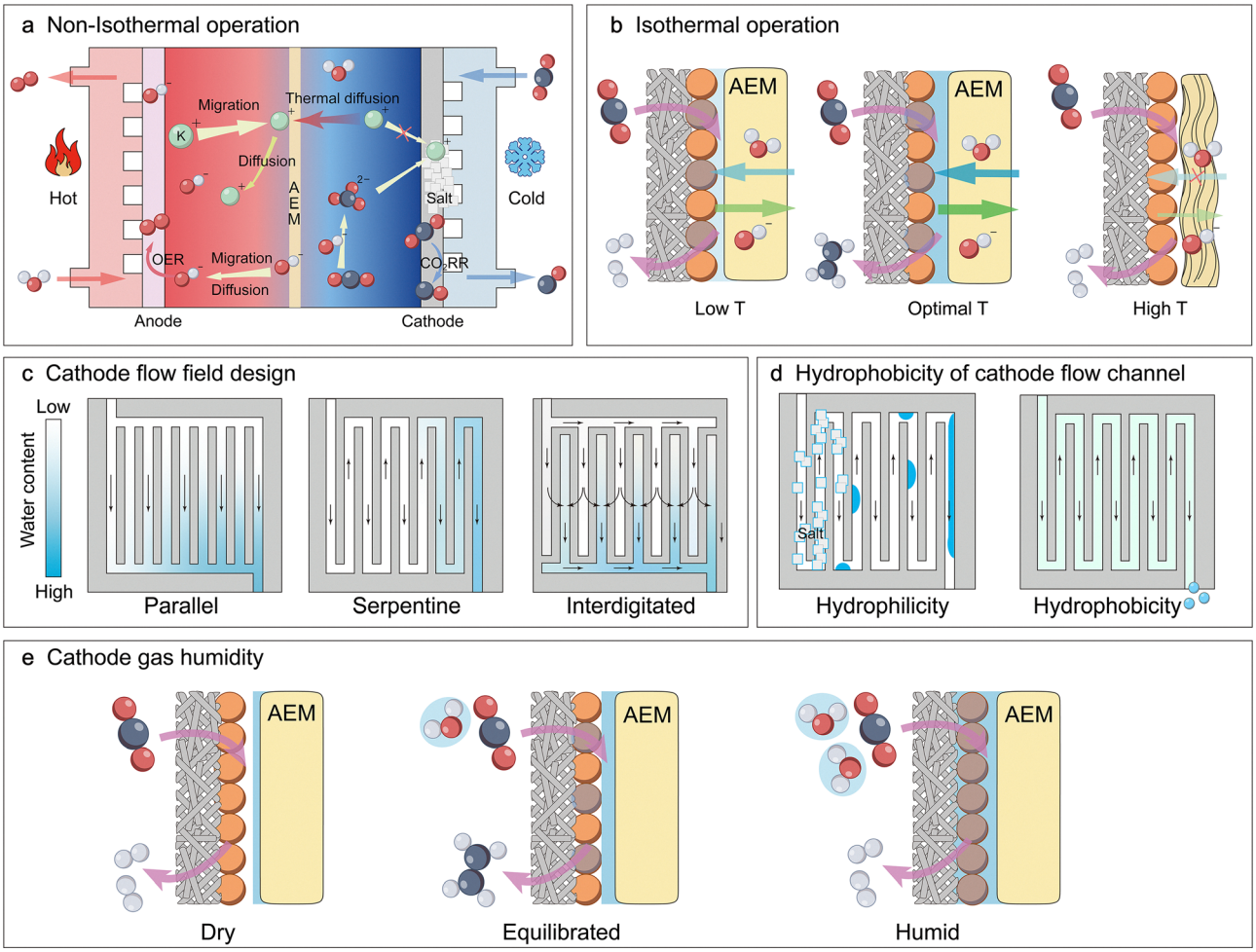

Fig. 16 Device architecture design and operating condition optimisation. (a) Schematic of the reaction and ion transport mechanism for the non-isothermal operation during the CO_2RR. (b) Effect of isothermal operation on anion exchange membrane (AEM) structure and water transport during the CO_2RR. Blue arrows represent water transport, green arrows indicate charge carrier transport, with the thickness of arrows reflecting the transport rate. (c) Schematic illustrating the influence of cathode flow field design on water distribution and content within flow channels during the CO_2RR. (d) Schematic comparison of water and salt distribution within flow channels with and without hydrophobic modification during the CO_2RR. (e) Schematic illustrating the effect of cathode gas feed humidification on water distribution across the AEM and GDE. The orange, grey, red, and white spheres represent metal particles, carbon, oxygen, and hydrogen atoms, respectively. AEM stands for the anion exchange membrane.

flow field boosted the CO FE by 43.5% compared to a standard parallel channel design at an identical total current density of 350 mA cm^{-2}. Even with optimised flow field structures, effective management of saline droplets on the cathode side remains vital to prevent salt-induced GDE blockage (Fig. 16d). Hao *et al.* have revealed that once cation-containing droplets form at the cathode reaction interface, they are propelled by the gas stream to the rear of the GDE, where they dry out and precipitate within the gas channels.[119] Usually, during long-term operation, salts mainly accumulate in the first few serpentine channels at the inlet of the flow field, primarily because the relative water content in the gas flow at the inlet position is lower while the CO_2 concentration is higher.[151,154] By coating interior walls of the stainless-steel gas channels with a hydrophobic Parylene layer, the adhesion force of droplets can be reduced, allowing them to be carried out by the gas flow before drying. This significantly extended the stable operation time for the CO_2RR to form CO at 200 mA cm^{-2} from approximately 100 hours to over 500 hours.

The relative humidity (RH) of the cathode feed gas is the most direct tool for regulating the water balance within an MEA (Fig. 16e). The work of Gawel *et al.* on the CO_2RR to form CO clearly demonstrates the critical trade-off involved.[13] Excessively low RH (*e.g.*, 37%) leads to membrane dehydration, which reduces the conductivity of the AEM and limits the reaction rate. Conversely, excessively high RH (*e.g.*, 100%) results in flooding, as the water input overwhelms the ability to remove it, thereby impeding CO_2 mass transport. Optimal performance is therefore achieved only within a well-defined, moderate humidity window (*e.g.*, 79% RH), where the supply and removal of water reach an ideal balance. It must be emphasised that these regulatory strategies are not universally applicable to all reaction systems, and water regulation is often accompanied by indirect regulation of other processes, such as the concentration and adsorption strength of CO_2 and reaction intermediates.

Collectively, these results clearly reveal that both salt accumulation in the CO_2RR and water flooding for the GDE are key causes of performance decline in electrolysis, fundamentally arising from improper water management.

3.6. Optimizing water management for large-scale CO_2/CO electrolysis

In the scaling process of CO_2/CO electrolysers, water management has emerged as a critically important yet frequently overlooked bottleneck, particularly due to its indirect role as an efficient medium for heat storage and exchange.[155] Given the low energy efficiency of CO_2 electrolysis, more than 50% of the electrical input is converted into Ohmic heat. In large-area electrolysers, the continuous accumulation of this heat, if not promptly removed, leads to a sharp rise in reaction zone temperature, severely impacting the performance and stability of the electrolyser. Consequently, the importance of water management at this scale has now garnered widespread attention. Hurkmans *et al.* systematically revealed that the temperature gradient along the flow channel is a key factor determining its scalability.[156] This finding was achieved through the development of a two-dimensional (2D) non-isothermal model (Fig. 17a and b). In this model, the *y*-direction represents the flow direction, while the *x*-direction is perpendicular to the flow, corresponding to the cross-sectional width of the electrolyser spanning from the anode to the cathode. The results showed a stark contrast. The exchange MEA, benefiting from the efficient heat removal capacity of its liquid anolyte, exhibited a temperature increase of less than 10 °C along a 20 cm flow path even at an industrial-grade current density of 750 mA cm^{-2} (Fig. 17c). In contrast, the full MEA, due to the poor thermal conductivity of its all-gas-phase architecture, experienced a sharp temperature rise from 20 °C to 55 °C at just 210 mA cm^{-2} (Fig. 17d). This high temperature triggered severe membrane dehydration, leading to a sharp increase in Ohmic losses and a rapid decline in current density, indicating that this configuration is unsuitable for scale-up. Additionally, non-isothermal effects were particularly pronounced in the *x*-direction (perpendicular to the electrode), with temperature peaks concentrated in the cathode catalyst layer, attributed to the higher overpotential of the CO_2RR compared to the OER. Therefore, the study conclusively identified that the exchange MEA configuration, with its superior thermal and water management capabilities, is the ideal choice for the industrial scale-up of CO_2 electrolysis. Although many single MEAs have demonstrated excellent performance in the CO_2RR and the CORR, the stacking and scaling-up process may lead to performance variations due to thermal effects. Quentmeier *et al.* constructed a three-cell short stack, consisting of a terminal anode cell (TA), a middle cell (MC), and a terminal cathode cell (TC) connected in series, and systematically investigated the impact of temperature gradients on the performance for the CO_2 reduction to CO (Fig. 17e–i).[116] The study found that at high current densities (300–400 mA cm^{-2}), the total voltage of the short stack was lower than the sum of the voltages of three independent single cells (Fig. 17i). The authors attributed this phenomenon to the heat accumulation effect during stack operation: compared to a single cell, the heat-generating active area of the short stack increased threefold, while the external heat dissipation area remained nearly unchanged, resulting in a significant rise in internal operating temperature (Fig. 17e and g). For instance, at 400 mA cm^{-2}, the electrolyte temperature of the stack reached 43 °C, whereas that of the single cell was only 38 °C. This resulted in a lower operating voltage but also a decrease in the CO FE (Fig. 17i). This result was consistent with a control experiment, which observed similar trends of a drop in both voltage and CO FE when a single cell was heated from 38 °C to 43 °C under the same conditions. The study revealed that cell performance is closely related to its position within the stack: the voltage of the TC remained the lowest under all operating conditions (Fig. 17i). This was attributed to the uneven temperature distribution within the stack caused by the asymmetrical cell structure. TA and MC benefited from effective cooling due to anode liquid flowing on both sides (Fig. 17g). In contrast, TC was cooled only on one side, with the other side exposed to poorly conductive CO_2 gas,

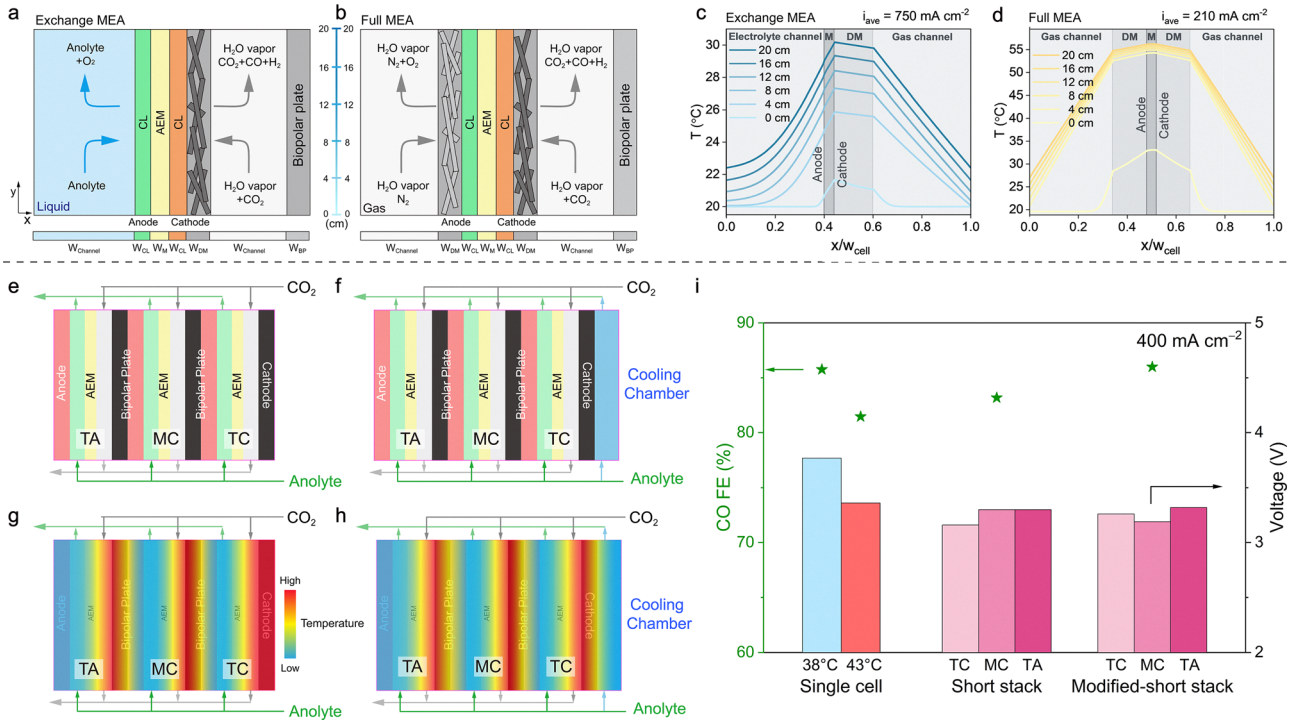

Fig. 17 Influence of water on heat management and reaction performance during CO_2 electrolysis upscaling in MEAs. (a) Exchange MEA configuration is fed with liquid electrolyte at the anode side. The cathode compartment is fed with humidified CO_2. (b) Full MEA configuration is fed with a gaseous feed at both the anode and the cathode. (c) Temperature profiles taken at intervals of 4 cm along the flow direction of the simulated exchange MEA electrolyser operating at 750 mA cm^{-2}. (d) Temperature profiles taken at intervals of 4 cm along the flow direction of the simulated full MEA electrolyser operating at 210 mA cm^{-2}. Reproduced with permission from ref. 156. Copyright 2025, Royal Society of Chemistry. (e) Illustration of the three-cell short stack. (f) Modified short stack with a half-plate of the bipolar plate on the adjacent side of the TC. (g) Possible heat distribution in the short stack with neglected cooling by gas. (h) Possible heat distribution in the modified short stack with neglected cooling by gas. (i) The cell voltage and the CO FE at 400 mA cm^{-2} for the CO_2RR for the single cell, short stack, and modified short stack. Reproduced with permission from ref. 116. Copyright 2024, American Chemical Society. TA, MC, TC, CL, and AEM stand for the terminal anode cell, middle cell, terminal cathode cell, catalyst layer, and anion exchange membrane, respectively.

resulting in the poorest heat dissipation, the highest local temperature, and the lowest voltage. Furthermore, by adding an additional cooling plate to the exterior of the TC, its heat dissipation conditions were symmetrized with those of the other cells (Fig. 17f and h). Experimental results demonstrated that in the modified short stack, the voltages of the individual cells became more uniform and the CO FE was also significantly improved (Fig. 17i). As the electrode area and total current further increase, the challenges of water management become more pronounced in kilowatt-scale electrolysis systems, particularly in addressing the temperature rise induced by Ohmic heating. Research by Crandall *et al.* demonstrated that expanding the MEA electrode area from 5 cm^2 to 100 cm^2 at a current density of 200 mA cm^{-2} causes the steady-state operating temperature to increase by 45% due to resistive heating.[120] To address this, when constructing a kilowatt-scale stack (100 cm^2 per layer, 10-layer), each layer was actively integrated with water cooling channels to effectively remove heat. Concurrently, to mitigate water flooding, the hydrophobicity of the cathode GDE was significantly enhanced by adding a coating of fluorinated ethylene propylene (FEP) mixed with carbon black. Ultimately, the 500 cm^2 CO_2 electrolyser stack operated at a total current of 100 A (200 mA cm^{-2}) with CO FE exceeding 80%. Meanwhile, the 1,000 cm^2 CO electrolyser stack operated at 300 A (300 mA cm^{-2}), achieving a cell voltage of 2.26 V and a full cell energy efficiency of 39% toward C_{2+} products. These findings highlight that, at the macro-scale, effectively managing the dual role of water in absorbing and transporting heat while shaping the multiphase reaction environment is essential for achieving stable, large-scale CO_2 electrolysis.

These findings reinforce the critical importance of implementing multi-scale synergistic water regulation during the CO_2RR and the CORR. As CO_2/CO electrolysis moves from laboratory to larger-scale systems, effective water management at various scales becomes increasingly vital to sustaining high performance and minimizing degradation during scale-up.

4. Advanced *in situ* characterization techniques related to water

Currently, *in situ* characterisation techniques for water in the electrocatalytic CO_2RR/CORR have evolved to span scales ranging from the molecular to the mesoscopic and macroscopic (Fig. 18 details these techniques, including a schematic

	Techniques	Characterization results related to water	Schematic diagram	Resolution
Micro-scale	*In-situ* ATR-IRAS (SEIRAS)	(1) Interfacial water orientation and hydrogen bond network structures (2) Reaction intermediates interacting with water	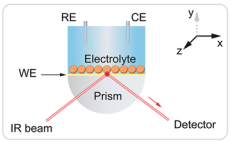	Probing depth: 100 nm ~1 μm Resolution (x,z): 20 ~500 μm Time resolution: 10 ms ~1 s
	In-situ Raman (SERS)	(1) Interfacial water orientation and hydrogen bond network structures (2) Reaction intermediates interacting with water (3) Local pH values	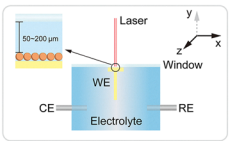	Probing depth: 0.5 ~2 μm Resolution (x,z): 20 ~500 μm Time resolution: 0.1 ~1 s
	In-situ APXPS	Chemical states and coverage density of surface water/ hydroxyl groups	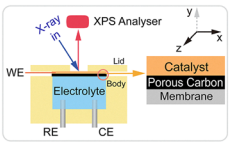	Probing depth: <10 nm Resolution (x,z): >100 μm
Meso-scale	*Operando* WAXS / XRF	(1) Water content distribution in MEA various layers (2) Alkali metal ion distribution in MEA various layers	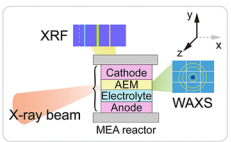	Resolution (y,z): 5 × 20 μm Time resolution: >0.8 s
	Operando NI	(1) Distribution of salt precipitate (2) Water transport, distribution and relative humidity within MEA	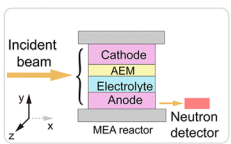	Resolution (y,z): ~6 μm Time resolution: >10 s
	Operando OCT	(1) 3D microstructure imaging of MEA (2) 3D imaging of water/droplet distribution (3) Direct imaging of gas bubble dynamics	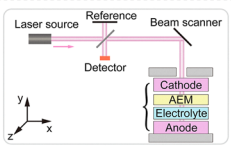	Resolution (x,y,z): 1 μm Time resolution: >1 μs
	Operando Synchrotron CT	(1) 3D microstructure imaging of MEA (2) 3D imaging of water/droplet distribution	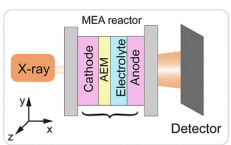	Resolution (x,y,z): 1 μm Time resolution: >40 ms
	In-situ FLIM	2D imaging of local pH gradients	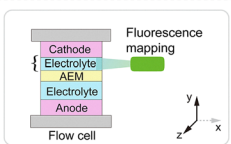	Probing depth: 2 mm Resolution (y,z): 5 μm Time resolution: >0.45 s
Macro-scale	*Operando* EIS (Multi-sine / DRT)	(1) Ohmic resistance (membrane/electrolyte hydration) (2) Mass transport impedance (GDE water management) (3) Warburg impedance (salt precipitation)	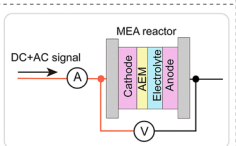	Overall Time resolution: >5 s
	Operando electrolyte leakage quantification	(1) Real-time electrolyte leakage rate from GDE (2) Direct correlation of leakage and product selectivity	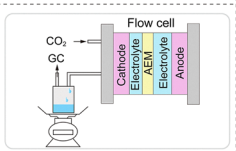	Overall Time resolution: 1 min Measurement uncertainty: ± 0.6 mg min^{-1}

Fig. 18 Summary of currently used advanced multi-scale *in situ* characterization technologies related to water. The orange spheres represent metal particles. ATR-IRAS, SEIRAS, SERS, APXPS, WAXS, XRF, NI, OCT, CT, FLIM, EIS, DRT, RE, CE, WE, IR, DC, AC, GDE stand for attenuated total reflection infrared absorption spectroscopy, surface-enhanced infrared absorption spectroscopy, surface-enhanced Raman spectroscopy, ambient pressure X-ray photoelectron spectroscopy, wide-angle X-ray scattering, X-ray fluorescence, neutron imaging, optical coherence tomography, computed tomography, fluorescence lifetime imaging microscopy, electrochemical impedance spectroscopy, distribution of relaxation times, reference electrode, counter electrode, working electrode, infrared, direct current, alternating current and gas diffusion electrode, respectively.

diagram, the time and spatial resolution, and typical characterization results for each).

At the molecular scale, research efforts are primarily focused on the precise probing of interfacial water behaviour. As a non-centrosymmetric molecule, the vibrational modes of water can be probed by both infrared and Raman spectroscopy. Furthermore, the metal electrodes commonly employed for the CO_2RR, such as Au, Ag, and Cu, possess plasmonic properties that can effectively enhance spectroscopic signals, thereby providing favourable conditions.[157] Although infrared spectroscopy is highly sensitive to absorption by bulk water, the attenuated total reflection infrared absorption spectroscopy (ATR-IRAS) and surface-enhanced infrared absorption spectroscopy (SEIRAS) configuration confines the probing depth to the electrode–electrolyte interfacial region [probing depth: 100 nm–1 μm; spatial (x, z): 20–500 μm; temporal: 10 ms–1 s], thereby mitigating interference from the bulk aqueous phase.[158] This technique enables the dynamic monitoring of changes in the intensity, frequency, and lineshape of the characteristic vibrational bands of interfacial water.[36] In conjunction with the analysis of relevant reaction intermediates, these observations provide deep insights into the dynamic evolution of water molecules near the catalyst surface and elucidate their pivotal role in electrocatalytic processes. Raman spectroscopy and surface-enhanced Raman spectroscopy (SERS), whilst sensitive to the inherently weak Raman scattering of water, are highly adaptable to aqueous systems and offer a versatile probing depth [probing depth: 0.5–2 μm; spatial (x, z): 20–500 μm; temporal: 0.1–1 s], yielding insights that are both similar and complementary to those from infrared spectroscopy.[159] For instance, the *in situ* monitoring of the interfacial carbonate-to-bicarbonate ratio allows for the effective inference of local pH, facilitating the tracking and analysis of interfacial water behaviour and the local microenvironment. A SERS investigation by Zhao *et al.* on different copper single-crystal facets (including Cu(100), Cu(110), and Cu(111)) for the CO_2RR revealed that the crystal surface significantly regulates the proportions of interfacial water types.[160] Their findings show a clear positive correlation between the concentration of K^+-hydrated water (K-H_2O) at the interface and the selectivity for C_{2+} products. The proposed mechanism suggests that in the absence of K^+, interfacial water tends to form hydrogen bonds with *CO intermediates, which promotes further hydrogenation to form C_1 products like methane. However, the presence of K^+ reshapes the surrounding water into K-H_2O configurations that are unfavourable for hydrogen bonding with *CO. This creates a local hydrogen-bond-absent environment that suppresses the hydrogenation pathway and kinetically favours C–C coupling, thereby significantly enhancing the selectivity for C_2 products. Additionally, *in situ* near-ambient pressure X-ray photoelectron spectroscopy (NAP-XPS) leverages its surface sensitivity [probing depth: $<$ 10 nm; spatial (x, z): $>$ 100 μm] and its ability to operate under near-ambient pressure conditions.[161] By analysing core-level spectra like O1s, it directly probes the chemical states of water and its derivatives (*e.g.*, OH^-) at the electrode interface. This allows for the quantification of water adsorption, dissociation, and its interaction with the catalyst surface under reaction conditions.

At the meso-scale, characterisation focuses on the visualisation and quantification of water distribution, transport, and associated structural evolution. Wide-angle X-ray scattering (WAXS) reveals structural changes in water clusters and ionomeric polymers within the MEA, as well as water- or ion-induced phase transitions. By analysing the scattering background, it can quantitatively determine the relative water content. As a powerful complement to WAXS, X-ray fluorescence (XRF) microscopy can reveal the distribution and concentration gradients of alkali metal cations in the various layers of the MEA, thereby indirectly reflecting the hydration environment and regions of ion enrichment or depletion. The spatial resolution for both techniques is determined by the beamline optics and specifications of the synchrotron source, with resolutions on the micrometer-scale being achievable [spatial (y, z): 5 μm × 20 μm; temporal: $>$ 0.8 s]. Notably, Joensen *et al.* employed correlative WAXS and XRF to simultaneously monitor water content and cation (*e.g.*, Cs^+) concentration within various MEA layers during the CO_2RR.[162] Their work conclusively demonstrated that cations transport water molecules across the AEM towards the cathode *via* electro-osmotic drag and revealed how subsequent water diffusion promotes Cs^+ penetration into the GDE, causing local flooding. Further investigation showed that the applied voltage difference is the primary driving force for Cs^+ migration, whereas upon lowering or removing the voltage, mass transport dominated by the concentration gradient promotes the rapid back-diffusion of Cs^+ from the cathode to the anode. The direct imaging of water provides more explicit visualisation of the internal environment of the electrolyser. Neutron imaging, owing to its high sensitivity to hydrogen atoms, has emerged as an ideal, non-destructive, high-resolution approach for visualising water distribution. By passing a neutron beam through the electrolyser, the significant attenuation of the signal by hydrogen creates high-contrast images that directly map the two-dimensional spatial distribution of water [spatial (y, z): *ca.* 6 μm; temporal: $>$ 10 s]. This allows for the observation of water distribution within the MEA/GDE, transport pathways (including flooded regions), membrane water content, and water transport dynamics. For example, research by Disch *et al.* using high-resolution neutron imaging revealed the non-uniform distribution of water upon electrolyser start-up, with preferential accumulation in the corners of the cathode flow channels and a greater accumulation of water-retaining precipitates in the channel area compared to the land area.[163] At low current densities, the cathode GDE is wetter than when no current is applied; however, with increasing current density, water consumption at the cathode intensifies, resulting in pronounced drying of both the cathode and the membrane, especially along flow channel regions of the cathode GDE. These findings indicate that the CO_2 gas stream typically carries away more water than it brings in and that the hygroscopic nature of precipitated salts also significantly affects water distribution on the cathode side. Electrochemical optical coherence tomography (eOCT), based on the

backscattering of near-infrared light, reconstructs the three-dimensional microstructure of the sample [spatial (x, y, z): 1 μm; temporal: >1 μs]. The technique allows for real-time observation of water distribution and dynamic changes within the MEA, including thickness variations and the evolution of flooded or dry regions, and liquid droplet migration processes. Lu *et al.* were the first to apply eOCT to observe in real time and with micrometre-scale resolution the formation of a dynamically changing gap filled with liquid electrolyte (water) between the cathode and the membrane, influenced by a combination of gas evolution and electric field effects.[164] This platform enables the identification and mapping of the TPB and demonstrates that CO generation is strongly correlated with regions of high TPB density. Likewise, synchrotron-based X-ray computed tomography (CT) has been successfully employed to investigate the three-dimensional spatial distribution of water within the MEA during the CO_2RR to form CO [spatial (x, y, z): 1 μm; temporal: >40 ms]. Ko *et al.* used this technique to visualise the progressive onset of flooding within the catalyst and GDL as the applied potential increased.[165] They further demonstrated that modifying silver nanoparticles with hydrophobic lipid ligands could effectively repel the electrolyte to prevent flooding at high voltages, enabling stable operation at a current density of 150 mA cm^{-2} for up to 100 hours. Finally, for probing the local chemical environment, fluorescence lifetime imaging microscopy (FLIM) offers a powerful approach [probing depth: 2 mm; spatial (y, z): 5 μm; temporal: >0.45 s]. By introducing pH-sensitive fluorescent dyes into the electrolyte and utilising changes in dye molecule fluorescence lifetime caused by pH variation, FLIM enables precise measurement of local pH values at specific locations, thereby revealing micrometre-scale local pH concentration gradients. Baumgartner *et al.* mapped the two-dimensional pH distribution within the cathode liquid chamber during the CO_2RR in a flow cell, directly observing the dynamic evolution of the aqueous local pH.[166] This work confirmed the formation of an alkaline boundary layer at the electrode–electrolyte interface, where OH^- production led to a local pH substantially higher than that of the bulk solution. Moreover, it was found that the local pH is highly dynamic and significantly influenced by bubble dynamics. At high current densities, vigorous bubble formation and the consequent mixing effectively promote the blending of high-pH interfacial regions with the lower-pH bulk solution, thereby suppressing an excessive rise in interfacial pH.

Finally, at the macroscopic scale, diagnostic approaches focus on evaluating the impact of water management on overall electrolyser performance. Electrochemical impedance spectroscopy (EIS), as a non-destructive, real-time, *in situ* diagnostic technique, sensitively probes charge transfer and mass transport processes within the electrolyser by applying small perturbation alternating current signals. By fitting impedance data to an equivalent electrical circuit (EEC) model, the specific impact of water can be translated into clear fault-diagnostic fingerprints. For example, Warkentin *et al.* systematically demonstrated the application of multi-frequency sinusoidal EIS in diagnosing water flooding-related failures of the cathode GDE within the MEA.[167] Their research revealed that excess water accumulation in the vicinity of the catalyst membrane interface leads to a decline in interfacial ionic conductivity, manifesting as an increase in Ohmic resistance (R_0). In contrast, the blockage of pores in the GDE due to flooding is primarily reflected by a significant increase in the faradaic resistance (R_1). Furthermore, they found that salt precipitation within the GDE is readily identified by a sharp increase in the Warburg diffusion impedance (W_1). To further elucidate the complex effects of water management, Qu *et al.* conducted long-term tests for the CO_2RR to form CO in a pure water system, introducing distribution of relaxation times (DRT) analysis to deconvolve the EIS data.[168] DRT analysis enables the effective deconvolution of mass transport processes highly correlated with water management. The results showed that during performance degradation over more than 40 hours of stability testing, the intensity of the P_1 peak, representing CO_2 mass transport, sharply increased in the DRT spectrum. Combined with the post-electrode test observation of a transition in water contact angle from hydrophobic to hydrophilic, the study further revealed that the fundamental cause of performance degradation was a loss of water control capability due to physical changes in the cathode catalyst layer structure, resulting in severe flooding and substantial obstruction of CO_2 transport. This series of works tightly link macroscopic performance, EIS/DRT signals, and the interplay between microstructural features and water, offering profound insights for the understanding and optimisation of water management strategies. To monitor GDE flooding in real-time during CO_2 electrolysis in a flow cell, Rottmann *et al.* developed an *operando* electrolyte leakage quantification method.[169] This technique uses a water trap on a precision balance to collect and quantify electrolyte leakage from the GDE, enabling the determination of real-time leakage rates (temporal: 1 min; measurement uncertainty: ±0.6 mg min^{-1}). Simultaneously, gaseous products are directed to a gas chromatograph (GC) for concurrent analysis. The study revealed that GDE flooding depends strongly on operating conditions. At higher current densities (200 and 300 mA cm^{-2}), the leakage rate increased significantly over time, whereas it remained low and stable at 100 mA cm^{-2}. A strong correlation was observed between the increasing leakage rate and the rising FE for H_2, indicating that flooding impedes CO_2 mass transport. However, external leakage rates alone cannot fully describe electrode flooding. After operating at high current density and returning to a lower one, the H_2 FE was higher than that in the initial phase, even when the leakage rates were comparable. This indicates the presence of internal flooding, whereby isolated regions within the GDE become flooded without forming a continuous path for external leakage. The study also proposed a recovery strategy. Intermittent rest periods at open-circuit voltage (OCV) effectively reduced flooding, lowering leakage rates and H_2 FE upon resuming electrolysis. This recovery is attributed to the diffusion of detrimental species, such as carbonate salts, from electrode pores, restoring GDE hydrophobicity and catalyst active sites.

5. Multi-scale theoretical modelling strategies related to water

While *in situ* characterization offers valuable insights, capturing the discrete dynamics of water behaviors remains difficult, as experimental signals inherently reflect statistical averages. As a vital complement, multi-scale simulation enables the resolution of specific water behaviors under evolving spatiotemporal conditions. The multi-scale simulation capability allows researchers to dissect the roles of water across different dimensions (Fig. 19 details these techniques, covering their schematic illustrations, spatiotemporal resolutions, representation of water, and key research objectives). As discussed above, significant progress has been made in unraveling the complex coupled mechanisms of the water–cation–electric field nexus, providing a theoretical foundation for achieving efficient CO_2RR and CORR.

Density functional theory (DFT) serves as a primary static computational tool at the atomic scale (typically $<$ 100 atoms; *ca.* 1 nm). In this framework, water acts as both a proton source and a potential oxygen source.[170] Calculations are typically performed at 0 K to determine the energy barriers (activation energy) of elementary reactions, reaction heats (thermodynamic potentials), and intermediate adsorption configurations. Water is usually represented using an explicit or implicit model: the explicit component introduces a limited number of water molecules *via* micro-solvation models to directly participate in intermediate stabilization through hydrogen bond networks (often using slab models), while the implicit component acts as a continuous background to simulate the dielectric screening effect of bulk water. Recent studies have profoundly revealed the critical role of such local solvation effects. For instance, Chen *et al.* utilized grand canonical ensemble DFT (GCE-DFT) combined with explicit water models to investigate the C–C coupling mechanism on copper surfaces.[171] Their results indicate that under vacuum conditions, the key intermediate OCCO tends to form a thermodynamically unstable L-shape configuration (single C atom adsorption). However, upon introducing explicit water molecules, the specific hydrogen bond network formed with the oxygen atoms of OCCO induces electron transfer to the intermediate, forcibly locking the configuration into a more stable U-shape (dual C atom adsorption). Computational results show that this water-mediated configurational inversion significantly

Technique	Scale (Time, Space)	Model illustration	Representation of water	Key research objective
DFT	Static Å - nm scale	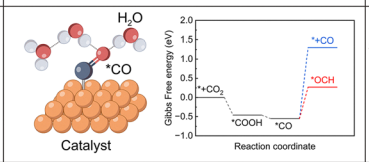	**Proton source or potential oxygen source,** implemented by: ➢ **Explicitly modeling:** Water molecules (microsolvation). ➢ **Implicitly simulating:** The bulk dielectric background.	• Calculating elementary reaction barriers and thermodynamic potentials, specifically: ➢ Resolving local stabilization of intermediates via specific H-bond networks. ➢ Incorporating bulk dielectric screening corrections to reaction energetics.
AIMD	Dynamic (ps) Å - nm scale	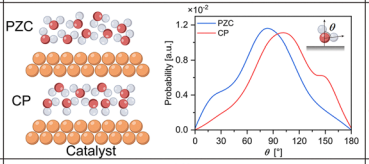	**Chemically active solvent:** Forming dynamic H-bond networks and allowing explicit O-H bond dissociation and proton shuttling under thermal motion.	• Observing real-time proton transfer mechanisms. • Studying potential-dependent interfacial water, structure, orientation, and H-bond dynamics. • Analyzing dynamic solvent effects on intermediate kinetics.
ML-MD	Dynamic (ns) nm	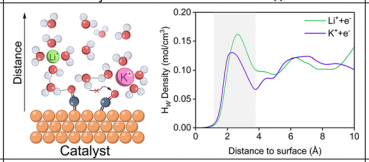	**Large-scale explicit solvent:** Capturing statistical dynamics of hydrogen-bond networks and EDL restructuring over long timescales.	• Simulating complex EDL structures and properties. • Investigating long-term water diffusion and transport phenomena.
kMC	Statistical (μs-s) nm-μm	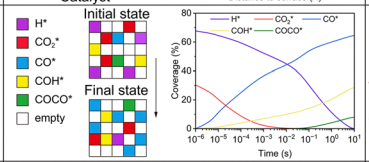	**Competitive surface species & reactants:** Accounts for surface coverage, competitive adsorption and surface diffusion of water species.	• Statistically analyzing the impact of interfacial electric fields on reactions. • Evaluating surface coverage of water-related species across different active sites. • Analyzing TOF and product selectivity influenced by water participation.
CFD	Continuum (s-h) > μm	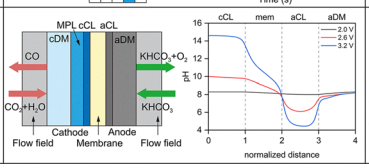	**Multi-functional continuum fluid:** Serving as solvent, reactant/product carrier, and medium for heat transfer and storage.	• Modeling temperature distribution driven by reaction/Joule heat. • Predicting concentration gradients of reactants/products and local pH shifts in the aqueous phase. • Studying electrolyte penetration and wettability in porous electrodes.

Fig. 19 Summary of currently used advanced multi-scale simulation technologies related to water. The orange, grey, red, and white spheres represent metal particles, carbon, oxygen, and hydrogen atoms, respectively. Reproduced with permission from ref. 170. Copyright 2022, Royal Society of Chemistry; ref. 174. Copyright 2025, Springer Nature; ref. 33. Copyright 2024, American Chemical Society; ref. 178. Copyright 2025, American Chemical Society; ref. 63. Copyright 2024, John Wiley & Sons, Inc. The abbreviations stand for density functional theory (DFT), *ab initio* molecular dynamics (AIMD), machine learning molecular dynamics (ML-MD), kinetic Monte Carlo (kMC), computational fluid dynamics (CFD), electrical double layer (EDL), turnover frequency (TOF), potential of zero charge (PZC), and cathodic potential (CP).

lowers the activation barrier for C–C coupling. This demonstrates that static DFT calculations ignoring the hydrogen-bond donor role of explicit water lead to erroneous predictions of reaction pathways.

To transcend the limitations of static calculations, *ab initio* molecular dynamics (AIMD) introduces thermal motion and temporal evolution on the picosecond scale. By constructing dynamic interfaces filled with explicit water molecules under periodic boundary conditions (typically $<$ 1000 atoms; spatial domain *ca.* 1 nm), AIMD treats water as a chemically active solvent connected by hydrogen bond networks and capable of O–H bond cleavage and recombination. This explicit representation enables the real-time capture of the Grotthuss proton transport mechanism and the dynamic structural evolution of solvent layers in real time.[172–174] Qin *et al.* discovered in their study of the Au–water interface that interfacial water does not exist independently but assembles with K^+ to form dynamic cation–water solvation shells.[175] Simulation results showed that this composite shell interacts directly with adsorbed CO_2 *via* an inner-sphere coordination mechanism, reducing the free energy barrier for CO_2 activation by 0.66 eV. Through electrostatic interactions and the hydrogen bond network, it stabilizes the transition states and intermediates of CO_2 activation, significantly enhancing the reaction rate. A more critical finding lies in the suppression mechanism of the HER, where slow-growth sampling (SG-AIMD) simulations revealed that the structural rigidity and restricted molecular rotation of the first interfacial water layer significantly impede water dissociation in the Volmer step. Consequently, this kinetic limitation raises the energy barrier of the rate-determining step from a facile 0.58 eV (observed when cations are in the bulk) to a prohibitive 1.27 eV. This result confirms, at the atomic kinetic level, that the interfacial water layer not only promotes the CO_2RR but also effectively blocks the parasitic consumption of protons.

Machine learning molecular dynamics (ML-MD) has successfully extended the simulation scale to the meso-micro bridging region (*ca.* 10–100 nm, ns scale) by training high-accuracy potential functions, thereby enabling the handling of statistical ensembles of the EDL containing millions of water molecules.[176] This approach quantifies the structural response of the EDL under realistic operating potentials and its statistical impact on reaction kinetics. Tian *et al.* investigated the solvent dynamics of the Ag(111)/water interface under constant potential conditions.[174] At a working potential of -1.5 V relative to the potential of zero charge (PZC), interfacial water molecules undergo significant rearrangement, predominantly adopting an H-down configuration (hydrogen atoms pointing towards the electrode). This leads to a shortened average lifetime of the interfacial hydrogen bond network and a reduction in the number of hydrogen bond donors. This loose dynamic solvent environment helps stabilize key intermediates (such as *COOH) and, more importantly, reduces the free energy barriers for hydroxide diffusion and proton transfer by approximately 0.2–0.3 eV. This finding proves that the solvent is not merely a background; the collective dynamic effects arising from thousands of water molecules in response to electrode potential changes can directly modulate intermediate stability and reaction rates.

Kinetic Monte Carlo (kMC) simulations bridge the vast gap between quantum chemical calculations and macroscopic experiments by tracking surface events on mesoscopic spatial scales (*ca.* μm) and macroscopic time scales (seconds to hours).[177,178] Unlike static DFT, kMC constructs discrete lattice networks based on the adsorption site topology determined by DFT. It utilizes transition state theory to convert microscopic energy barriers into stochastic hopping rates for elementary steps (*e.g.*, adsorption, diffusion, reaction), while introducing coverage-dependent lateral interactions to dynamically describe reaction kinetics under high coverage. By counting the cumulative number of specific product formation events over the simulation time, this method allows for the direct quantitative calculation of turnover frequency (TOF) and product selectivity. In kMC simulations, water and its dissociated species (*H and *OH) not only participate as key reactants in intermediate hydrogenation and product formation but also exert statistical occupancy and steric hindrance effects on active sites at high coverage. Li *et al.* profoundly revealed the roadblock effect imposed by solvent species. Specifically, they demonstrated that in high-coverage surface environments, water-related species (*H and *OH) physically partition the active region, forcing key intermediates (such as *CO) to diffuse through tortuous paths.[177] This crowded environment constructed by the solvent significantly alters the local residence time and collision probability of intermediates, resulting in kinetically restricted surface diffusion of *CO. This mechanism successfully explains the previous experimentally observed isotope fractionation phenomenon, where the produced ethylene and ethanol possess distinct isotopic compositions, statistically proving that restricted surface diffusion is a governing factor for C_{2+} product selectivity.

Multiphysics simulation, *i.e.*, computational fluid dynamics (CFD) coupled with mass transport,[179,180] treats water as a multifunctional continuous medium that transports solvents, reactants, and heat. By coupling the Navier–Stokes equations, Nernst–Planck equations, and electrochemical kinetic equations, this method resolves complex physical field distributions at macroscopic time resolutions ($>$1 s) that are difficult to measure experimentally.[181,182] Initially, this approach was primarily applied at the reactor scale to predict reactant/product concentration gradients, local pH shifts, and temperature distributions driven by reaction or Joule heating. The studies by Reyes *et al.* and Hurkmans *et al.* successfully utilized this method to analyze water-thermal management in MEAs, as detailed in the previous section.[145,156] Recently, it has been extended to the micro-scale to address HER challenges in acidic systems. Qin *et al.* utilized a multi-physics model to simulate mass transport processes within a surface-modified cross-linked polyelectrolyte (cl-PDDA) layer.[180] In this model, water is treated as a continuous background, focusing on the diffusion and migration behavior of hydronium ions (H_3O^+) within the polymer network. Simulation results quantitatively revealed the remodeling role of the Donnan effect on the interfacial

water environment: the high density of fixed positive charges on the polymer backbone exerts strong electrostatic repulsion on H_3O^+ in the solution, significantly suppressing proton diffusion within the polymer layer. Quantitative conclusions indicate that this electrostatic sieving effect reduces the local H^+ concentration at the catalyst surface by approximately three orders of magnitude compared to the bulk phase (pH = 1.0), successfully constructing a localized proton-deficient/neutral water environment within a macroscopic acidic electrolyte. This study demonstrates that continuum simulation can precisely decouple water environments at different locations, effectively separating the microscopic water environment at the catalyst surface from the macroscopic bulk water environment through artificially engineered interface layers.

6. Challenges and outlook

This review has summarised the multi-scale roles of water in the CO_2RR/CORR and its corresponding regulation strategies. Although these strategies have demonstrated immense potential for enhancing reaction performance, the translation from laboratory-scale research to industrial application still faces formidable challenges. Future research should achieve breakthroughs in the following key directions:

6.1 Deepening atomic/molecular-scale understanding to guide rational catalyst and interface design

A profound understanding of the multifaceted roles of water in electrocatalysis remains a challenge. For instance, key scientific questions at the atomic-scale are still not fully understood, such as the differential water activation requirements for the CO_2RR *versus* the HER, and the extent and sites of water activation needed for the formation of different products. Future studies should clarify the molecular dissociation mechanisms of water at the atomic level, clearly differentiating the specific requirements for the CO_2RR from those for the HER, rather than indiscriminately designing catalysts to promote or hinder water activation. Additionally, it is crucial to elucidate both the degree and site specificity of water activation needed for different product pathways, and based on such insights, to establish unified descriptors and new frameworks for catalyst design.

6.2 Bridging the gap in cross-scale understanding

One of the core challenges in current research lies in effectively correlating and unifying the understanding of regulatory effects across different scales. Existing *in situ* characterisation techniques at the atomic, mesoscopic, and macroscopic levels often rely on *in situ* cells with structures that are quite distinct from those operating under real reaction conditions. This disparity between the characterisation environment and the real reaction environment makes it difficult to directly match and cross-validate obtained data, leading to a fragmented understanding of the crucial chain linking "macroscopic operating parameters–meso-scale transport–atomic-scale interfacial reactions." To this end, the key moving forward lies in integrating advanced, multi-scale *in situ* characterisation techniques. Efforts should be focused on developing *in situ* platforms and methods that can operate for extended periods under conditions more closely mimicking realistic industrial operation, while possessing high spatiotemporal resolution, high interfacial sensitivity, and the capacity for multi-probe correlative analysis. Moreover, integrated multi-scale modeling (combining DFT, AIMD, ML-MD, kMC, and CFD) will play a crucial role in future water-centered research by bridging microscopic mechanisms with macroscopic performance. To ensure predictive accuracy, these models must be rigorously validated against experimental parameters across various scales. Microscopic validation should focus on adsorbed intermediates and active site states (*e.g.*, vibrational frequencies and adsorption configurations of water-related species, coordination states and electronic structures of active sites under hydration). Mesoscopic validation focuses on coupled reaction-transport phenomena, calibrating parameters such as diffusion parameters, apparent activation energies, and species coverage, together with charge/ion transfer resistance. Macroscopic validation must calibrate interfacial environment and fluid properties (*e.g.*, local pH gradients, water activity, and permeability). Ultimately, the integrated model must be benchmarked against system-level performance indicators (*e.g.*, polarization curves, Tafel slopes, and faradaic efficiencies), while accounting for environmental variables (*e.g.*, electrolyte hydration effects and hydrophobicity of porous structures). This will help us construct a complete physical picture and foster a fundamental understanding of the multi-scale mechanisms of water in the CO_2RR/CORR.

6.3 Developing configuration-specific water management strategies for precise adaptation

Different electrolyser configurations (*e.g.*, flow cells and MEAs) have markedly different requirements for water regulation strategies. An effective strategy in a flow cell may perform poorly or even be counterproductive when transferred to an MEA system, as has already been verified in CORR studies. However, systematic investigation in the context of CO_2RR remains limited, hampering the establishment of translatable guidelines for cross-configuration water management. This necessitates the bespoke design of water introduction/removal, interfacial wettability, and multiphase flow field management according to the specific system characteristics, in order to achieve the precise multi-scale regulation and optimisation of water. Future research should urgently uncover the key behaviours and regulatory bottlenecks of water in different electrolyser designs and, based on this, develop bespoke water management solutions for specific electrolyser and reaction processes.

6.4 Overcoming the bottleneck of long-term operational stability to build effective water management systems

The excellent performance reported for most water management strategies has only been validated over tens or hundreds

of hours. However, their stability and robustness face a severe test during the thousands of hours of long-term operation required for practical implementation at industrially relevant current densities (>200 mA cm^{-2}). Issues such as the degradation and detachment of interfacial modification layers, irreversible flooding or salt precipitation in the GDE, and catalyst reconstruction can all lead to the gradual failure of even the most carefully designed water management systems. Future efforts should focus on designing a new generation of highly efficient and inherently stable electrocatalysts, as well as developing customised and integrated multi-scale coupled water management strategies. It is particularly important to understand how product accumulation (especially of oxygenated products) in turn alters interfacial wettability, pore structure, and proton transport pathways. Based on this understanding, tailor-made multi-scale coupled solutions must be developed to ensure robust long-term operation under demanding industrial conditions.

6.5 Establishing standardised evaluation protocols to accelerate technological iteration and industrialisation

The conditions under which the electrocatalytic CO_2RR/CORR are studied (*e.g.*, electrolyser configuration, gas and electrolyte flow rates) vary immensely. This means that water management strategies that are effective under specific laboratory conditions may prove much less effective in different systems. The lack of standardised evaluation frameworks makes cross-study comparison of water management strategies highly challenging and hinders the development of universal design principles. To accelerate progress from laboratory to industrial applications, the establishment of standardised testing protocols and benchmarks is imperative.

Author contributions

X. He conceptualized the review and wrote the original draft; W. Zhou prepared the majority of the figures and contributed to the writing of the manuscript; J. Chen assisted with the preparation of the figures and summarized the table; Q. Zhang and Y. Wang provided valuable advice and suggestions during the manuscript's development; S. Xie supervised the project and critically revised the manuscript for scientific accuracy and clarity.

Conflicts of interest

There are no conflicts to declare.

Data availability

No primary research results, software or code have been included and no new data were generated or analysed as part of this review.

Acknowledgements

This work was supported by the National Key Research and Development Program of the Ministry of Science and Technology (No. 2022YFA1504600), the National Natural Science Foundation of China (No. 22121001, 22022201, U24A20490, U22A20392, and U23A2087), the Fundamental Research Funds for the Central Universities (No. 20720250005 and 20720240123), the Science and Technology Project of Fujian Province (2022L3077) and the Natural Science Foundation of Fujian Province (No. 2024J011005). We would like to express our gratitude to G. Tang for his valuable suggestions and assistance in figure modifications, as well as to Z. Chen for her help in reviewing the manuscript content.

Notes and references

1 M. Peplow, *Nature*, 2022, **603**, 780–783.
2 W. F. Lamb, T. Gasser, R. M. Roman-Cuesta, G. Grassi, M. J. Gidden, C. M. Powis, O. Geden, G. Nemet, Y. Pratama, K. Riahi, S. M. Smith, J. Steinhauser, N. E. Vaughan, H. B. Smith and J. C. Minx, *Nat. Clim. Change*, 2024, **14**, 644–651.
3 P. De Luna, C. Hahn, D. Higgins, S. A. Jaffer, T. F. Jaramillo and E. H. Sargent, *Science*, 2019, **364**, 350.
4 W. Ma, J. Morales-Vidal, J. Tian, M.-T. Liu, S. Jin, W. Ren, J. Taubmann, C. Chatzichristodoulou, J. Luterbacher, H. M. Chen, N. López and X. Hu, *Nature*, 2025, **641**, 1156–1161.
5 Y. Luo, S. Hu and B. Liu, *Sci. China Mater.*, 2024, **67**, 1780–1790.
6 C. P. O'Brien, R. K. Miao, A. S. Zeraati, G. Lee, E. H. Sargent and D. Sinton, *Chem. Rev.*, 2024, **124**, 3648–3693.
7 X. Ding, J. Zhang and Y. Li, *eScience*, 2023, **3**, 100137.
8 H. Li, H. Li, P. Wei, Y. Wang, Y. Zang, D. Gao, G. Wang and X. Bao, *Energy Environ. Sci.*, 2023, **16**, 1502–1510.
9 P. Wei, D. Gao, T. Liu, H. Li, J. Sang, C. Wang, R. Cai, G. Wang and X. Bao, *Nat. Nanotechnol.*, 2023, **18**, 299–306.
10 B. Pan, Y. Wang and Y. Li, *Chem. Catal.*, 2022, **2**, 1267–1276.
11 J. Wu, W. Li, K. Liu, A. Kucernak, H. Liu, L. Chai and M. Liu, *Next Energy*, 2023, **1**, 100032.
12 T. Burdyny and W. A. Smith, *Energy Environ. Sci.*, 2019, **12**, 1442–1453.
13 A. Gawel, T. Jaster, D. Siegmund, J. Holzmann, H. Lohmann, E. Klemm and U.-P. Apfel, *iScience*, 2022, **25**, 104011.
14 W. Ma, X. He, W. Wang, S. Xie, Q. Zhang and Y. Wang, *Chem. Soc. Rev.*, 2021, **50**, 12897–12914.
15 M. Sassenburg, M. Kelly, S. Subramanian, W. A. Smith and T. Burdyny, *ACS Energy Lett.*, 2023, **8**, 321–331.
16 M. Ma, Y. Fang, Z. Huang, S. Wu, W. He, S. Ge, Z. Zheng, Y. Zhou, W. Fa and X. Wang, *Angew. Chem., Int. Ed.*, 2025, **64**, e202425195.
17 Y. Huang, Y. Gao and B. Zhang, *Chem*, 2025, **11**, 102533.

18 Y. Yuan, J. Li, Y. Zhu, Y. Qiao, Z. Kang, Z. Wang, X. Tian, H. Huang and W. Lai, *Angew. Chem., Int. Ed.*, 2025, **64**, e202425590.
19 M. H. Hicks, W. Nie, A. E. Boehme, H. A. Atwater, T. Agapie and J. C. Peters, *J. Am. Chem. Soc.*, 2024, **146**, 25282–25289.
20 M. Dunwell, Q. Lu, J. M. Heyes, J. Rosen, J. G. Chen, Y. Yan, F. Jiao and B. Xu, *J. Am. Chem. Soc.*, 2017, **139**, 3774–3783.
21 J. Wang, C. Cui, X. Zhu, H. Wang and Q. Ge, *Catalysts*, 2023, **13**, 1033.
22 T. Cheng, H. Xiao and W. A. Goddard, 3rd, *Proc. Natl. Acad. Sci. U. S. A.*, 2017, **114**, 1795–1800.
23 Y. Lum, T. Cheng, W. A. Goddard and J. W. Ager, *J. Am. Chem. Soc.*, 2018, **140**, 9337–9340.
24 B. Hasa, M. Jouny, B. H. Ko, B. Xu and F. Jiao, *Angew. Chem., Int. Ed.*, 2021, **60**, 3277–3282.
25 M. Jouny, W. Luc and F. Jiao, *Nat. Catal.*, 2018, **1**, 748–755.
26 G. Shi, T. Lu and L. Zhang, *Nat. Sci. Rev.*, 2024, **11**, nwae241.
27 M. A. Brown, Z. Abbas, A. Kleibert, R. G. Green, A. Goel, S. May and T. M. Squires, *Phys. Rev. X*, 2016, **6**, 011107.
28 C. G. Malmberg and A. A. Maryott, *J. Res. Natl. Bur. Stand.*, 1956, **56**, 1–8.
29 C. M. Schott, P. M. Schneider, K. T. Song, H. Yu, R. Götz, F. Haimerl, E. Gubanova, J. Zhou, T. O. Schmidt, Q. Zhang, V. Alexandrov and A. S. Bandarenka, *Chem. Rev.*, 2024, **124**, 12391–12462.
30 J. Le, A. Chen, Y. Kuang and J. Cheng, *Nat. Sci. Rev.*, 2023, **10**, nwad105.
31 J. Gu, S. Liu, W. Ni, W. Ren, S. Haussener and X. Hu, *Nat. Catal.*, 2022, **5**, 268–276.
32 Q. Wu and Z. J. Xu, *Angew. Chem., Int. Ed.*, 2025, **64**, e202505022.
33 X. Yang, H. Ding, S. Li, S. Zheng, J. Li and F. Pan, *J. Am. Chem. Soc.*, 2024, **146**, 5532–5542.
34 H. Zhang, J. Gao, D. Raciti and A. S. Hall, *Nat. Catal.*, 2023, **6**, 807–817.
35 Z. Tang, Z. Dong, L. Yuan, B. Li and Y. Zhu, *EES Catal.*, 2025, **3**, 943–971.
36 Z. Zhang, T. Wang, Y. Cai, X. Li, J. Ye, Y. Zhou, N. Tian, Z. Zhou and S. Sun, *Nat. Catal.*, 2024, **7**, 807–817.
37 C. Y. Li, J. B. Le, Y. H. Wang, S. Chen, Z. L. Yang, J. F. Li, J. Cheng and Z. Q. Tian, *Nat. Mater.*, 2019, **18**, 697–701.
38 D. Cheng, Z. Wei and P. Sautet, *J. Am. Chem. Soc.*, 2025, **147**, 10954–10965.
39 A. Hassanali, F. Giberti, J. Cuny, T. D. Kühne and M. Parrinello, *Proc. Natl. Acad. Sci. U. S. A.*, 2013, **110**, 13723–13728.
40 J. Li, X. Li, C. M. Gunathunge and M. M. Waegele, *Proc. Natl. Acad. Sci. U. S. A.*, 2019, **116**, 9220–9229.
41 H. Xiao, W. A. G. Iii, T. Cheng and Y. Liu, *Proc. Natl. Acad. Sci. U. S. A.*, 2017, **114**, 6685–6688.
42 J. Jiao, R. Lin, S. Liu, W. Cheong, C. Zhang, Z. Chen, Y. Pan, J. Tang, K. Wu, S.-F. Hung, H. M. Chen, L. Zheng, Q. Lu, X. Yang, B. Xu, H. Xiao, J. Li, D. Wang, Q. Peng, C. Chen and Y. Li, *Nat. Chem.*, 2019, **11**, 222–228.
43 Z. Huang, M. Fang, X. Feng, M. Wang, W. Jiang, Z. Wang, R. Zhang, Y. Zhu and L. Jiang, *Adv. Funct. Mater.*, 2025, e09330.
44 J. Y. T. Kim, C. Sellers, S. Hao, T. P. Senftle and H. Wang, *Nat. Catal.*, 2023, **6**, 1115–1124.
45 M. R. Singh, Y. Kwon, Y. Lum, J. W. Ager and A. T. Bell, *J. Am. Chem. Soc.*, 2016, **138**, 13006–13012.
46 O. Ayemoba and A. Cuesta, *ACS Appl. Mater. Interfaces*, 2017, **9**, 27377–27382.
47 M. Ma and B. Seger, *Angew. Chem., Int. Ed.*, 2024, **63**, e202401185.
48 F. Pan, X. Duan, L. Fang, H. Li, Z. Xu, Y. Wang, T. Wang, T. Li, Z. Duan and K. Chen, *Adv. Energy Mater.*, 2024, **14**, 2303118.
49 Q. Sun, *Molecules*, 2022, **27**, 7009.
50 F. Sun, X. Zhou, L. Qin, Z. Tang, L. Wang and Q. Tang, *ACS Catal.*, 2025, **15**, 4605–4617.
51 P. Lai, Y. Zhang, B. Huang, X. Deng, H. Hua, Q. Chen, S. Zhao, J. Dai, P. Zhang and J. Zhao, *Energy Storage Mater.*, 2024, **67**, 103314.
52 X. Jing, L. Chen, Y. Liu and Z. Fu, *Chem. Technol. Fuels Oils*, 2022, **58**, 410–421.
53 X. You, D. Zhang, X. G. Zhang, X. Li, J. H. Tian, Y. H. Wang and J. F. Li, *Nano-micro Lett.*, 2023, **16**, 53.
54 B. Tang, Y. Fang, S. Zhu, Q. Bai, X. Li, L. Wei, Z. Li and C. Zhu, *Chem. Sci.*, 2024, **15**, 7111–7120.
55 W. Ren, Y. Zheng and S. Qiao, *Energy Environ. Sci.*, 2025, **3**, 7402–7412.
56 P. A. Kempler, R. H. Coridan and L. Luo, *Chem. Rev.*, 2024, **124**, 10964–11007.
57 M. S. Kodaimati, R. Gao, S. E. Root and G. M. Whitesides, *Chem. Catal.*, 2022, **2**, 797–815.
58 M. E. Leonard, M. J. Orella, N. Aiello, Y. Román-Leshkov, A. Forner-Cuenca and F. R. Brushett, *J. Electrochem. Soc.*, 2020, **167**, 124521.
59 R. Akbari, M. Mastrosimone, M. Muhyuddin, T. Caielli, P. Mustarelli, C. Santoro and C. Antonini, *Mater. Renew. Sustain. Energy*, 2025, **14**, 47.
60 A. Kusoglu and A. Z. Weber, *Chem. Rev.*, 2017, **117**, 987–1104.
61 K. V. Petrov, C. I. Koopman, S. Subramanian, M. T. M. Koper, T. Burdyny and D. A. Vermaas, *Nat. Energy*, 2024, **9**, 932–938.
62 W. L. Toh, H. Q. Dinh, A. T. Chu, E. R. Sauvé and Y. Surendranath, *Nat. Energy*, 2023, **8**, 1405–1416.
63 V. M. Ehlinger, D. U. Lee, T. Y. Lin, E. B. Duoss, S. E. Baker, T. F. Jaramillo and C. Hahn, *ChemElectroChem*, 2024, **11**, e202300566.
64 G. Li, Y. Liu, T. Feng and R. Ye, *ChemElectroChem*, 2024, **11**, e202400475.
65 J. C. Bui, E. W. Lees, A. K. Liu, W. L. Toh, T. N. Stovall, P. Goyal, F. J. U. Galang, Y. Surendranath, A. T. Bell and A. Z. Weber, *Nat. Chem. Eng.*, 2024, **2**, 63–76.
66 J. C. Bui, E. W. Lees, D. H. Marin, T. N. Stovall, L. Chen, A. Kusoglu, A. C. Nielander, T. F. Jaramillo, S. W. Boettcher, A. T. Bell and A. Z. Weber, *Nat. Chem. Eng.*, 2024, **1**, 45–60.

67 K. Xie, R. K. Miao, A. Ozden, S. Liu, Z. Chen, C. T. Dinh, J. E. Huang, Q. Xu, C. M. Gabardo, G. Lee, J. P. Edwards, C. P. O'Brien, S. W. Boettcher, D. Sinton and E. H. Sargent, *Nat. Commun.*, 2022, **13**, 3609.
68 M. Li, E. W. Lees, W. Ju, S. Subramanian, K. Yang, J. C. Bui, H. P. Iglesias van Montfort, M. Abdinejad, J. Middelkoop, P. Strasser, A. Z. Weber, A. T. Bell and T. Burdyny, *Nat. Commun.*, 2024, **15**, 8222.
69 M. Jouny, G. S. Hutchings and F. Jiao, *Nat. Catal.*, 2019, **2**, 1062–1070.
70 R. Rodriguez-Mosqueda, E. A. Bramer, T. Roestenberg and G. Brem, *Int. J. Hydrogen Energy*, 2018, **57**, 3628–3638.
71 Y. Xu, J. P. Edwards, S. Liu, R. K. Miao, J. E. Huang, C. M. Gabardo, C. P. O'Brien, J. Li, E. H. Sargent and D. Sinton, *ACS Energy Lett.*, 2021, **6**, 809–815.
72 D. Wakerley, S. Lamaison, F. Ozanam, N. Menguy, D. Mercier, P. Marcus, M. Fontecave and V. Mougel, *Nat. Mater.*, 2019, **18**, 1222–1227.
73 Z. Liu, X. Lv, S. Kong, M. Liu, K. Liu, J. Zhang, B. Wu, Q. Zhang, Y. Tang, L. Qian, L. Zhang and G. Zheng, *Angew. Chem., Int. Ed.*, 2023, **62**, e202309319.
74 J. Chen, H. Qiu, Y. Zhao, H. Yang, L. Fan, Z. Liu, S. Xi, G. Zheng, J. Chen, L. Chen, Y. Liu, L. Guo and L. Wang, *Nat. Commun.*, 2024, **15**, 5893.
75 Y. Wei, J. Zhang, B. Li, F. Yu, M. Li, Y. Wang, T. He, J. Zhu, S. Chen, Y. Su, S. Ding, C. Xiao and B. Y. Xia, *Adv. Mater.*, 2025, **37**, 2504515.
76 Y. Wang, Y. Cheng, S. Liu, Y. Yin, J. Yang, H. Wang, K. Li, M. Zhou, J. Jiao, P. Zhang, Q. Qian, Q. Zhu, X. Sun, Y. Xu, M. Luo, X. Kang and B. Han, *Angew. Chem., Int. Ed.*, 2025, **64**, e202420661.
77 S. Lee, Y. Jeon, S. Lee, W. Lee, S. Kim, J. Choi, J. Park, J. Han, Y. N. Ko, Y. Kim, J. Park, J. Kim, K. T. Park and J. Lee, *Chem. Eng. J.*, 2023, **464**, 142593.
78 W. Ren, H. Zhang, M. Chang, N. Chen, W. Ma, J. Gu, M. Lin and X. Hu, *Chem*, 2025, **11**, 102352.
79 W. Tang, Y. Shen, Y. Yang, C. Li, Y. Li, S. Yin, F. Li, H. Li and C. Li, *Nano Res.*, 2025, **18**, 94907200.
80 N. Lee, H. Y. Jang, K. Shim, S. M. Jung, J. Lee, S. H. You, H. S. Kang, J. K. Kim, S. Back and Y. T. Kim, *ACS Appl. Energy Mater.*, 2023, **6**, 4413–4421.
81 X. Wang, X. Sang, C. Dong, S. Yao, L. Shuai, J. Lu, B. Yang, Z. Li, L. Lei, M. Qiu, L. Dai and Y. Hou, *Angew. Chem., Int. Ed.*, 2021, **60**, 11959–11965.
82 S. Chen, Z. Zhang, W. Jiang, S. Zhang, J. Zhu, L. Wang, H. Ou, S. Zaman, L. Tan, P. Zhu, E. Zhang, P. Jiang, Y. Su, D. Wang and Y. Li, *J. Am. Chem. Soc.*, 2022, **144**, 12807–12815.
83 Y. Liang, F. Li, R. K. Miao, S. Hu, W. Ni, S. Zhang, Y. Liu, Y. Bai, H. Wan, P. Ou, X.-Y. Li, N. Wang, S. Park, F. Li, J. Zeng, D. Sinton and E. H. Sargent, *Nat. Synth.*, 2024, **3**, 1104–1112.
84 X. Yan, C. Chen, Y. Wu, S. Liu, Y. Chen, R. Feng, J. Zhang and B. Han, *Chem. Sci.*, 2021, **12**, 6638–6645.
85 X. Qi, J.-H. Wang, J. Shao, H. Dong, C. Li and Y.-W. Zhang, *Appl. Catal., B*, 2026, **382**, 125920.
86 Y. Hu, M. Zhou, K. Xu, Z. Yang and Z. Dong, *J. Energy Chem.*, 2026, **115**, 337–346.
87 X. He, L. Lin, X. Li, M. Zhu, Q. Zhang, S. Xie, B. Mei, F. Sun, Z. Jiang, J. Cheng and Y. Wang, *Nat. Commun.*, 2024, **15**, 9923.
88 W. Ma, S. Xie, T. Liu, Q. Fan, J. Ye, F. Sun, Z. Jiang, Q. Zhang, J. Cheng and Y. Wang, *Nat. Catal.*, 2020, **3**, 478–487.
89 Y. Yang, Z. Tan, J. Zhang, J. Yang, R. Zhang, S. Wang, Y. Song and Z. Su, *Green Energy Environ.*, 2024, **9**, 1459–1465.
90 X. Chen, J. Chen, H. Chen, Q. Zhang, J. Li, J. Cui, Y. Sun, D. Wang, J. Ye and L. Liu, *Nat. Commun.*, 2023, **14**, 751.
91 Y. Li, X. Zhang, X. Tai, X. Yang, P. Yu, S. Dong, L. Chi, Z. Wu, Y. Zhang, S. Sun, P. Lu, L. Zhu, F. Gao, Y. Lin and M. Gao, *Angew. Chem., Int. Ed.*, 2025, **64**, e202422054.
92 Y. Cao, Z. Chen, P. Li, A. Ozden, P. Ou, W. Ni, J. Abed, E. Shirzadi, J. Zhang, D. Sinton, J. Ge and E. H. Sargent, *Nat. Commun.*, 2023, **14**, 2387.
93 F. P. García De Arquer, C.-T. Dinh, A. Ozden, J. Wicks, C. McCallum, A. R. Kirmani, D.-H. Nam, C. Gabardo, A. Seifitokaldani, X. Wang, Y. C. Li, F. Li, J. Edwards, L. J. Richter, S. J. Thorpe, D. Sinton and E. H. Sargent, *Science*, 2020, **367**, 661–666.
94 Q. Fan, T. Xiao, H. Liu, T. Yan, J. Lin, S. Kuang, H. Chi, T. J. Meyer, S. Zhang and X. Ma, *ACS Cent. Sci.*, 2024, **10**, 2331–2337.
95 X. Chen, J. Chen, N. M. Alghoraibi, D. A. Henckel, R. Zhang, U. O. Nwabara, K. E. Madsen, P. J. A. Kenis, S. C. Zimmerman and A. A. Gewirth, *Nat. Catal.*, 2020, **4**, 20–27.
96 Z. Du, S. Li, G. Liang, Y. Xie, Y. A, Y. Zhang, H. Zhang, J. Tian, S. Zheng, Q. Zheng, Z. Chen, W. F. Ip, J. Liu and J. Li, *J. Am. Chem. Soc.*, 2024, **146**, 32870–32879.
97 M. Chang, S. Yoo, W. Ma, H. Girault, Y. J. Hwang and X. Hu, *J. Am. Chem. Soc.*, 2025, **147**, 34001–34010.
98 X. Han, Q. Wang, Y. Wu and C. Wu, *Electrochim. Acta*, 2022, **402**, 139526.
99 H. Zhang, D. Raciti and A. S. Hall, *Nat. Chem.*, 2025, **17**, 1161–1168.
100 S. Banerjee, C. S. Gerke and V. S. Thoi, *Acc. Chem. Res.*, 2022, **55**, 504–515.
101 W. Ni, Y. Guan, H. Chen, Y. Zhang, S. Wang and S. Zhang, *Angew. Chem., Int. Ed.*, 2023, **62**, e202303233.
102 Y. Wu, S. Garg, M. Li, M. N. Idros, Z. Li, R. Lin, J. Chen, G. Wang and T. E. Rufford, *J. Power Sources*, 2022, **522**, 230998.
103 Q. Wan, L. Yuan, W. Jiang, Y. Liu, L. Zhang, X. Zhuang, J. Zhang and C. Ke, *ACS Sustainable Chem. Eng.*, 2023, **11**, 17046–17052.
104 L. Li, J. Chen, V. S. S. Mosali, Y. Liang, A. M. Bond, Q. Gu and J. Zhang, *Angew. Chem., Int. Ed.*, 2022, **61**, e202208534.
105 Z. Xing, L. Hu, D. S. Ripatti, X. Hu and X. Feng, *Nat. Commun.*, 2021, **12**, 136.
106 X. Kong, C. Wang, Z. Xu, Y. Zhong, Y. Liu, L. Qin, J. Zeng and Z. Geng, *Nano Lett.*, 2022, **22**, 8000–8007.

107 Y. Zhao, L. Hao, A. Ozden, S. Liu, R. Miao, P. Ou, T. Alkayyali, S. Zhang, J. Ning, Y. Liang, Y. Xu, M. Fan, Y. Chen, J. E. Huang, K. Xie, J. Zhang, C. P. O'Brien, F. Li, E. H. Sargent and D. Sinton, *Nat. Synth.*, 2023, **2**, 403–412.
108 C. Dinh, T. Burdyny, M. G. Kibria, A. Seifitokaldani, C. M. Gabardo, F. P. García De Arquer, A. Kiani, J. P. Edwards, P. De Luna, O. S. Bushuyev, C. Zou, R. Quintero-Bermudez, Y. Pang, D. Sinton and E. H. Sargent, *Science*, 2018, **360**, 783–787.
109 M. Sun, J. Cheng and M. Yamauchi, *Nat. Commun.*, 2024, **15**, 491.
110 R. Chen, H. Y. Su, D. Liu, R. Huang, X. Meng, X. Cui, Z. Q. Tian, D. H. Zhang and D. Deng, *Angew. Chem., Int. Ed.*, 2020, **59**, 154–160.
111 W. Ren, W. Ma and X. Hu, *Joule*, 2023, **7**, 2349–2360.
112 T. Möller, T. Ngo Thanh, X. Wang, W. Ju, Z. Jovanov and P. Strasser, *Energy Environ. Sci.*, 2021, **14**, 5995–6006.
113 A. B. Moss, S. Garg, M. Mirolo, C. A. G. Rodriguez, R. Ilvonen, I. Chorkendorff, J. Drnec and B. Seger, *Joule*, 2023, **7**, 350–365.
114 D. Kim, M. H. Han, J. Park, H. Kim, H. Bang, S. Yu, J. Choi, H. Oh and W. H. Lee, *J. Power Sources*, 2024, **621**, 235324.
115 T. Ma, H. Qiu, W. Jing, F. Wang, Y. Liu and L. Guo, *J. Mater. Chem. A*, 2024, **12**, 15343–15351.
116 M. Quentmeier, B. Schmid, H. Tempel and R.-A. Eichel, *ACS Sustainable Chem. Eng.*, 2024, **12**, 3876–3885.
117 J. Li, H. Zhang, C. Luo, D. Cheng, W. Xu and M. Lin, *Nat. Commun.*, 2025, **16**, 4181.
118 S. Yuan, R. Wang, R. Xue, L. Wu, G. Zhang, H. Li, Q. Wang, J. Yin, L. Luo, S. Shen, L. An, X. Yan and J. Zhang, *ACS Energy Lett.*, 2024, **9**, 5945–5954.
119 S. Hao, A. Elgazzar, N. Ravi, T.-U. Wi, P. Zhu, Y. Feng, Y. Xia, F. Chen, X. Shan and H. Wang, *Nat. Energy*, 2025, **10**, 266–277.
120 B. S. Crandall, B. H. Ko, S. Overa, L. Cherniack, A. Lee, I. Minnie and F. Jiao, *Nat. Chem. Eng.*, 2024, **1**, 421–429.
121 D. Q. Song, Y. B. Lian, M. Wang, Y. H. Su, F. L. Lyu, Z. Deng and Y. Peng, *eScience*, 2023, **3**, 100097.
122 C. Kim, J. C. Bui, X. Luo, J. K. Cooper, A. Kusoglu, A. Z. Weber and A. T. Bell, *Nat. Energy*, 2021, **6**, 1026–1034.
123 Y. Guo, P. Lei, X. Wei, X. Z. Fu, S. Q. Liu and J. L. Luo, *Chem. Commun.*, 2025, **61**, 15670–15673.
124 Z. Wang, D. Liu, C. Xia, X. Shi, Y. Zhou, Q. Liu, J. Huang, H. Wu, D. Zhu, S. Zhang, J. Li, P. Deng, A. S. Vasenko, B. Y. Xia and X. Tian, *Nat. Commun.*, 2025, **16**, 1754.
125 W. Ma, S. Xie, X. G. Zhang, F. Sun, J. Kang, Z. Jiang, Q. Zhang, D. Y. Wu and Y. Wang, *Nat. Commun.*, 2019, **10**, 892.
126 S. Li, G. Zhang, X. Ma, H. Gao, D. Fu, T. Wang, J. Zeng, Z. Zhao, P. Zhang and J. Gong, *J. Am. Chem. Soc.*, 2024, **146**, 31927–31934.
127 Y. Chen, N. Lyu, J. Zhang, S. Yan, C. Peng, C. Yang, X. Lv, C. Hu, M. Kuang and G. Zheng, *Small*, 2024, **20**, 2308004.
128 J. Li, A. Xu, F. Li, Z. Wang, C. Zou, C. M. Gabardo, Y. Wang, A. Ozden, Y. Xu, D. Nam, Y. Lum, J. Wicks, B. Chen, Z. Wang, J. Chen, Y. Wen, T. Zhuang, M. Luo, X. Du, T. Sham, B. Zhang, E. H. Sargent and D. Sinton, *Nat. Commun.*, 2020, **11**, 3685.
129 X. Wang, W. Sun, P. Wang, T. Sheng, F. Gao and Z. Wu, *Sci. China Mater.*, 2025, **68**, 455–463.
130 M. Luo, Z. Wang, Y. C. Li, J. Li, F. Li, Y. Lum, D. H. Nam, B. Chen, J. Wicks, A. Xu, T. Zhuang, W. R. Leow, X. Wang, C. T. Dinh, Y. Wang, Y. Wang, D. Sinton and E. H. Sargent, *Nat. Commun.*, 2019, **10**, 5814.
131 H. Zhang, Y. Sun, J. Wang, X. Gao, Z. Tang, S. Li, Z. Hou, X. Wang, K. Nie, J. Xie, Z. Yang and Y.-M. Yan, *ACS Appl. Energy Mater.*, 2023, **6**, 11448–11457.
132 Y. Zhang, F. Chen, G. Gao, M. Xu, Y. Song, C. Sun, X. Zhang, X. Zhang, H. Dong, W. Wang, F. Lu, Z. Lu, R. Zhang, H. Liu, H. Liu, R. Zheng and Y. Cheng, *Nano Energy*, 2025, **135**, 110657.
133 J. Xia, S. Li, X. Liu, X. Dong, J. Mao, A. Chen, H. Zhu, X. Wang, Z. Xu, Y. Wei, G. Li, Y. Song, W. Wei and W. Chen, *Appl. Catal., B*, 2025, **371**, 125202.
134 M. Feng, Z. Chen, H. Sun, S. Yao, Z. Liu, M. Lu, F. Li, H. Wang and L. Liu, *J. Energy Chem.*, 2025, **107**, 582–590.
135 S. You, J. Xiao, S. Liang, W. Xie, T. Zhang, M. Li, Z. Zhong, Q. Wang and H. He, *Energy Environ. Sci.*, 2024, **17**, 5795–5818.
136 M. Ma, K. Djanashvili and W. A. Smith, *Angew. Chem., Int. Ed.*, 2016, **55**, 6680–6684.
137 W. Fu, Y. Li, J. Chen, J. Chen, S. Xi, J. Zhang and L. Wang, *Angew. Chem., Int. Ed.*, 2024, **63**, e202407992.
138 J. Li, Q. Zhu, A. Chang, S. Cheon, Y. Gao, B. Shang, H. Li, C. L. Rooney, L. Ren, Z. Jiang, Y. Liang, Z. Feng, S. Yang, L. Robert Baker and H. Wang, *Nat. Nanotechnol.*, 2025, **20**, 515–522.
139 P. C. Chen, C. Chen, Y. Yang, A. L. Maulana, J. Jin, J. Feijoo and P. Yang, *J. Am. Chem. Soc.*, 2023, **145**, 10116–10125.
140 L. Bian, Y. Bai, J. Y. Chen, H. K. Guo, S. Liu, H. Tian, N. Tian and Z. L. Wang, *ACS Nano*, 2025, **19**, 9304–9316.
141 K. Liao, M. Askerka, E. L. Zeitler, A. B. Bocarsly and V. S. Batista, *Top. Catal.*, 2015, **58**, 23–29.
142 H. Rabiee, B. Ma, Y. Yang, F. Li, P. Yan, Y. Wu, X. Zhang, S. Hu, H. Wang, L. Ge and Z. Zhu, *Adv. Funct. Mater.*, 2025, **35**, 2411195.
143 A. A. Samu, I. Szenti, Á. Kukovecz, B. Endrődi and C. Janáky, *Commun. Chem.*, 2023, **6**, 41.
144 Y. Kong, M. Liu, H. Hu, Y. Hou, S. Vesztergom, M. D. J. Gálvez-Vázquez, I. Zelocualtecatl Montiel, V. Kolivoška and P. Broekmann, *Small Methods*, 2022, **6**, 2200369.
145 A. Reyes, R. P. Jansonius, B. A. W. Mowbray, Y. Cao, D. G. Wheeler, J. Chau, D. J. Dvorak and C. P. Berlinguette, *ACS Energy Lett.*, 2020, **5**, 1612–1618.
146 P. Saha, D. Henckel, C. Baez-Cotto, F. Intia, L. Hu, T. Van Cleve and K. C. Neyerlin, *J. Electrochem. Soc.*, 2023, **170**, 014505.
147 Y. Wang, Y. Yang, S. Jia, X. Wang, K. Lyu, Y. Peng, H. Zheng, X. Wei, H. Ren, L. Xiao, J. Wang, D. A. Muller, H. D. Abruña, B. J. Hwang, J. Lu and L. Zhuang, *Nat. Commun.*, 2019, **10**, 1506.

148 L. Weng, A. T. Bell and A. Z. Weber, *Energy Environ. Sci.*, 2019, **12**, 1950–1968.
149 C. A. Giron Rodriguez, N. C. Kani, A. B. Moss, B. O. Joensen, S. Garg, W. Deng, T. Wilson, J. R. Varcoe, I. Chorkendorff and B. Seger, *EES Catal.*, 2024, **2**, 850–861.
150 V. D. Brandão, H. Song, A. Venkataraman, Y. Fishler, S. S. Arora, S. S. Bhargava, C. Villa, A. Holewinski, S. Nair, M. C. Hatzell and C. Sievers, *ACS Catal.*, 2025, **15**, 8979–8990.
151 D. G. Wheeler, B. A. W. Mowbray, A. Reyes, F. Habibzadeh, J. He and C. P. Berlinguette, *Energy Environ. Sci.*, 2020, **13**, 5126–5134.
152 M. Sauermoser, N. Kizilova, B. G. Pollet and S. Kjelstrup, *Front. Energy Res.*, 2020, **8**, 00013.
153 R. F. Ziesche, J. Hack, L. Rasha, M. Maier, C. Tan, T. M. M. Heenan, H. Markötter, N. Kardjilov, I. Manke, W. Kockelmann, D. J. L. Brett and P. R. Shearing, *Nat. Commun.*, 2022, **13**, 1616.
154 I. Sullivan, L. Han, S. H. Lee, M. Lin, D. M. Larson, W. S. Drisdell and C. Xiang, *ACS Sustainable Chem. Eng.*, 2019, **7**, 16964–16970.
155 H. M. Pelzer, N. Kolobov, D. A. Vermaas and T. Burdyny, *Nat. Energy*, 2025, **10**, 549–556.
156 J. W. Hurkmans, H. M. Pelzer, T. Burdyny, J. Peeters and D. A. Vermaas, *EES Catal.*, 2025, **3**, 305–317.
157 C. Zhan, X. Chen, J. Yi, J. F. Li, D. Y. Wu and Z. Q. Tian, *Nat. Rev. Chem.*, 2018, **2**, 216–230.
158 L. Sun, V. Reddu, S. Xi, C. Dai, Y. Sheng, T. Su, A. C. Fisher and X. Wang, *Adv. Energy Mater.*, 2022, **12**, 2202108.
159 X. Ren, J. Zhao, X. Li, J. Shao, B. Pan, A. Salame, E. Boutin, T. Groizard, S. Wang, J. Ding, X. Zhang, W. Y. Huang, W. J. Zeng, C. Liu, Y. Li, S. F. Hung, Y. Huang, M. Robert and B. Liu, *Nat. Commun.*, 2023, **14**, 3401.
160 Y. Zhao, Q. Q. Li, Q. F. He, P. W. Ren, D. A. Zhang, Y. H. Wang, J. C. Dong, S. Zheng, Y. J. Zhang, Z. L. Yang and J. F. Li, *J. Am. Chem. Soc.*, 2025, **147**, 30230–30238.
161 S. Kumar, J. J. C. Counter, D. C. Grinter, M. A. V. Spronsen, P. Ferrer, A. Large, M. W. Orzech, P. Jerzy Wojcik and G. Held, *J. Phys. Energy*, 2024, **6**, 036001.
162 B. Ó. Joensen, J. A. Zamora Zeledón, L. Trotochaud, A. Sartori, M. Mirolo, A. B. Moss, S. Garg, I. Chorkendorff, J. Drnec, B. Seger and Q. Xu, *Joule*, 2024, **8**, 1754–1771.
163 J. Disch, L. Bohn, S. Koch, M. Schulz, Y. Han, A. Tengattini, L. Helfen, M. Breitwieser and S. Vierrath, *Nat. Commun.*, 2022, **13**, 6099.
164 X. Lu, C. Zhou, R. S. Delima, E. W. Lees, A. Soni, D. J. Dvorak, S. Ren, T. Ji, A. Bahi, F. Ko and C. P. Berlinguette, *Nat. Chem.*, 2024, **16**, 979–987.
165 Y.-J. Ko, C. Lim, J. Jin, M. G. Kim, J. Y. Lee, T. Seong, K. Lee, B. K. Min, J. Choi, T. Noh, G. W. Hwang, W. H. Lee and H. Oh, *Nat. Commun.*, 2024, **15**, 3356.
166 L. M. Baumgartner, A. Kahn, M. Hoogland, J. Bleeker, W. F. Jager and D. A. Vermaas, *ACS Sustainable Chem. Eng.*, 2023, **11**, 10430–10440.
167 H. Warkentin, C. P. O'Brien, S. Holowka, B. Maxwell, M. Awara, M. Bouman, A. S. Zeraati, R. Nicholas, A. H. Ip, E. S. Elsahwi, C. M. Gabardo and D. Sinton, *ChemSusChem*, 2023, **16**, e202300657.
168 Y. Qu, K. Yang, W. Li, G. Wang, L. Xiao, G. Wang and L. Zhuang, *ACS Energy Lett.*, 2024, **9**, 3042–3048.
169 D. M. Rottmann, R. Kollmuss, S. Haufe and K. J. J. Mayrhofer, *J. Electrochem. Soc.*, 2025, **172**, 054510.
170 Y. Meng, Z. Xu, Z. Shen, Q. Xia, Y. Cao, Y. Wang and X. Li, *J. Mater. Chem. A*, 2022, **10**, 6508–6522.
171 J. Chen, B. W. J. Chen, J. Zhang, W. Chen and Y. Y. Sun, *Chem. Sci.*, 2024, **15**, 8835–8840.
172 F.-T. Wang and J. Cheng, *Curr. Opin. Electrochem.*, 2025, **49**, 101605.
173 P. L. Geissler, C. Dellago, D. Chandler, J. Hutter and M. Parrinello, *Science*, 2001, **291**, 2121–2124.
174 X. Tian, A. Tosello Gardini, U. Raucci, H. Xiao, Y. Zhuo and M. Parrinello, *Nat. Commun.*, 2025, **16**, 10636.
175 X. Qin, T. Vegge and H. A. Hansen, *J. Am. Chem. Soc.*, 2023, **145**, 1897–1905.
176 C. Zhang, M. F. Calegari Andrade, Z. K. Goldsmith, A. S. Raman, Y. Li, P. M. Piaggi, X. Wu, R. Car and A. Selloni, *Nat. Commun.*, 2024, **15**, 10270.
177 J. Li, I. Maresi, Y. Lum and J. W. Ager, *J. Chem. Phys.*, 2021, **155**, 164701.
178 S. Wei, Y. Luo, H. Zhang, X. Du, Y. Wang, G. Liu and J. Li, *J. Phys. Chem. Lett.*, 2025, **16**, 2896–2904.
179 T. Wang, S. Wei, Y. Zhao, Z. Xiong, J. Zhang, J. Liu, L. Luo and T. Chen, *Int. J. Hydrogen Energy*, 2025, **105**, 1186–1206.
180 H. G. Qin, Y. F. Du, Y. Y. Bai, F. Z. Li, X. Yue, H. Wang, J. Z. Peng and J. Gu, *Nat. Commun.*, 2023, **14**, 5640.
181 R. Barnett, F. Municchi, J. King and M. Icardi, *Eng. Comput.*, 2023, **39**, 4129–4152.
182 J. C. Bui, E. W. Lees, L. M. Pant, I. V. Zenyuk, A. T. Bell and A. Z. Weber, *Chem. Rev.*, 2022, **122**, 11022–11084.